Hydrogen Hyperfine Studies of the Early Universe

by

Ian Maxwell Avruch

B.A. Physics, Brandeis University (1989)
S.M. Physics, Massachusetts Institute of Technology (1991)

Submitted to the Department of Physics
in partial fulfillment of the requirements for the degree of

Doctor of Philosophy

at the

MASSACHUSETTS INSTITUTE OF TECHNOLOGY

June 1998

Author .....
Department of Physics
May 18, 1998

Certified by .....
Bernard F. Burke
William A.M. Burden Professor of Astrophysics
Thesis Supervisor

Accepted by .....
Thomas J. Greytak
Professor, Associate Department Head for Education

Hydrogen Hyperfine Studies of the Early Universe

by

Ian Maxwell Avruch

Submitted to the Department of Physics
on May 18, 1998, in partial fulfillment of the
requirements for the degree of
Doctor of Philosophy

Abstract

In this thesis I describe several investigations in high redshift radio astronomy.

The Arecibo Search for HI Protoclusters is an ongoing experiment at Arecibo Observatory to detect highly redshifted hyperfine emission from protogalactic condensates of neutral hydrogen. I describe the custom-built instrument we have installed, and the reduction and analysis of the data obtained. I am able to place upper limits on the masses of HI protoclusters undetected in our fields, generally at the level $10^{16}\,M_{\odot}$. I discuss the instrumental and environmental effects which most influence our sensitivity. I also describe extensive numerical modeling of the system optics aimed at maximizing sensitivity.

The MIT Near–Real–Time Correlator is a test fixture in support of the VSOP Orbiting Very Long Baseline Interferometry (OVLBI) experiment. OVLBI allows high resolution imaging of very distant bright sources. I describe the design and operation of this instrument, which we installed at Green Bank Observatory, and with which we performed OVLBI experiments on a baseline consisting of the GB140′ telescope and the VSOP satellite. We have not yet detected fringes, although we have successfully observed Galactic maser emission in W49 with the 140′ by using the NRTC as an autocorrelator.

Low surface brightness radio structure has been discovered in the field of the gravitational lens 0957+561. The emission is diffuse and so faint as to be near the limiting sensitivity of the Very Large Array, the instrument used to perform the observations. Nevertheless, by coadding many data sets and carefully calibrating we map the features and identify several which may be lensed. An arc 5″ to the east of G may be a stretched image of emission in the background quasar's environment. 1.4″ southwest of G we detect a source that we interpret as an image of emission from the quasar's western lobe, which could provide a constraint on the slope of the gravitational potential in the central region of the lens. We explore the consequences of these new constraints with simple lens models of the system.

Thesis Supervisor: Bernard F. Burke
Title: William A.M. Burden Professor of Astrophysics

Acknowledgments

Firstly, all of the work described in this thesis grew from the ideas and suggestions of Professor Bernard Burke. Under Bernie's supervision I have gained experience in areas allied to Radio Astronomy that more linear trajectories would bypass: from building antennae and measuring their patterns on the roof of Building 26 to designing high-speed digital equipment at Harvard, and in the end doing a project in experimental cosmology, which was my goal in coming to graduate school. I am fortunate to have had Bernie provide me with all these broadening opportunities.

The Arecibo project, which constitutes the bulk of this thesis, is a collaboration between M.I.T., Harvard, and N.A.I.C. At Harvard, Professor Paul Horowitz, Jonathan Weintroub, and Darren Leigh, in addition to their own work, taught me the how to do my job. They are all very generous with their time and fellowship, and in particular Paul allows his lab and equipment to serve as a resource to researchers from Harvard, M.I.T., and probably plenty more. In short, Jono taught me how to build things and Darren taught me how to program.

Dr. Michael Davis at N.A.I.C., in charge of the experiment at Arecibo, besides setting up the upstairs front end has babysat the instrument for four years. Even though he is the Project Scientist in charge of the Gregorian Upgrade, he found time to tend to the apparatus and to encourage Jono and I in our work when it might have seemed we had disappeared.

Glen Langston at N.R.A.O. prepared for our arrival with the correlator, and then stayed up all night with us getting it to work. His good spirits and trenchant advice for graduate students are hereby noted.

Peggy Berkovitz in the Physics Graduate Office is the most helpful person at M.I.T. If she isn't acknowledged in every contemporary physics thesis in the library then there has been an oversight. Jack Barrett has been a guide in the hardware matter of this work, and a stalwart presence in the lab. Sam Conner served as an advisor *pro tem* when I first landed in Bernie's group and worked on 0957+561. No one I've met at M.I.T. equals his knowledge of physics, concern for fellow students, and friendly humor (except for Julianna Hsu, but not as boisterous).

Cathy Trotter spent a lot of time as sysadmin when she should have been working on

her thesis, and when the computers were moved from the RLE to the CSR came back to the lab and made sure they came up smoothly so I could get back to work the same day. Debbie Haarsma took over the AIPS administration when I defaulted on it after a short term. Chris Moore was always interested in discussing the work with me, and always had good suggestions, which he explained with excellent pedagogy. It was a pleasure to work with Froney Crawford, in the shop, on the roof, and at the cash bar at Green Bank.

Charlie Katz contributed in discussions with me to many aspects of this work, from programming to typesetting. Andre Fletcher frequently listened to late-night lamentations on my work. He was providing me with references up to the week before my defense. Mike Schwartz, Carlos Cabrera, and Junehee Lee all helped me grapple with my data.

Felicia Brady and Anne Conklin glued the group together. Besides keeping a tab on the professors, they brought some of the outside world into the lab.

All these people are also my friends, and I want to thank them for helping me finish what I started a long time ago. In this regard the love and support of my parents Joe and Sheryl has to come first in acknowledging debts. They've kept me afloat me through all these self-centered years. I know I've been selfish, but really, did they expect anything else?

Thank you, Katya.

Dedicated to Milton and Hazel, Ben and Edith

Contents

List of Figures

List of Tables

Chapter 1

Introduction

This thesis describes three experiments designed to investigate the universe at high redshift. The most expansive by far is the Arecibo Search for Early Hydrogen, and detailed in chapters 2, 3, and appendix A. Chapter 6 describes observations of the gravitational lens 0957+561 with the Very Large Array, and interprets newly discovered faint emission in the context of a model for the gravitational lens. And in chapter 5 I describe our effort, joint with NRAO's Green Bank Tracking Station staff, in support of the VSOP Orbiting VLBI experiment: the M.I.T. Near–Real–Time Correlator. This is an instrument designed, built, and deployed by the author and several others at Green Bank Observatory to provide diagnostic assistance during the preliminary phase of the VSOP mission.

1.1 Arecibo Search for Early Hydrogen

Between recombination ($z \approx 1100$) and the quasars ($z \approx 5$) structures formed which today we observe in the hierarchy of galaxies, clusters, voids, and sheets. Theories of what happened in that interval are constrained by observations of the diffuse CMB and the appearance of discrete objects. We want to extend the lower bound by detecting protoclusters in collapse. We are trying to observe these in the hydrogen hyperfine line (λ 21 cm), at redshifts $4.7 \leq z \leq 5.5$.

The experiment is at the boundary of reasonable possibility. The expected signal characteristics depend on which of the large set of possible physical models is chosen. We

can use a very simple set of assumptions to estimate what might be seen; more particular cosmological models are suppositions. We write the total power flux

$$F_{rec} = \frac{\mathcal{L}}{4\pi D_H^2 z^2 (1+z)^2} f(\Omega, z, \ldots)$$

where D_H is the Hubble distance ($(c/H_\circ)h_{100}^{-1}$), taking $H_\circ = 100$ km/s/Mpc and scaling by h_{100}. f is a function of cosmological model. For simplicity we will set $f = 1$, appropriate for a Euclidean universe. The luminosity, if the state temperature is greater than the ambient cosmic background radiation temperature, is

$$\mathcal{L} = \frac{3}{4} N_H A h\nu$$

or, in units of 10^{14} solar masses (comparable to the baryonic mass of the Coma cluster)

$$\mathcal{L} = 2.4 \times 10^{39} M_{14} \quad \text{ergs/sec}$$

The total flux received in the redshifted hydrogen line, with the cosmological factor f (unity under our assumptions but can be calculated for particular cosmological models), becomes (with MKS units)

$$F_{rec} = 2 \times 10^{-21} h_{100}^2 \frac{f M_{14}}{z^2 (1+z)^2} \quad \text{W/m}^2$$

If the state temperature is close to the radiation temperature, or if there is ionization, F_{rec} is reduced.

The detectability of the hydrogen signal depends upon the velocity dispersion, the effective area of the antenna, and the receiver noise temperature. The expression above gives the total flux from a large hydrogen cloud, but it must be divided by the expected bandwidth to get the flux density. If we assume that the velocity width is 100 km/s, the expected flux density at 230 MHz ($z = 5$) is

$$S = 3 M_{14} \quad \text{mJy}$$

At such relatively long wavelengths, a simple feed can be used to illuminate a large fraction of the area of the Arecibo spherical dish, with a small penalty resulting from

the difference between the sphere and the best-fitting paraboloid. Based upon a detailed analysis, one can probably achieve a sensitivity of about 3.8 Kelvins/Jansky. The source temperature within the line, therefore, will be (assuming 70 kHz linewidth = 100 km/s) $\Delta T_{sig} = 6.3 M_{14}$ mK. One can expect a system noise temperature of about 170 K away from the galactic plane, and since the spectrometer will use 8-bit quantization, the sampling degradation will be negligible. There will be an observing time of about 180 seconds/day (drift time through the beam), and the rms fluctuation level will be $T_N/\sqrt{Bt}$, so the number of successive days required to get a signal $n_\sigma\times$ the rms noise is

$$t = 77 n_\sigma^2 M_{14}^{-2} \Delta v_{100}^{-1} \quad \text{days}$$

The scaling in terms of Δv for 100 km/s has been included in this expression. So about a year would be needed to detect a $10^{14} M_\odot$ primeval cloud at 5σ significance. But keep in mind that for such long integrations noise does not go down with $\sqrt{t}$; generally it declines much more slowly and may even fail to improve after some time, due to the contribution of 1/f fluctuations.

The expected signal is very weak. In order to make a detection in a reasonable time we exploit the large collecting area of Arecibo Observatory. Our experiment, installed in the summer of 1994, runs continuously and in the main independently of scheduled observations and the observatory upgrade. Dual broadband point feeds are mounted on the telescope catwalk where it intersects the focal surface, allowing continuous transit observations. The dedicated receiver includes low-noise pre-amplifiers, RF and IF filters and mixers, and a custom power-accumulating FFT spectrometer with 10-kHz resolution and 32-MHz instantaneous bandwidth (4k channels per feed). The spectrometer output is time tagged and logged to disk on a control PC, and digital audio data tapes are shipped biweekly to Cambridge.

1.1.1 Current Status

The search system has been running and gathering data, albeit in a single beam mode, since January of 1995. We first installed two helices of opposite polarization, but the

system is limited to a single feed because of feed-feed interaction problems. The one feed then came down for the very active hurricane season in the fall of 1995. Because the Arecibo maintenance staff have been busy with upgrade related tasks it took until March of 1996 for the feed to be reinstalled. We would like to move the feeds further apart or install the second one at some distance along the catwalk, giving dual declination coverage.

Initial data reduction showed our system temperature to be rather higher than expected. From late Fall of 1995 until our feed was reinstalled in March of 1996 we investigated whether we could significantly improve overall performance through a redesign of our feeds. The iterative process begins by formulating the desired electrical characteristics of a new feed. These are derived through computer simulation, taking into account the aberrated optics of the Arecibo spherical reflector, the placement and orientation of the feed, the geometry of the terrain, and the noise contributions from spillover, the celestial background, and our receivers. Then 9 GHz scale models are constructed and tested with special care given to sidelobe and polarization characteristics. The best models are then used in the computer simulations to calculate new estimates of system sensitivity.

The result of these efforts has been new helical feed designs with sidelobe responses 8 dB below our present feeds and system sensitivities 50% better. We have also identified the position and tilt angle for optimum performance. Although there is potential for improvement, we have held off construction of a full size feed while we look for other experimental parameters (frequency coverage, receiver temperature) that might be more dramatically beneficial.

During June and July, 1996 we upgraded our experiment. A switching noise source has been installed in the front end for calibration. Due to the fierce and variable radio frequency interference (RFI) environment it had been difficult to separate celestial signals, gain variations, and broadband interference. The computer controlled noise source was to allow us to do an absolute calibration over our entire bandwidth. Unfortunately as described in chapter 2, the scheme did not live up to expectations. Control software was improved too, especially in time-keeping and error capture. Daily status reports are automatically generated and emailed to us in Cambridge and Arecibo.

In this thesis I present the results of reducing approximately six months of the most

recent data, which amount chosen for its homogeneous characteristics. We do not achieve a sensitivity at the level generally expected necessary to observe protoclusters, but we can set upper limits on the HI masses of unobserved clouds that might be in our field of view. We do find appealing spectral and angular structures, but we must conclude they are likely of instrumental origin.

1.2 Near–Real–Time Correlator for VSOP Space VLBI

The Near–Real–Time Correlator is a test apparatus built in support of the VSOP Orbiting VLBI experiment. The satellite radiotelescope was designed, built, and launched by the Institute of Space and Astronautical Science (ISAS), the Japanese national space agency. NASA (through JPL) and the NSF (through NRAO) support the experiment by providing a network of tracking telescopes, adding capabilities to hardware and software used to reduce VLBI data, and providing assistance to the general international community of interested users. The satellite will observe with unprecedented resolution. Some of the targets include the cores of AGN and extragalactic masers.

The VSOP satellite was launched in February 1997 and has been producing images since July of that year. The preliminary check-out phase included demonstrating acquisition of the satellite by the tracking stations, and the successful detection of fringes on short baselines formed by the satellite and close ground stations. Normally the correlation of data tapes is performed at one of a few facilities; there are correlators for this mission in Socorro, Mitaka, and Penticton. The correlators themselves are very complex, and the failure to detect fringes may be due to an algorithmic problem in the correlator rather than in the data. For this reason it was decided a "quick look" capability would be advantageous.

The Green Bank 140′ telescope, near the tracking station, is capable of observing in VLBI compatible modes. If an instrument were built that could acquire a small amount of data simultaneously from the 140′ and the satellite via the tracking station, and diagnose the quality of the data perhaps even detecting fringes, it would provide very useful feedback to the satellite team.

In chapter 5 I describe the device our group installed at Green Bank for this purpose.

Much of the design and construction was done by the author, with the correlation software written by F. Crawford; The Green bank OVLBI team installed special hardware at the site to facilitate the experiment and provided large amounts of support. The custom hardware was built in the laboratory of Paul Horowitz at Harvard University, with advice and supervision by Jonathan Weintroub.

1.3 Low Surface Brightness Structure in Gravitational Lens 0957+561

The double quasar 0957+561 is the first example of gravitational lensing discovered. In chapter 6 I describe a project to create deep maps of the object and the field nearby. Our intention was to create the highest dynamic range map possible for the source by re-reducing the longest observations available in the VLA archive, and combining shorter observations.

We discovered several faint, previously unknown, features in the field. Some of the emission is very likely associated with the lensing galaxy, which is itself a radio source. But some of the features are consistent with being lensed background emission. In particular, one faint object falls near the lensed optical image of a background source; the two are consistent with a lens model developed from other constraints. The radio and optical emission is not associated, however. The radio emission is more extended, and if it is visible in higher resolution maps made with instruments such as the VLBA it could provide an additional constraint of the gravitational potential close to the center of the lens.

Chapter 2

Arecibo Search for Early Hydrogen Experimental Setup

This chapter describes the apparatus which we have designed, built, installed, and maintained at Arecibo Observatory in order to perform the survey for high redshift neutral hydrogen described in this thesis. The key difference between this and previous searches is the potentially unlimited observing time available to us by installing our own dedicated feeds away from the telescope's feed platform, and our own signal path from feeds through receiver to tape. This means we may operate for the most part independently of normal telescope operations, although hurricanes and power outages affect us as much as other observers.

Much of the design work was performed by J. Weintroub as part of his Ph.D. thesis (Weintroub 1998). Some is taken from pre-existing SETI designs by Paul Horowitz. The system has performed very well with a minimum of hardware or software related downtime.

2.1 Front End

A block diagram is displayed in figures 2-1, 2-2, and 2-3 The experiment has two dedicated feeds suspended from the catwalk near the paraxial surface. Initially these were two helices of opposite polarization, for two separate beams on the sky to confirm detections and identify RFI. Soon after installation however, it was determined they antennae were too

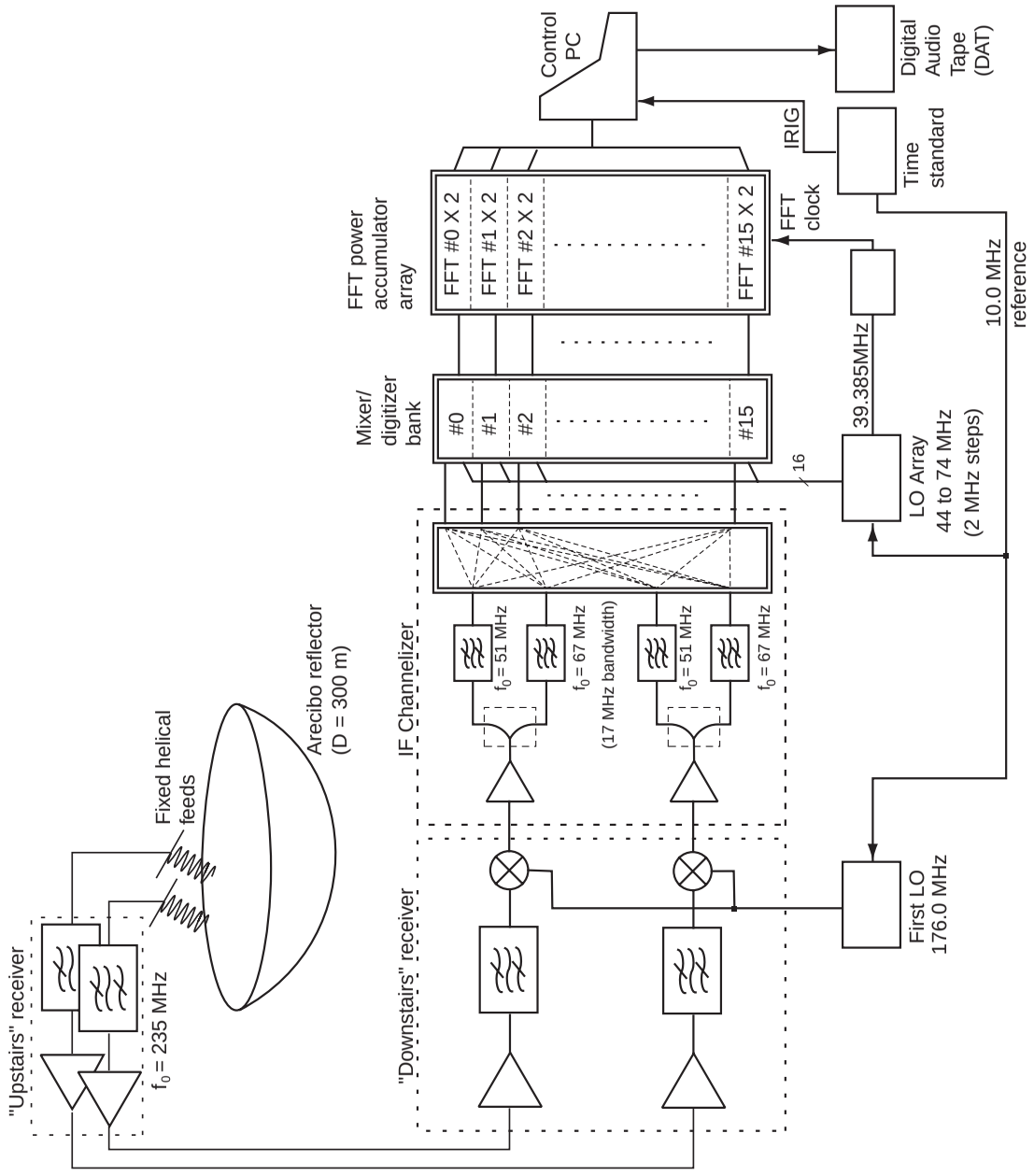

Figure 2-1: A simplified block diagram of the ASEH apparatus. Courtesy J.Weintroub.

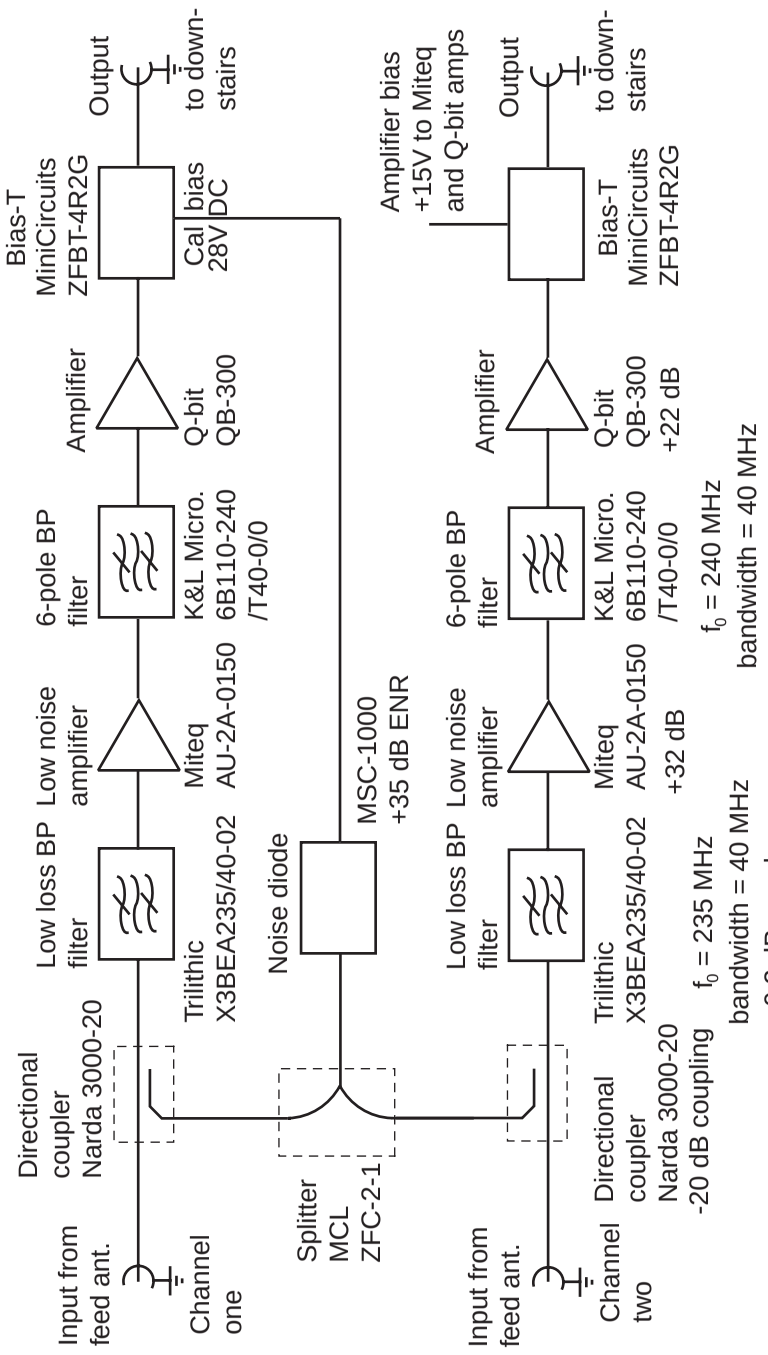

Figure 2-2: The front end of our apparatus from feed to second stage of the receiver. Courtesy J.Weintroub.

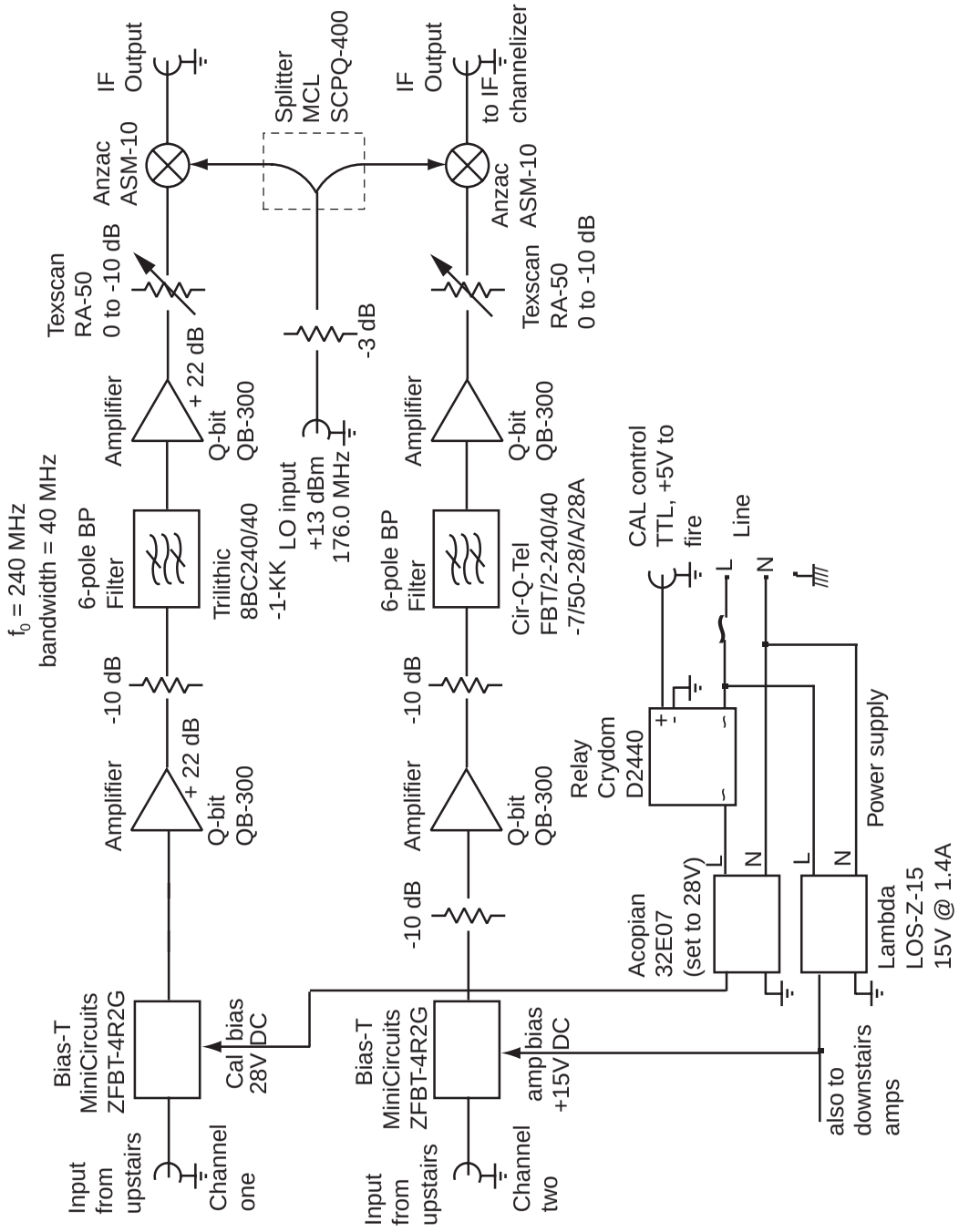

Figure 2-3: The "downstairs" receiver, including the second stage amplification. Courtesy J.Weintroub.

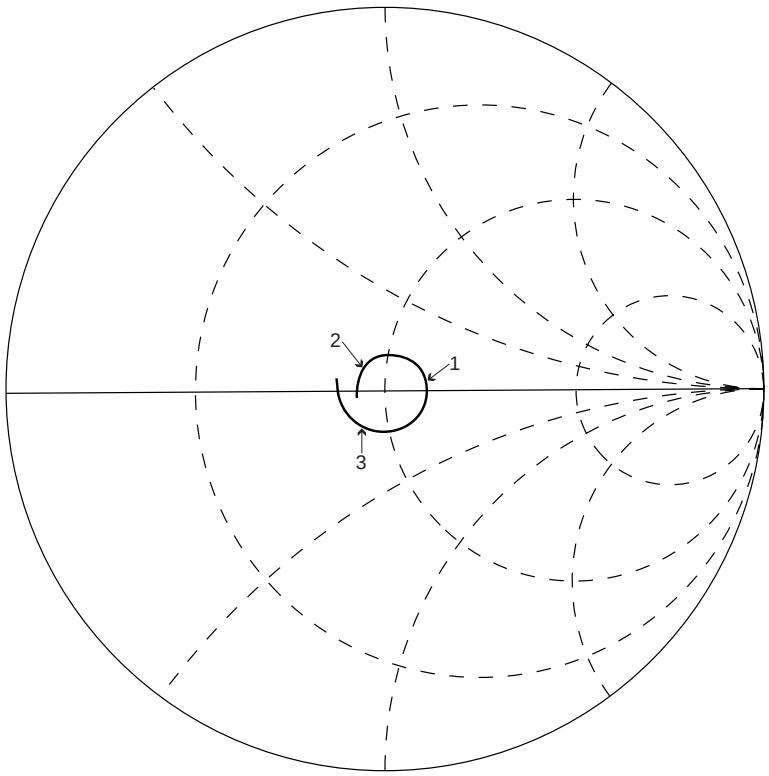

Figure 2-4: The impedance of our hanging feed, represented on a Smith Chart. Measurements took place on the catwalk in August 1997; the reference plane is the receiver end of the Heliax antenna cable. Frequency band is 210 MHz to 260 MHz. Marker frequencies and impedances in order are 235 MHz, $(63 + i)\ \Omega$; 219 MHz; $(45 + 6i)\ \Omega$; 251 MHz, $(45 - 9i)\ \Omega$. Measurements and figure courtesy of J. Weintroub.

close together and distorted each other's beams, so one was removed pending a feed design review (see Chapter 4). Due to time and resource constraints the second feed has not been re-hung.

Low loss Heliax cable connects the feeds to the pre-amplifier box sited on the catwalk. Each channel passes through an initial filter to suppress RFI near the observation band of 218 – 251 MHz. The signals are then amplified about 55 dB, filtered again and fed down low-loss waveguides to the second stage of the receiver in the control building. Figure 2-5 presents the receiver temperature contribution of the first stage. In addition, there is a noise diode which is always coupled into the front end before the first filter. It is powered by a DC voltage applied through the same waveguide from the second stage, and switched on/off via

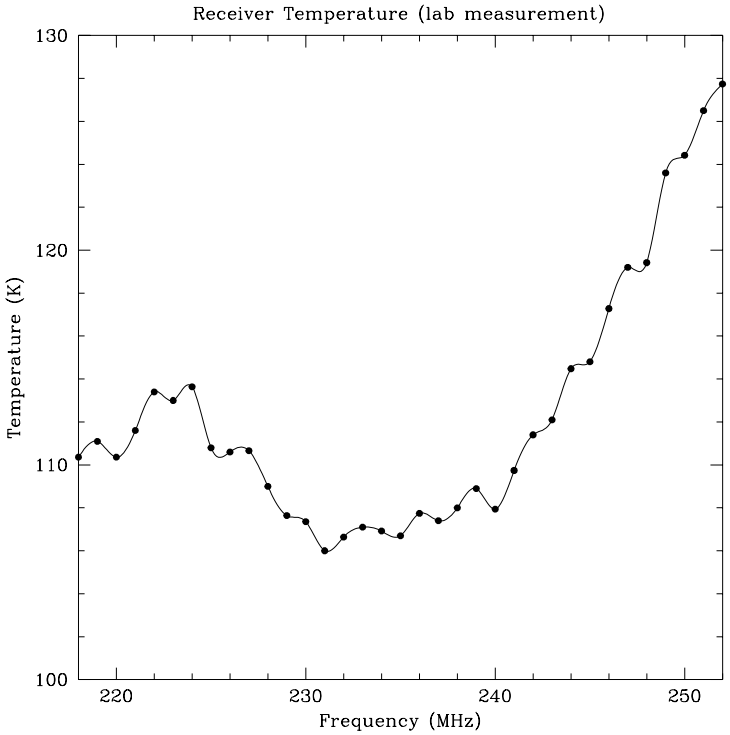

Figure 2-5: Receiver Temperature as measured on the bench in the lab. This is temperature of the first stage, the most important contributor to receiver temperature.

computer control. The purpose of the noise source is to calibrate the relative system gain over time, reducing errors due to gain fluctuations. The power from the cal unfortunately is not strictly white, but the spectrum does seem to be stable with temperature changes similar to day/night variations. Figure 2-6 shows the measured (bench top) excess noise temperature as seen by our system.

2.2 Back End

The second stage of the receiver consists of further amplification and filtering, and a mixing down from the sky frequencies to the band 43 – 75 MHz. The signal from each channel is split into 16 and amplified, and each individually mixed down to baseband with the local oscillator array frequencies from 44 to 74 MHZ. Each stream is conditioned, digitized and

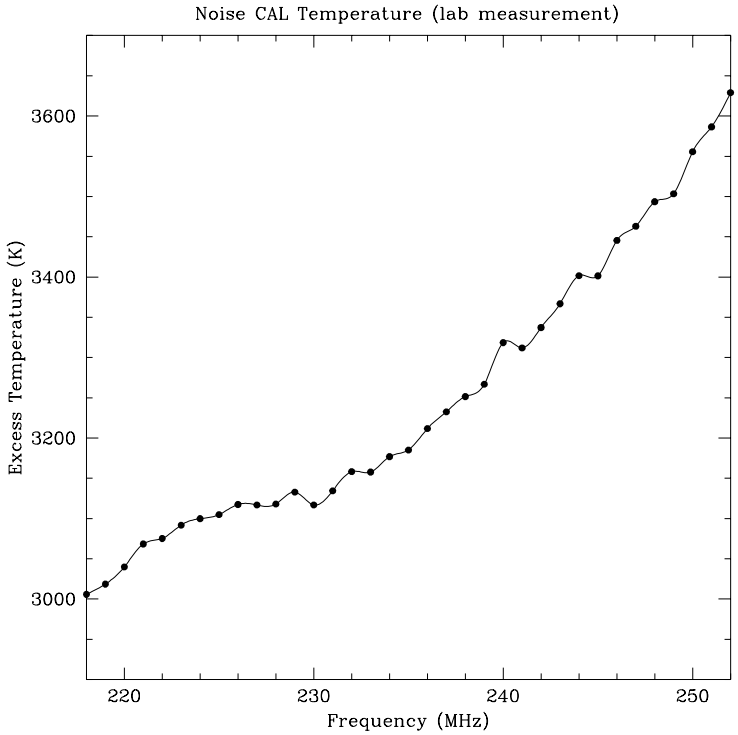

Figure 2-6: The excess temperature of our noise CAL, as measured in the lab.

fed into the FFT engines.

The FFT Spectrometer Power Accumulator (SPA) boards are based on a dedicated FFT chip by Austek, and designed by J. Weintroub to perform seamless Fourier transforms and accumulations, allowing integration times of from 102μs to 20s. The 32 SPA boards are configured over a serial interface. Buffered data are presented on a shared bus, and each board is addressed uniquely.

The system is controlled by a '486 CPU PC running custom software over the MS-DOS OS. It configures the SPA boards over a serial line and latches data from the SPA data bus via a custom interface card. Data rates are slow, an average 1.6KB/s, so there is no problem passing it through the PC ISA bus to disk storage. Once a day the system is suspended and data are logged to a Digital Audio Tape (DAT), which can store 2 GB total or about 13 days of data. The results of hardware self tests, parity and overflow errors, and other

diagnostic information are written into the data records.

Timing information is supplied by Arecibo Observatory in the form of an IRIG-B encoded time signal derived from the Observatory's maser clock and decoded by a custom hardware interface to the PC. Unfortunately standard PC clock hardware is rather poor, so between periodic syncs to the standard the local clock may drift up to a second. If the house clock signal is unavailable, the control software attempts to query a computer on the local net for the time. However, without frequent update by the observatory standard, over 24 hours the PC clock my drift by several minutes.

After logging data to tape the disk is cleared. A status message is uploaded to a workstation on the LAN which is later emailed to us and the telescope operators. If any hardware errors were reported during the prior data run they are included in the message. Further, if the status file fails to appear by a specified time, if for example the PC has crashed, we are automatically informed by email. DOS-based programs are notoriously unstable due to primitive memory management, but we have been free of these problems. The system has run unattended for months at a stretch.

2.3 Experiment Time-line

In 1991 Burke, Conner, and Lehar conducted an RFI survey at Arecibo Observatory to determine if an experiment like this was possible. The results were positive. In the spring of 1993 Weintroub designed the SPA board, prototyped it that summer, and went into production in the winter. Other hardware modules, such as the mixer–digitizer boards, power splitter, and local oscillator array were constructed by Weintroub, the author, and others during the winter and spring of 1993-1994. The first version of the control software was written by Darren Leigh and the author during the spring of 1994. The first and second receiver stages were built by NAIC at Arecibo. The apparatus was installed at the observatory in July and August of 1994, and commenced autonomous regular observing in late December, 1994.

The system hardware has run relatively problem–free; there was one power supply failure and a hardware failure due to a bad batch of microcontrollers. An amplifier in the upstairs

box burned out and was replaced. The PC monitor failed but this did not interrupt data taking. There have been several software upgrades to correct minor problems, but data has not been corrupted by these. The most intrusive presence has been the Arecibo Upgrade project, which has occasioned downtime due to power outages and equipment upgrades, lack of time for support on site, and increased RFI. The upgrade changes will not improve the performance of our system, except for the new ground screen lowering spillover loss (see chapter 4). It will, however, much improve conditions for normal observers. During the very active hurricane season of 1995 the single helix mounted was removed and not replaced for many months. Each time the helix is moved our pointing changes slightly, potentially complicating data reduction. One time the waveguide from the catwalk to the control building was disconnected as a weather precaution, and not reconnected for weeks. These are the pitfalls of remote, unsupervised operation. The only operator interaction normally required is the replacement of the archive tape every two weeks.

Table 2.3 shows the up/down time of the experiment from first light in July 1994 until the present. The system is still running and data are being logged. It might be valuable to acquire data in a post–upgrade environment. Upon completion of the experiment the apparatus will become observatory equipment.

2.4 Data Reduction

2.4.1 Data Format

Instrumental Peculiarities

Although the hardware consisting of the front and back ends of our receiver has functioned very well, considering that it is operating in the main unattended and thousands of miles from the experimenters, the data acquired over the operating life of the experiment are of nonuniform properties that make them sometimes difficult to reduce. The spottiness arises somewhat from hardware errors, but is mostly due to "human factors." In this section I will describe format of the data format as it is produced by the apparatus, and point out the important instrumental effects.

But before discussing the digital data I will describe some instrumental problems that

date	event	comments
07/10/94	data taking first started	2 feeds, 8 kilochannels
10/24/94	2nd helix canted 30°, disconnected	feed interactions
11/15/94	2nd helix taken down	feed interactions
01/20/95	remaining helix repointed 10° S	gain ↑, noise ↓
	RFI monitor disconnected	
01/23/95	RFI monitor reconnected	
01/31/95	feed position measured	
'soon after'	one catwalk tiedown loosened	upgrade activity
02/08/95	feed moved one hanger inboard	improve gain, see chapter 4
02/20/95	catwalk tiedown tightened	upgrade activity
08/95	flatline, front end amplifier failure	replaced on this date
08/27/95	helix removed; replaced by load	hurricane season
03/15/96	helix replaced, restarted	pointing per chapter 4
08/96	CAL installed	CAL software upgraded
09/09/96	hurricane Hortense	6 in. coax disconnected
09/26/96	6 in. coax still disconnected	no power to front end
10/03/96	power restored to front end	
10/14/96	channel 1 down	
10/14/96	RFI monitor misconnected to ch 1	date of diagnosis
10/15/96	ch.1 repaired, helix replaced	restarted
12/96	Antenna disconnected, S-band tests	upgrade activity
8/1-6/97	front end shutdowns	noise measurements
8/5/97	new LO array	replaced borrowed unit
8/6/97	Antenna switched to ch. 2	lower noise channel
10/08/97	system shut down	bad DAT tape drive
10/20/97	restarted	DAT replaced
11/4/97	noticed ch 1 flatlined	inactive channel, data ok
11/20/97	CAL shutdown	noticed CAL misfiring
2/7–20/98	no status messages, data OK	network problem

Table 2.1: Chronology of system faults, courtesy J. Weintroub (Weintroub 1998). This list is not a complete account of all conditions occasioning data problems.

precede them. Table 2.3 details changes to the system that have either stopped data taking or changed its character. Some cause only loss of data. For example, during hurricane season Puerto Rico is often in the track of storms, and there are elaborate safety precautions taken by Arecibo Observatory when hurricanes threaten. At that start of the particularly active season of 1995, our feed was removed from the catwalk. However, due to the pressure of the Arecibo Upgrade project on manpower, we were unable to reconnect our feed for 7 months. Being absentee observers, we could not apply the sufficient pressure. The lag between data logging at Arecibo and shipment to Cambridge also can be a problem. In September of 1996 the front end signal and power cables up the catwalk were disconnected in preparation for hurricane Hortense, but then not reconnected. We didn't notice the data was void until it was shipped up and inspected a month later.

At some points the character of the data has changed in a way that must be diagnosed during reduction. For example, on February 8th, 1995, the feed was moved, the goal being to improve optical sensitivity. A consequence of the move is a shift of beam position on the sky. If one wishes to coadd data prior to and following the move he should be careful to make sure the beams do overlap sufficiently. As another example, In July of 1996 we installed a calibrating noise source whose pulsed signal is injected into the system at the front end. This fundamentally changes the way one must use the data logged to tape. Soon after a new amplifier was installed, changing the system gain and frequency response. Smart reduction software should remember or detect all these changes and do the appropriate things to the data.

For the purposes of this thesis, I have decided to only reduce those data that were taken after the calibrating noise source and new front end amplifier were installed. That limits the data volume to about 14 month's worth (about 59 GB of raw data). A post-observing hardware error limits the volume even more. On about 30 October 1996, the tape drive logging our data began to fail, writing data only it can read, until the problem was discovered in the summer of 1997. The faulty drive was replaced and shipped to Cambridge where we were able to salvage several months worth of data before it failed more disastrously. It may be possible to recover more data, but not within the time constraints of this work. Therefore, the data reduced in this thesis cover approximately the observing

dates 06AUG97 to 22FEB98. This leaves out a substantial amount of older data, but it also smoothes reduction because all the data are in the same binary format. I take the position that the analysis described in this thesis lays the extensive foundation for further work employing more refined techniques.

Digital Data

The process of data logging is basically thus: the control PC resets the spectrometer over a bussed serial line, issues commands to configure and sync the individual FFT engines, starts them running and then waits for a signal that the first integration's data are ready. It then services the boards and stores the data to disk along with time tags and status bytes. Everyday at 10AM local time it stops data logging, writes the data file to tape (or deletes it if there is some tape problem), emails the observers a status report, and then repeats the process. Every time the computer is manually interrupted from data logging, or boots up (as after a power failure), it also informs us via email. This way we have a fairly complete record of up/down–time and can be made aware of certain problems before the data tapes are shipped up.

Within a 23.5-hour-long data file, a single record consists of 32 256-point spectra, each one coming from a different Spectrometer Power Accumulator (SPA) board. Sixteen correspond to channel 1, the signal path from the helix, and the other 16 to the other signal path, which for the time range considered here starts with a 50Ω termination. An example of a single 256-point spectrum (of white noise) is shown in figure 2-7. Each datum is a two-byte unsigned integer, so power can be presented by 65536 digital levels, including 0. Although these are enough levels so that quantization noise will not be a problem in our analysis, the upper limit does cause us a "wraparound" problem that will be described. The shape of the spectrum in figure 2-7 is due to effect of the various stages of gain and filtering in the signal path, and represents our system's response to a particular frequency subband of 2.25 MHz within the total 32 MHz. In particular, the lazy ripples and sharp shoulders are due to the anti-alias filters in front of the A/D board that handles this subband. To produce final spectra the system response must be accounted for. Figure 2-8 shows the average response of all the subbands comprising channel 1; in addition to the individual

SPA board gains the response of the pre-amp filter is visible, lowering boards 0 and 15 relative to the middle ones. This figure represents our relative gain across the observing band, assuming our terminator is perfect and the cables and connectors do not impose any frequency-dependent loss.

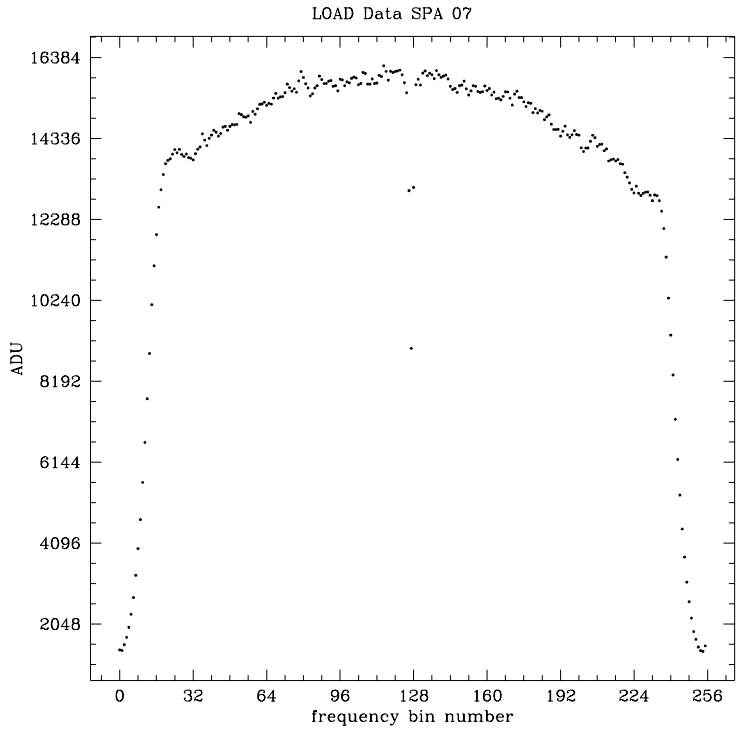

Figure 2-7: Example LOAD Spectrum, produced by a single SPA board when the system is terminated by a matched LOAD rather than the feed.

The previous figures presented the spectrum of white noise, so that the reader might have an idea of the "Platonic ideal form" of a spectrum produced by our instrument. Figure 2-9 shows a typical to good mid-day spectrum of the radiation coupling to our feed. Radio-Frequency Interference (RFI) is a severe, and worsening, problem. It is such that for most of the day most of the observing band is unusable, and even estimating the non-RFI baseline is problematic. Fortunately, for a few hours very early in the morning the environment is quieter, figure 2-10. In this thesis I have reduced only data taken between 01:00 and 05:00 hours AST (Atlantic Standard Time).

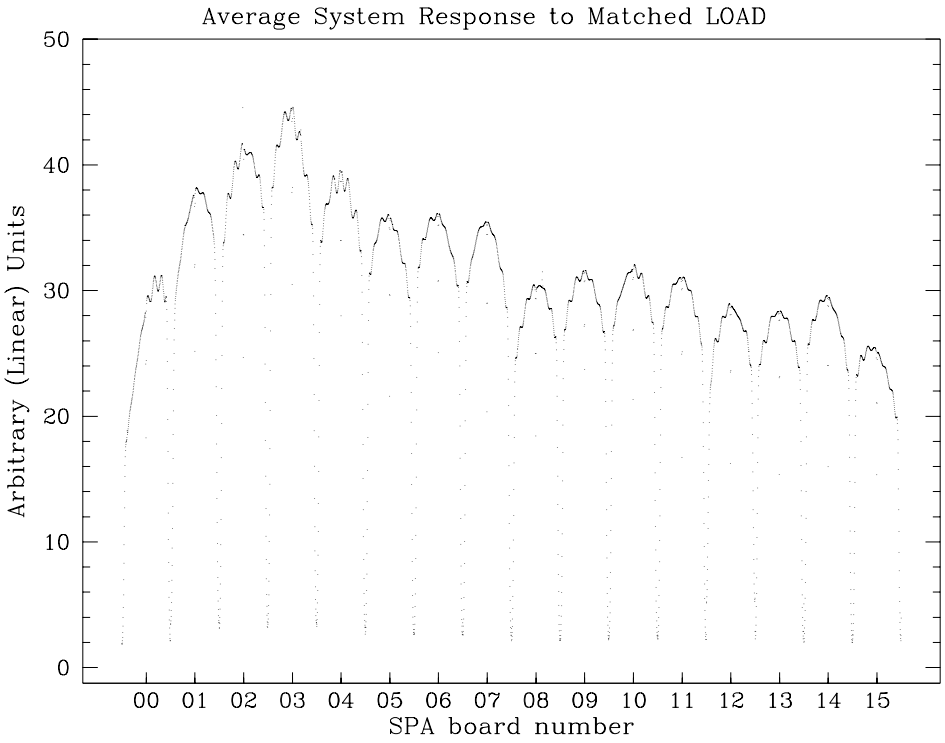

Figure 2-8: System response to white noise over full band.

Because of the problems associated with reducing data in the presence of RFI and gain instability, we installed the calibrating noise source whose signal is injected into our system at the front end. We have measured the noise equivalent temperature of the source over our frequency range, and it is not white, a feature which will work its way into the data. Another problem with the CAL, from an algorithmic point of view, is that it is sufficiently bright that it sometimes pushes the system temperature over 65535 digital units. Fortunately, the SPA boards have more than 16 bits of dynamic range; it is only that we have chosen which 16 bits to take as data. So we lose the most significant bit, and the data values appear to "wraparound." I have written software to detect when this occurs and recover the true spectrum. Figure 2-11 shows this happening when the CAL fires, in a data file which is LOAD data (*i.e.* the feed is disconnected, and the input to the front end is a 50Ω terminator).

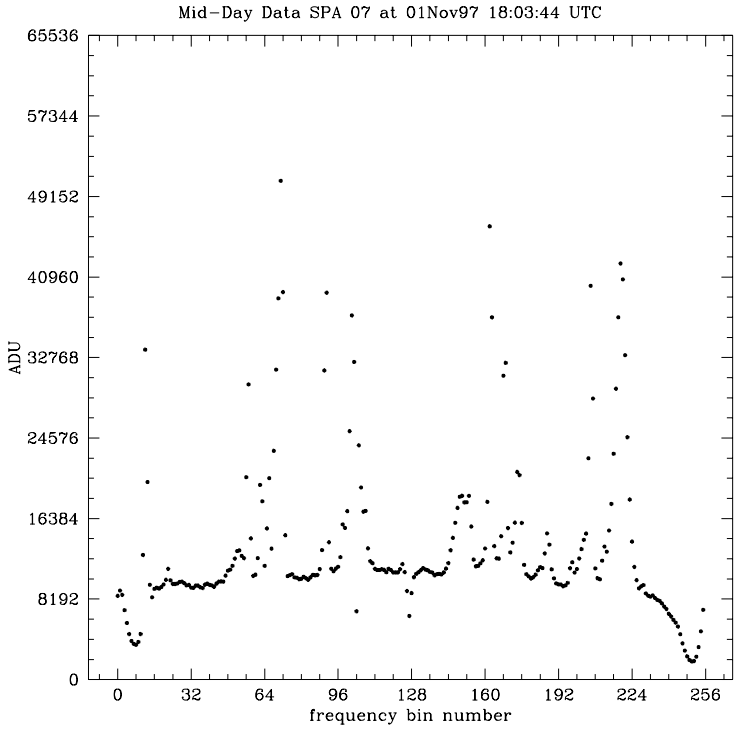

Figure 2-9: Typical–good example of mid-day RFI environment.

Unfortunately, the CAL data does not provide as useful a diagnostic as expected, because of the following: figure 2-12 shows two consecutive integrations of LOAD data, one with the CAL off and one ON. Apart from an offset and perhaps small slope they are the same. Their difference would be the system response to a known source, hence a calibration. Figure 2-13 shows that difference, and also a difference spectrum when the feed is connected instead of a matched load. Notice the large frequency-dependent difference. This is probably due to standing waves in the system, set up by a mismatch between the first filter and the hybrid coupler injecting the CAL signal. The waves are not present in the CAL off data, so this renders a bin-by-bin calibration impossible. Even if the waves are stationary in time, the uncertainties introduced by fitting and removing them, in addition to the bins lost to RFI, make it unworth the effort. I have instead used the CAL integrations to perform a rough gain calibration at the subband level in such a way that whatever error is introduced by

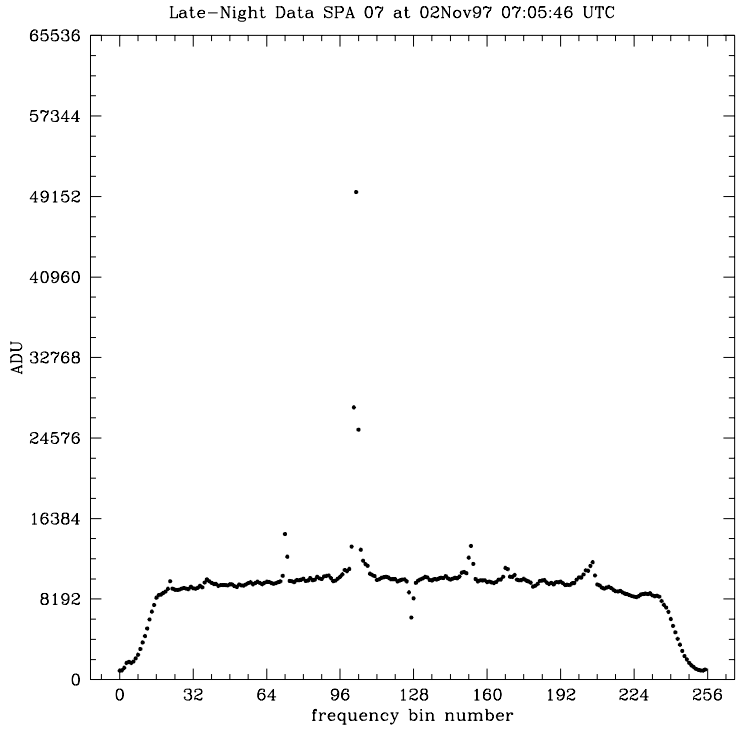

Figure 2-10: Typical–good example of late-night RFI environment.

the standing waves is a constant, as will be described. In fact, due to the possibility that the mismatch causes CAL power (which is considerable) to be reradiated by our feed into the Arecibo dish, we have disconnected the CAL indefinitely.

One more hardware issue affecting the data: there is a particular hardware bug, due to largely unknown causes, in which a SPA board outputs scrambled data (figure 2-14). The problem has something to do with long clock lines or underdriven busses, or some such reason which so far has been impossible to duplicate in the lab. Having failed to find a decryption algorithm for such data, I have written software to detect it and flag the data as unusable. The bug occurs randomly, but typically one or two boards (out of 16) per data file are corrupted in this way.

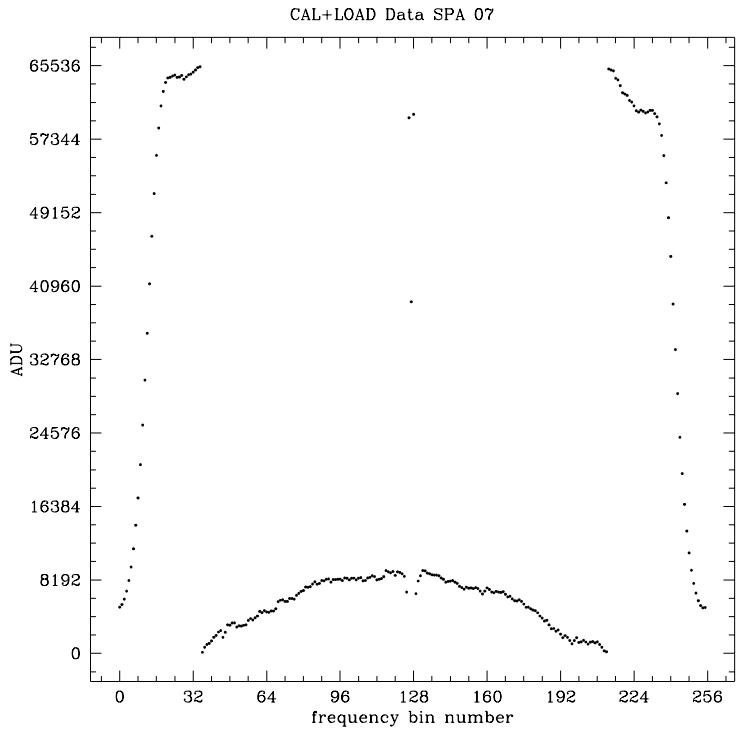

Figure 2-11: Digital wraparound caused by dynamic range overflow.

2.4.2 Reduction Procedure

Even with the limitations described above, there is a very large volume of data that must be reduced, necessarily in a piecewise fashion. A pipeline of data reduction software has been developed in which the base unit of data reduced is one DAT tape, about 2 GB. In this section I describe the manipulations performed on the raw data in the pipeline, and the finishing work on the results of many runs through the pipe.

One tape holds 13 days of data. By inspection of the email log of status reports from the computer I eliminate any data files wherein the computer detected either a faulty time code or one of various hardware errors. Our time standard is ultimately from the Observatory maser, encoded in IRIG-B format and supplied to us over coaxial cable from the encoder. Often the encoder malfunctions or is turned off, but data acquisition software which I wrote detects these departures and signals an error condition. The software then shifts to

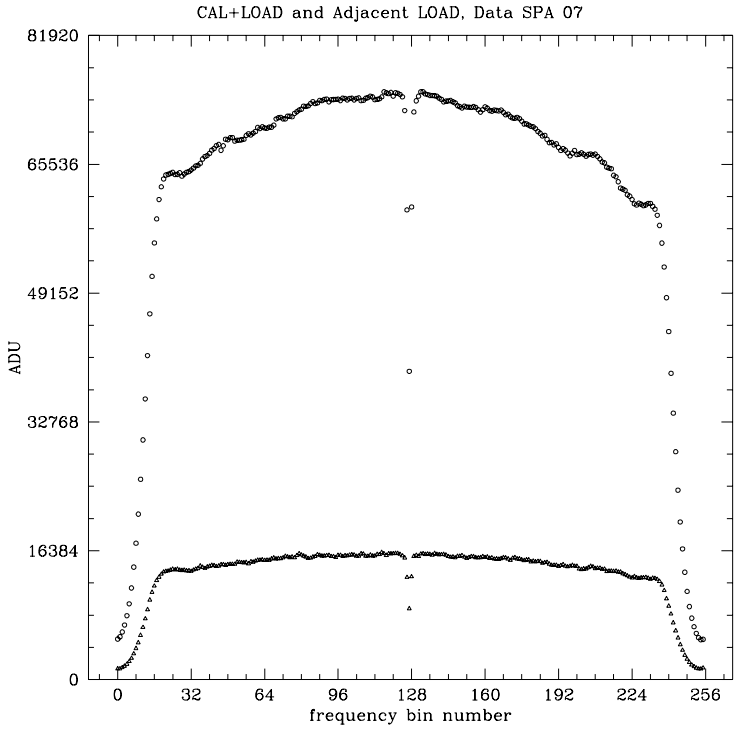

Figure 2-12: The higher spectrum is an integration when the CAL fires with 50Ω load terminating system. The lower one is the adjacent in time LOAD only spectrum.

the crystal clock internal to the computer. Unfortunately, I have found that this clocks drifts as much as 1s/300s, or two beams/day. Rather than try to back out the correct time I discard the data.

Only data taken between 01:00 and 05:00 AST in reduced. The spectra are inspected, and any affected by the "startup bug" described are flagged. The calibration procedure is graphically represented in figure 2-15. A time ordered set of raw spectra is formed, such that the outer two are CAL+SKY integrations. Because of turn on/off transients, the two spectra immediately adjacent to each CAL+SKY spectrum are unusable, so I use the next closest. Two difference spectra are computed, the difference between each CAL+SKY spectrum and its closest inner SKY neighbor. If it were not for the standing waves described above, this spectrum would represent the effect of system gain on the CAL output only, the contribution from SKY having been removed. One could then normalize each bin of

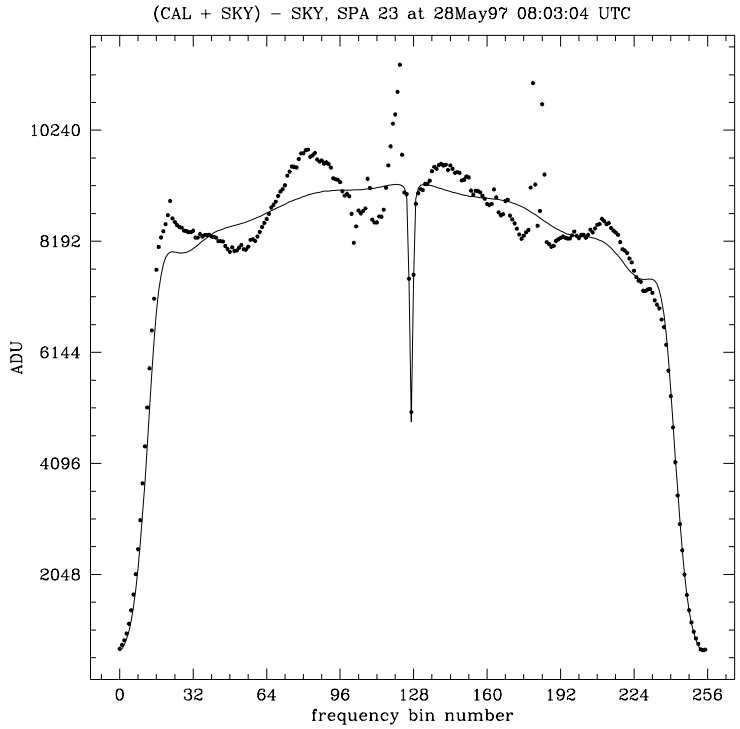

Figure 2-13: The solid line is the difference spectrum of the two traces in figure 2-12: (CAL+LOAD)-LOAD. The dotted trace is the same when the feed is connected: (CAL+SKY)-SKY. Note the standing waves.

the intermediate SKY spectra with an interpolated value from these two difference spectra, removing gain drifts in time and the gain shape in frequency of the spectrum. But because of the standing waves, present only when CAL is on, this would introduce spurious features in the resulting spectra. Also, RFI will frequently contaminate many bins in the difference spectra (recognizable half the time because the difference bins would be negative), making these frequencies uncalibratable.

As a consequence, what I have done is sort the difference spectral bins in order of power, and employed the 33%ile point as the normalizing value. By experience I have found that sorting in this way differentiates strong RFI, which has a broad spread of brightnesses, from the baseline, which sorts to a plateau of characteristic value (figure 2-16). It in no way eliminates broad-band RFI. The standing waves, to the extent they are stationary (which

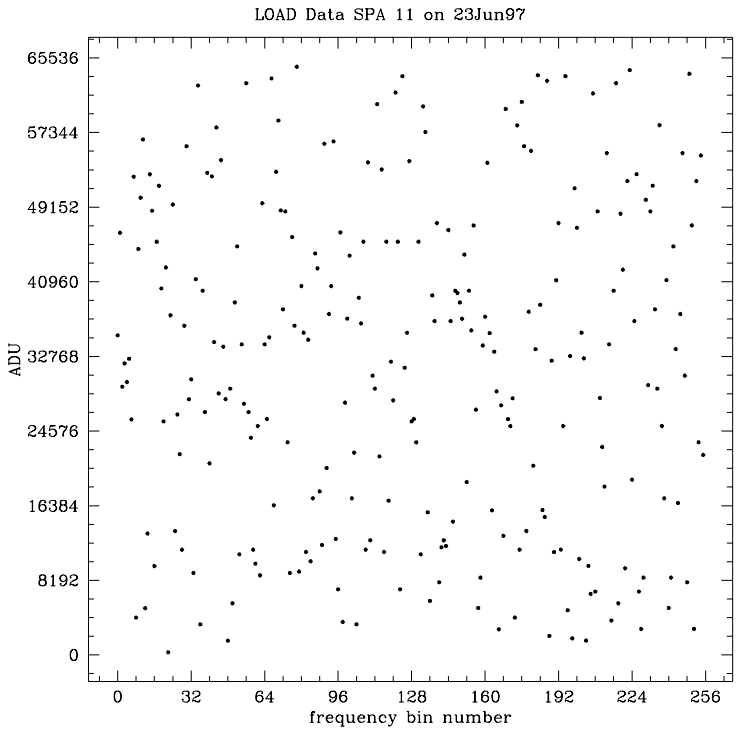

Figure 2-14: The data-scrambling start-up bug.

they appear to be over timescales of days) will modify the value picked by sorting, but always in the same way. Thus I can remove the effects of gain drift, but not remove the frequency structure of the gain function. I will describe later how I accomplish that. The normalized spectra are written out, along with the Local Mean Sidereal Time of observation, and the radial velocity of the receiver to CMB rest frame. To calculate the latter we need to know the direction of observation, which we do to sufficient accuracy from the measured position of the feed and geometrical optics. The expected pointing has been confirmed by observations; during trials of a new pulsar machine, built and installed by Joseph Taylor's group, we donated air time with our feed and a known pulsar at declination -7° was detected. Coupled with this, the observed transit time of the Galactic plane through our beam puts it at an Hour Angle of -15 minutes.

The next step of reduction is to resample the data to common LMSTs. For the purpose

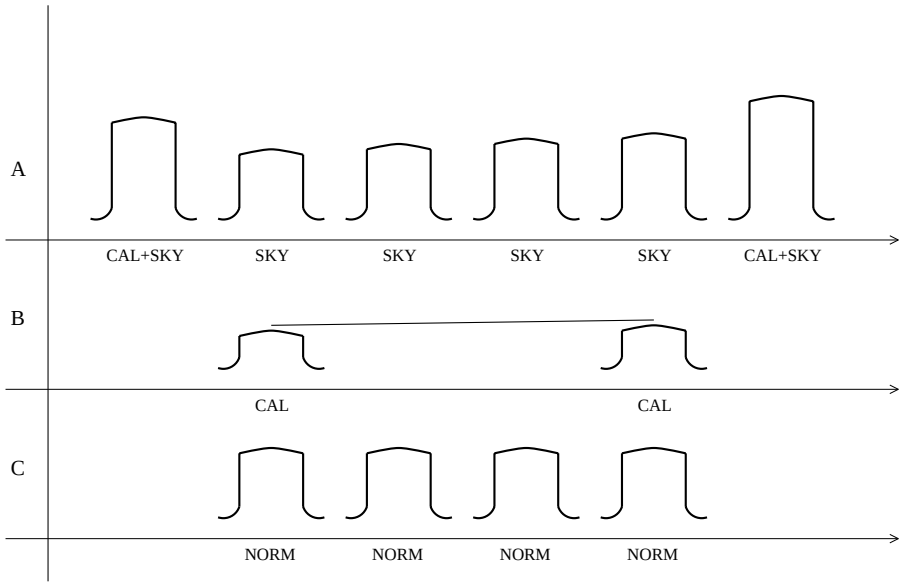

Figure 2-15: Calibration procedure using CAL source.

of coadding, it would be convenient if all data points lay at precise LMSTs. Our integration time is approximately 10s per spectrum, or about 18 per beam, so we are heavily oversampled. Oversampling makes RFI detection easier, so we would like to preserve this headroom in the process of resampling, but also we would like to filter as much RFI out at this stage as possible. I implement resampling by use of median filtering with a stretchable window, resampling at the rate of 4 per sidereal minute, or about a factor of 2/3. The window stretches to grab three good points, avoiding missing values during CAL cycles, which are of known duration. If no unflagged spectra are available within a certain maximum window size, the output data is flagged as unusable.

The resampled LMST data files are split into half-hour chunks, a convenient size, and set aside. The above process is repeated on every raw file, and then the individual split data files are coadded. Specifically, a coadded spectrum at a certain LMST is the median of the approximately 13 spectra at that LMST. Of course LMST drifts with respect to UTC, so start and end LMSTs of the earliest raw data file of the set are different than those of the last. For this reason there will be only one or a few data files that cover a border half hour of LMST. I do not average these; I hold them until the next data tape is processed,

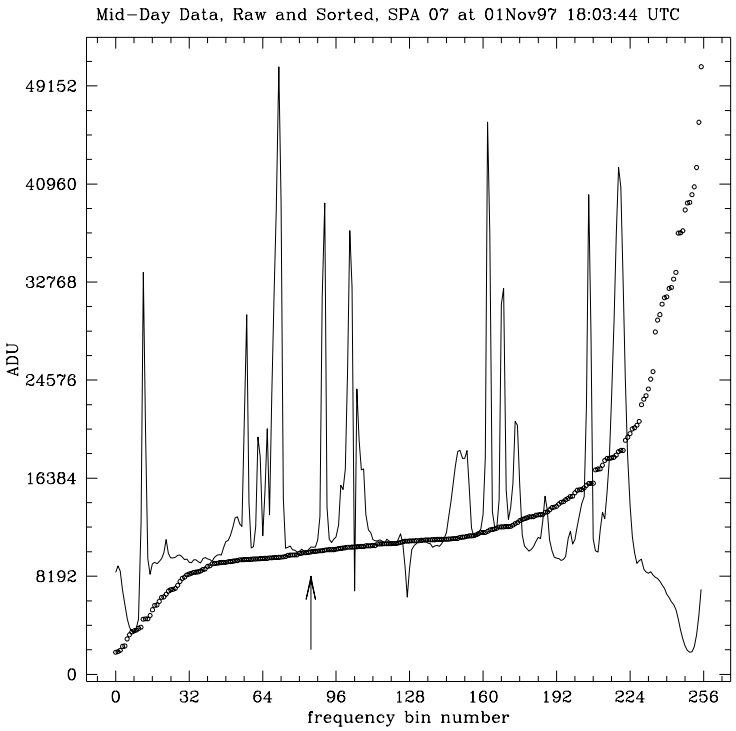

Figure 2-16: An RFI corrupted spectrum, sorted by intensity. The arrow indicates the position of the 33%ile point used as an estimate of the baseline.

which, if in chronological order, will have more data at that LMST and make for a happier average.

The basic unit of data volume is one DAT tape. A tape at a time is reduced and coadded. About a dozen tapes were pushed through the reduction pipeline in this part of the analysis, and the reduced half hour chunks were stored until the end and then coadded the same way individual days were. The motion of the Earth about the barycenter produces a noticeable frequency shift – up to 4 bins ($\approx$ 40 kHz) over 6 months. Although I do keep track of the SSB-frame frequency of each observation, I chose to ignore the effect when coadding spectra of large UTC separation. 40 kHz is much narrower than the signal of interest, and it saves much book–keeping and disk space. Not handling the effect rigorously will smear narrower signals out, if such exist in our data set; but one must decide what is most important and in the present discussion it is the protocluster signal that we seek.

After reducing data from the aforementioned dates, we have produced spectra covering the LMST range 22:00 to 09:30 hours. Now, the frequency dependence of the gain can be removed in the following way. Denoting frequency bin within a board by i, and the relative gain as a function of frequency by g_i, system temperature at frequency i by T_i^S, the datum produced so far for each bin is (in the absence of RFI, and slightly modified by the standing waves)

$$V_i = \frac{g_i T_i^S}{\langle g_i T_i^C \rangle_m}, \tag{2.1}$$

where T_i^C is the noise temperature of the CAL source, and $\langle\ \rangle_m$ denotes the median of the set. In figure 2-8 I showed an average of the system response when the inputs are matched terminators (presumably white noise). I can compute the same profile for the response to CAL only, with the same data, by means of the differencing described above in reference to calibration. What one gets from that, being careful to remove the effect of gain and temperature variations by renormalizing each spectrum before averaging, is just the shape of the response to CAL, $\beta g_i T_i^C$, where β is some constant. If one then sorts, takes the median,a nd normalized by that, he can form

$$V_i' = \frac{g_i T_i^S}{\langle g_i T_i^C \rangle_m} \frac{\langle g_i T_i^C \rangle_m \beta}{g_i T_i^C \beta} = \frac{T_i^S}{T_i^C} \tag{2.2}$$

which is what one wants, the system temperature in units of the CAL temperature at each frequency. Unfortunately the CAL is not flat across our band, but measurements on the bench indicate it is at least stable over time and temperature. Finally, the individual 256-point spectra of each SPA board are concatenated, with overlapping frequencies averaged, to form a single 3376-point spectrum covering the entire band. The CAL frequency dependence has been measured on the bench, so we can remove it after coadding all the data.

System Performance

Before discussing the final analysis of the coadded data, there were some diagnostics performed to evaluate system performance. One upsetting fact is presented in figure 2-20, where apparently no continuum sources have been detected over a thirty minute stretch of right ascension. In older data we *have* seen continuum sources which repeat day to day in

regions of low Galactic foreground. Between then and now something has changed; perhaps the raising of the Gregorian enclosure at Arecibo has drastically increased aperture blockage for us, or reflects broadband RFI into a previously blind sidelobe.

I undertook an unsuccessful search for the Moon. The Moon should just about fill our beam, and at these frequencies should appear as a thermal source of approximately 220K. It will pass through our declination twice a month. I calculated the Moon's topocentric coordinates and examined all data when it should have been within a few degrees of our expected pointing. The Galactic background at our frequency varies from 90K, typically, to about 1300K in the plane. So the Moon will appear bright or dark depending on Galactic latitude. I couldn't find it. This indicates that the system temperature is higher than expected, since a large change in the sky contribution did not result in a significant excursion. An interesting possible improvement is to search for the Moon in spectral lines, namely reflected RFI from TV and military radar in Earthshine (Sullivan & Knowles 1985). The video carriers can be thousands of Janskys bright. In my search I looked only in total power after excluding strong spectral features.

Fortunately, we still unambiguously detect the Milky Way as it transits. I have used observations of the plane of the Galaxy to estimate our system temperature and gain. Taking surveys of the sky at two bracketing frequencies, 408 MHz (Haslam *et al.* 1982) and 35 MHZ (Dwarakanath & Shankar 1990) I computed the spectral index and then the the expected brightness temperature on the sky, taking into account the different survey resolutions and our large fractional bandwidth (32 MHz/235 MHz). With this synthetic map, one may construct a model of the system temperature as a function of beam position, and receiver and other non-sky contributions to system temperature (including spillover). Figure 2-17 presents this model of the sky contribution to $T_{\rm sys}$. The best–constrained fits will be where the temperature variations are largest, so taking a data set wherein the inner Galactic plane transited in the very early morning I computed an estimate of the baseline power and fit it to the model. I assume the uncalibrated digital data counts can be related to $T_{\rm sys}$ in Kelvin by

$$D(\mathrm{LMST}) = K(T_{\rm model}(\mathrm{RA} + \mathrm{HA}) + T_{\rm misc}) \tag{2.3}$$

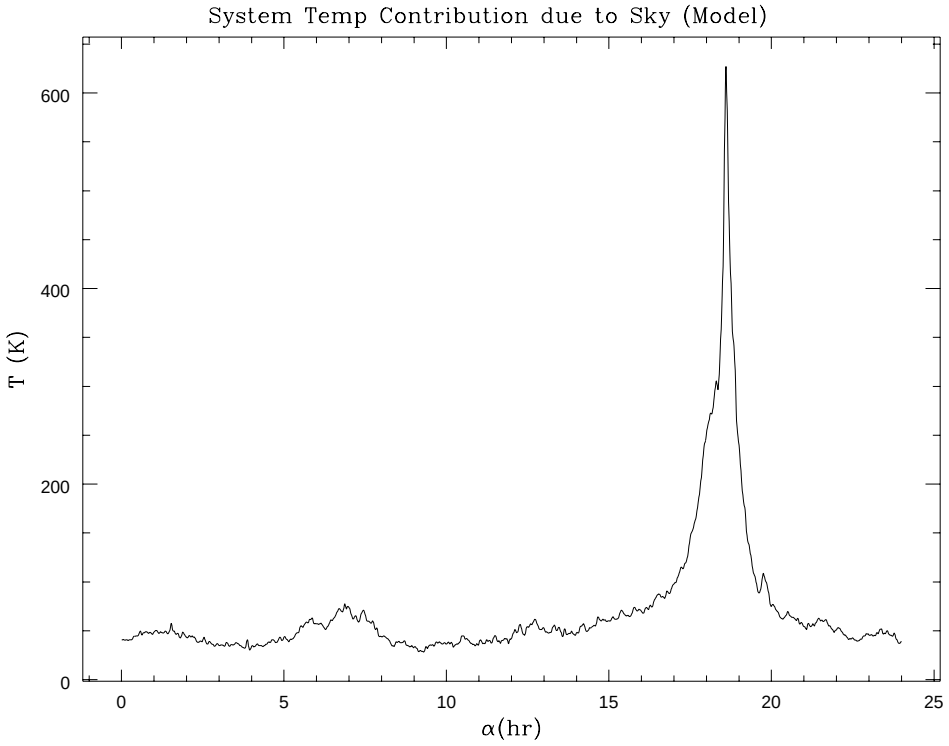

Figure 2-17: The expected temperature contribution of the sky to $T_{\rm sys}$, with right ascension (at declination -7°). To get $T_{\rm sys}$, add to this contributions from spillover, receiver noise, line loss.

and fit for HA (hour angle), K, and $T_{\rm misc}$. K will be vary over time, so this is just an order of magnitude estimate when applied to any other data set. I expect $T_{\rm misc}$ to be roughly constant over other data sets, unless broadband RFI makes a significant contribution to $T_{\rm sys}$. Each SPA board has a gain which can vary separately, so I fit each board separately. Example fits are shown in figure 2-19, and full results are tabulated in table 2.2[1]. First, note that although I think it's fair to say the model looks much like what is observed, there are clear systematic differences. I do contend the match is good enough to derive rough but believable estimates of fitted parameters. The non-sky contributions to $T_{\rm sys}$ are rather higher than we had expected, but consistent with the null results of the Moon search. I

[1]Very shortly before submission of this thesis an error was found in the construction of the Galaxy model described above. The effect of the error on the $M_{\rm HI}$ limits derived in the next chapter is such that they are underestimated, and should be revised upward by a factor of order 1.3

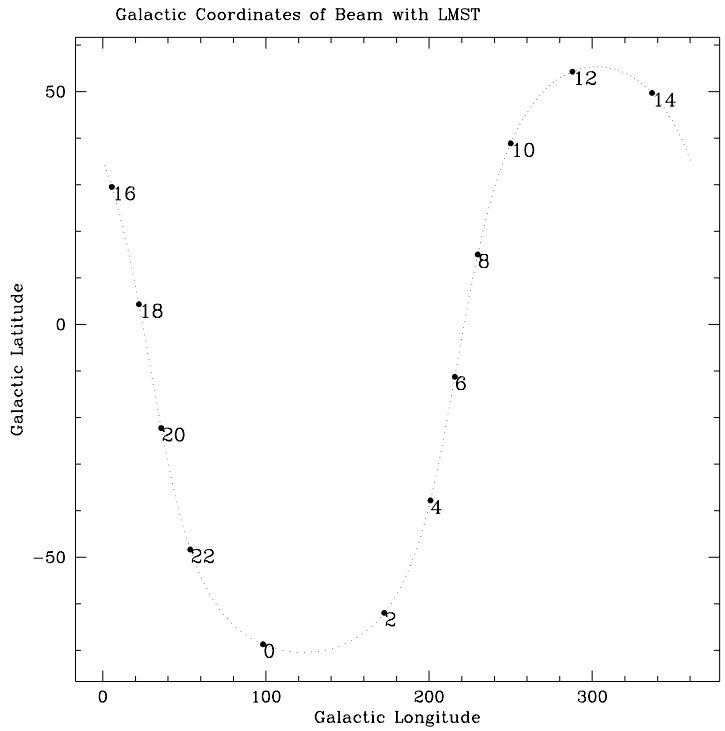

Figure 2-18: The path of the ASEH beam in Galactic Coordinates as a function of sidereal hour.

have not calculated confidence intervals on these fitted values, or the covariances; they are meant to be rough estimates and I expect a different approach to be necessary for higher precision. Note the large $T_{\rm misc}$ at the higher frequencies. I suspect this is due to strong RFI; note the noisiness of the total power trace for board 15 relative to lower–numbered ones in figure 2-19. K does track the gain curves in figure 2-8.

Inspection

For purposes of presentation and inspection, the coadded spectra are grouped into two dimensional images, the axes being frequency (218.774 MHZ to 251.226 MHz) and sidereal time (span 31.75 minutes). An example is presented in figure 2-21. The brightness units are $T_{\rm sys}$ in Kelvin. Note the temperature discontinuities in time for some frequencies. The boundary is a CAL firing, when new calibration is computed. This indicates that my

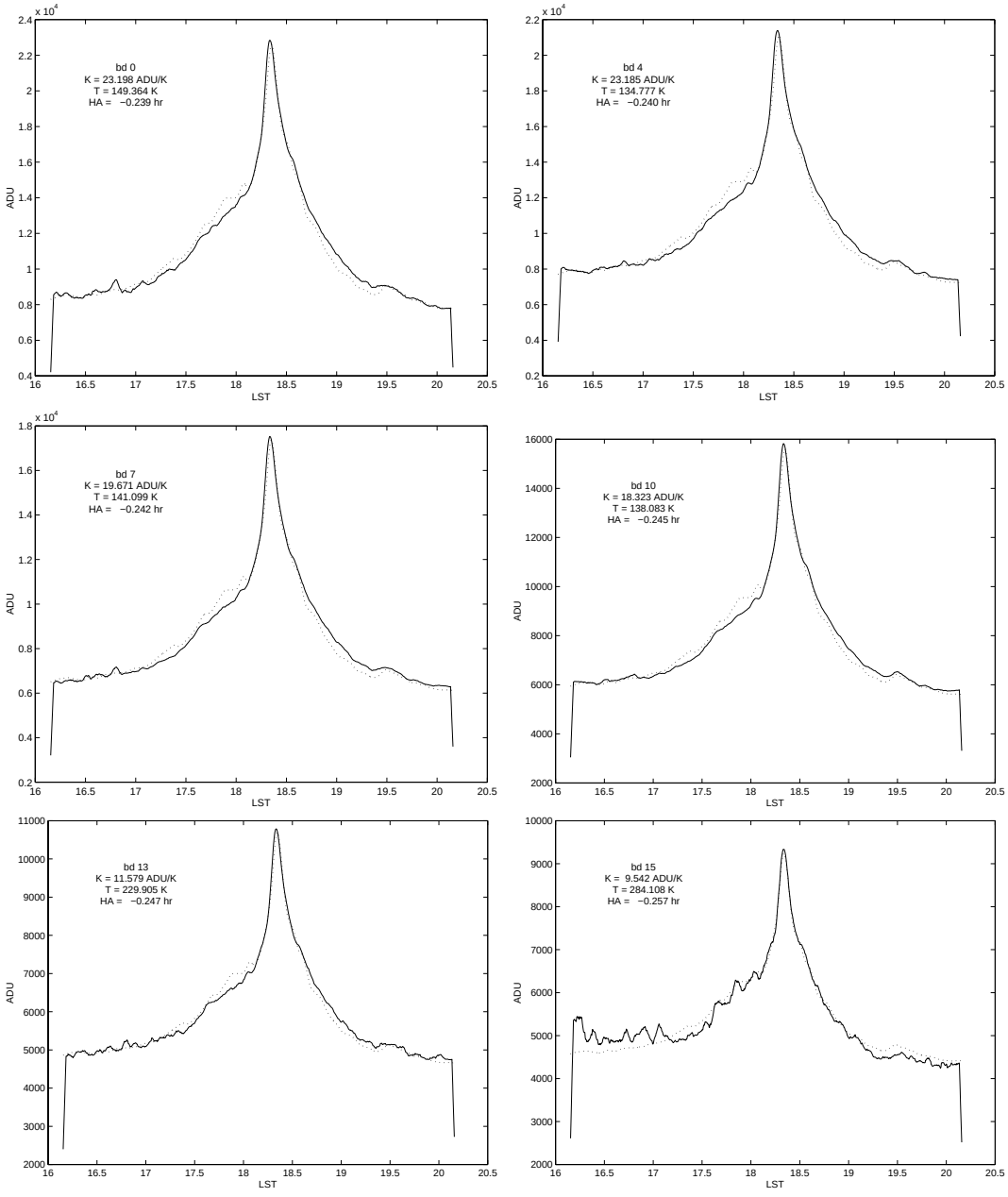

Figure 2-19: A representative sample of results of fitting Milky Way transit to a model response, taking account of sky brightness spectral index and extraneous contributions to system temperature.

SPA board (ν_{center} MHz)	K (ADU/K)	T_{MISC}	Hour Angle (hrs)
0 (220)	23.20	149.4	-0.24
1 (222)	28.25	159.4	-0.24
2 (224)	25.23	193.3	-0.23
3 (226)	25.29	171.0	-0.24
4 (228)	23.19	134.8	-0.24
5 (230)	21.01	141.5	-0.24
6 (232)	20.06	140.6	-0.24
7 (234)	19.67	141.1	-0.24
8 (236)	17.78	141.2	-0.24
9 (238)	19.54	129.6	-0.24
10 (240)	18.32	138.0	-0.25
11 (242)	–	–	–
12 (244)	13.74	148.3	-0.25
13 (246)	11.56	229.9	-0.25
14 (248)	11.56	245.3	-0.25
15 (250)	9.54	284.1	-0.26

Table 2.2: The results of fitting Milky Way transit data for one night in May 1997 to a model response based on expected sky brightness. T_{misc} is the non–sky contribution to system temperature *minus* measured receiver temperature, for example feed spillover, cable loss, *etc.*

method of removing gain variations adds noise of its own.

The question arises whether one can reduce the data without a CAL source, just averaging data. The main difficulty is the gain instability of the system from day to day. As shown in figure 2-20, the broadband gain can vary by ±15% from day to day; it could be even worse seasonally (although the seasons are not pronounced in Puerto Rico). The baseline shifts could also be due to broadband RFI, but without an external CAL its difficult to tell which.

One might self-calibrate. That is, estimate the baseline power as a function of LMST, and look for similar structure in the baseline power traces over all the nights to be coadded, then tie the gains together to an arbitrarily normalized trace. Although the Galaxy profile is reproduced well night to night, there are stretches of sky where the celestial variation is less than the instrumental effects. This is clear again in figure 2-20. The traces do not share any structure. It is not clear how to adjust the gains in this case to improve convergence of the coaddition.

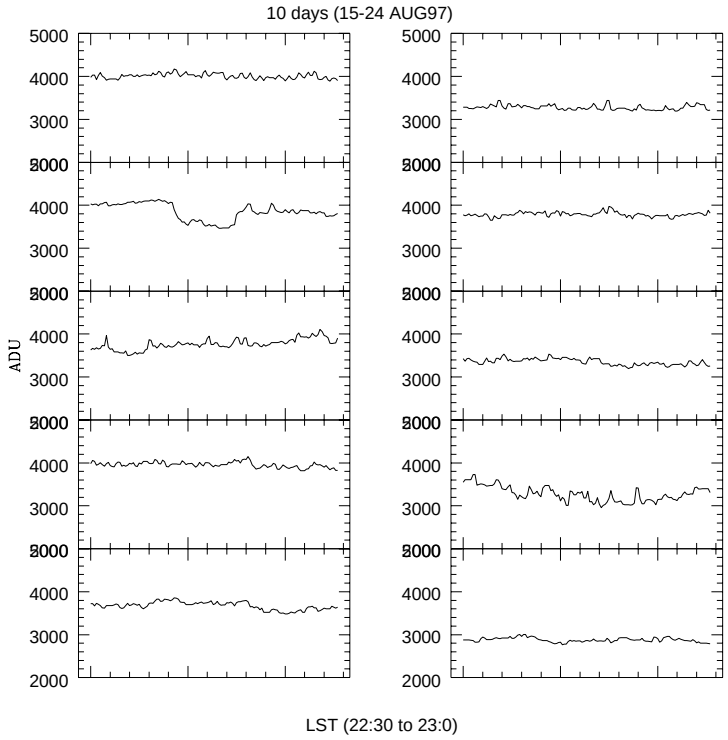

Figure 2-20: Continuum power over the same LMST range on ten consecutive days, away from the Galactic plane. Where are the continuum sources? We expect the sky to vary by about 10K over this LST range. The variations in system power are dominated by non-celestial sources.

Second Reduction

In light of the problems with the CAL and the quality of the final images, I believe even the limited use I make of the CAL signal is not especially worthwhile. So I have also reduced the data (adding the data that arrived by mail since completing the first reduction) without any calibration. The pipeline is almost exactly the same as above, except the CAL integrations are not used and the spectra are left unnormalized. When a tape's worth of days are resampled and ready to be coadded, I compute each coadded frequency bin independently by sorting the set by value, discarding the bottom two and upper 40%, and taking the mean of the remainder. This is only slightly different than the first reduction in which I simply sorted the values for that bin for all the spectra, and then picked the 33% point. The mean

converges faster than the median for Gaussian distributed values, but much slower for some other distributions, in particular ones which more closely resemble our RFI–corrupted data (Weintroub 1998 , Lupton 1993).

An example of an uncalibrated coadded spectral image is figure 2-22, covering the same LMST range as figure 2-21. I generally achieve lower $T_{\rm rms}$ without using the CAL, but the conversion from ADU to K may be less secure. I can convert the brightness scale to Kelvin, roughly, by using the results of the Galaxy transit fits. Figure 2-23 shows the conversion factors I used. In figure 2-22, the high frequencies are brighter than the low frequencies; this is obviously an artifact of the conversion from ADU to Kelvin. The baseline will be subtracted, however, so the net effect is that the rms in Kelvin will be higher in this subband than it should be; or that the rms is too low in the middle of the band. A more precise determination of the conversion of ADU to Kelvin, by a different method than described above, would improve things. I leave this for future work.

Baseline Subtraction

To look for spectral lines it is necessary to subtract baselines both in frequency and time. The frequency baseline has a very complex structure, which is constant in time, and whose amplitude far dominates over the "thermal" noise, as demonstrated in figures 2-24 and 2-25. I do not know what causes this structure; it could be interference from the instrument itself or from other electronics nearby. It is noticeable only after coadding some amount of data. I remove it, along with any trend over time, in the following way: the first spectrum in the image is taken as fiducial. Every other spectrum is fit to it, the allowed differences being, a constant offset (to allow for continuum sources passing through the beam) and a distortion described by a second order polynomial in frequency (to allow for spectral index variations). Figure 2-26 shows the derived baseline deviations for the field starting at 00:00 LMST. The fit is "robust," meaning large discrepancies of the data from the model do not increase the measure being minimized. That way spectral features that are not constant in sidereal time are not included in the fitted baseline and so are left in the base-line subtracted data. A smoothness constraint in time would be physically reasonable and might improve confidence in the final residuals, but I leave that also for the future.

After solutions are found to make each spectrum resemble the first in baseline DC level and curvature, I compute a template spectrum by taking the median (again, a robust measure) of each frequency bin. Then the template is subtracted from all spectra. The resulting spectra are close to zero-mean, flat in frequency and sidereal time. The results of this procedure on the same field in figures 2-22 and 2-21 are presented in figures 2-27 and 2-28. The residuals are definitely not Gaussian-distributed. Figure 2-29 is a histogram of all time-frequency pixels in the example field. There are a large number of bright outliers due to the RFI-corrupted subbands. We expect that. Figure 2-30 is a histogram of the quietest (as ranked by time-wise variance) 128 frequency bins, or about 4% of the whole band. The spike at 0 is probably due to my baseline subtraction technique, perhaps related to the lack of a smoothness constraint in time; on the other hand, broadband RFI can turn on and off faster than the beam, so it's not clear that the lack of such a constraint is invalid. There are clear deviations from Gaussianity, which could be evidence of (a) low-level RFI, perhaps bleeding from the stronger bands (b) real positive excess celestial flux. I don't see how the two effects are separable.

What is the effective noise in the final images, for the purposes of setting upper limits on protocluster fluxes? The RFI corrupted subbands would skew the overall value of $T_{\rm rms}$, so what fraction of the whole band do they occupy? In figure 2-31 I have computed the rms as a function of fractional bandwidth, adding frequency channels from quietest to noisiest as measured in time-wise variance. Note that $T_{\rm rms}$ stays below 2K until one incorporates more than 35% of the band. It rises as a power law until about 70%, when it takes off due to the inclusion of RFI-dominated channels. In the search for protocluster signatures, the RFI bins will be obvious and visually excluded. Therefore I can take the effective noise in the band to be the cumulative $T_{\rm rms}$ at the knee, which is at about the 75%ile. This is not the full story, because the 75% will not be contiguous in frequency and that complicates source detection; but it's a straightforward estimate and not grossly incorrect.

Image Presentation, Candidate Source List

For inspection by the reader, In Figures A-1 through A-98 I present all the fields reduced, in most cases both with and without CAL, but some fields do not have both available. I

have inspected the images for interesting signatures: bright regions about a beamwidth ($\approx$ 3 min) wide and between 0.5 and 2 MHz tall (see 3.1.3). As discussed above, the final images are the result of combining some small number, usually four, of spectral images which are themselves averages of nominal 2 week intervals. So when I see an interesting feature in the final image, I can inspect the independent 2-week images as a check on its reality. The upshot is that I can find no convincing signals. Usually it turns out the feature is not present in one or two of the 2-week sets, even though they all may have about the same noise level. Figure 2-32 is the one possible exception, and not very convincing. It does not appear in all the independent images.

If one knew, or made bold assumptions, about what the signature should be, a more sophisticated analysis might be warranted, such as matched or optimal filtering (Press *et al.* 1992); (Weintroub 1998) or a likelihood analysis. I have attempted to filter the images by means of a template derived from the considerations of section 3.1.3, but the results are not better than the raw images and not worth further mention.

Although the search for obvious, discrete signals has not yielded a result, there are some artifacts in the data worth noting. In many fields, there is low-level structure in the images which does not look like simple noise. In figure 2-32 they are visible. In section 3.1.3 I review the results of theoretical investigations of cosmological HI emission that cause me to pause over these features, although I must say up front I believe they are most likely artifacts produced by my reduction algorithm, probably during baseline estimation and subtraction. It is possible they are associated with real, polarized emission in the Galactic plane. These features are most prominent in fields at low Galactic latitude. Wieringa *et al.* (1993), during a search for protocluster HI emission discovered linearly polarized structures on scales of arcminutes to degrees, and of brightness temperatures 2-4 K.

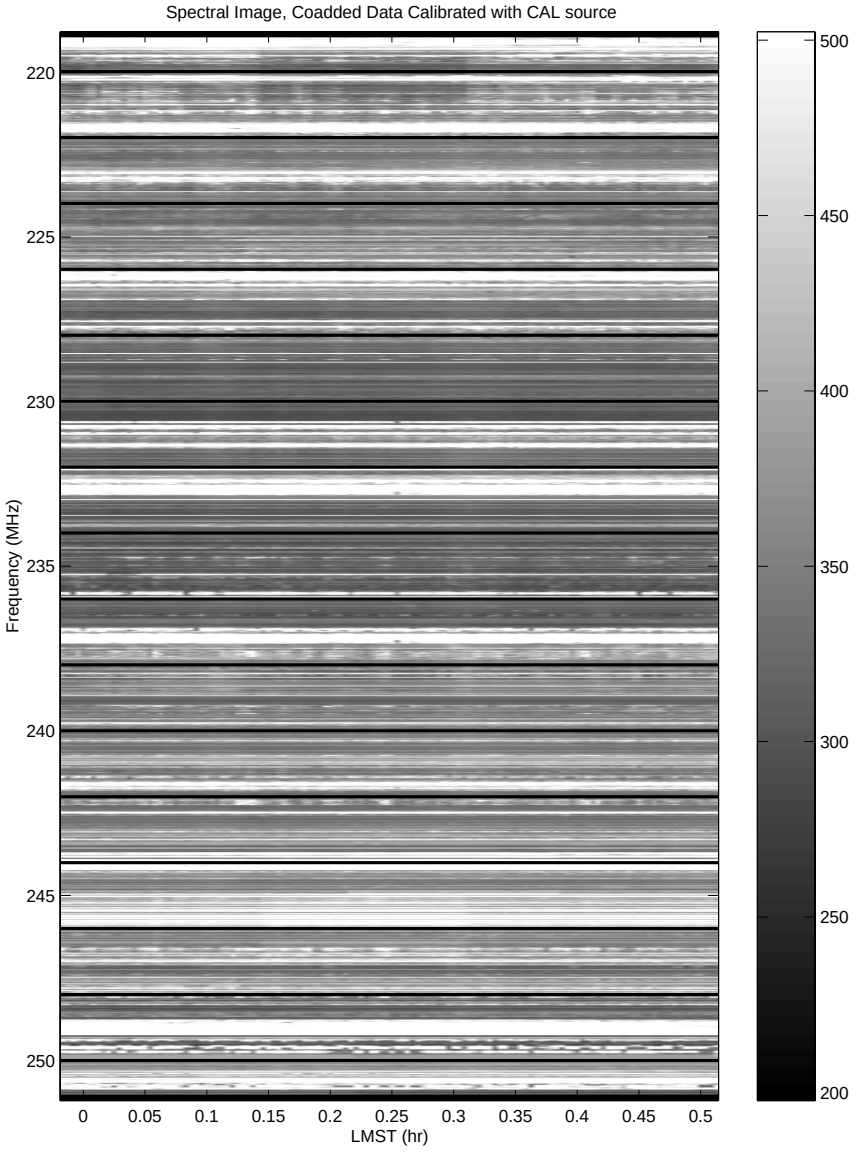

Figure 2-21: A spectral image of coadded data, in the example field around 0.24 hr LMST. These data have been calibrated with the CAL source before coaddition, in the manner described in the text.

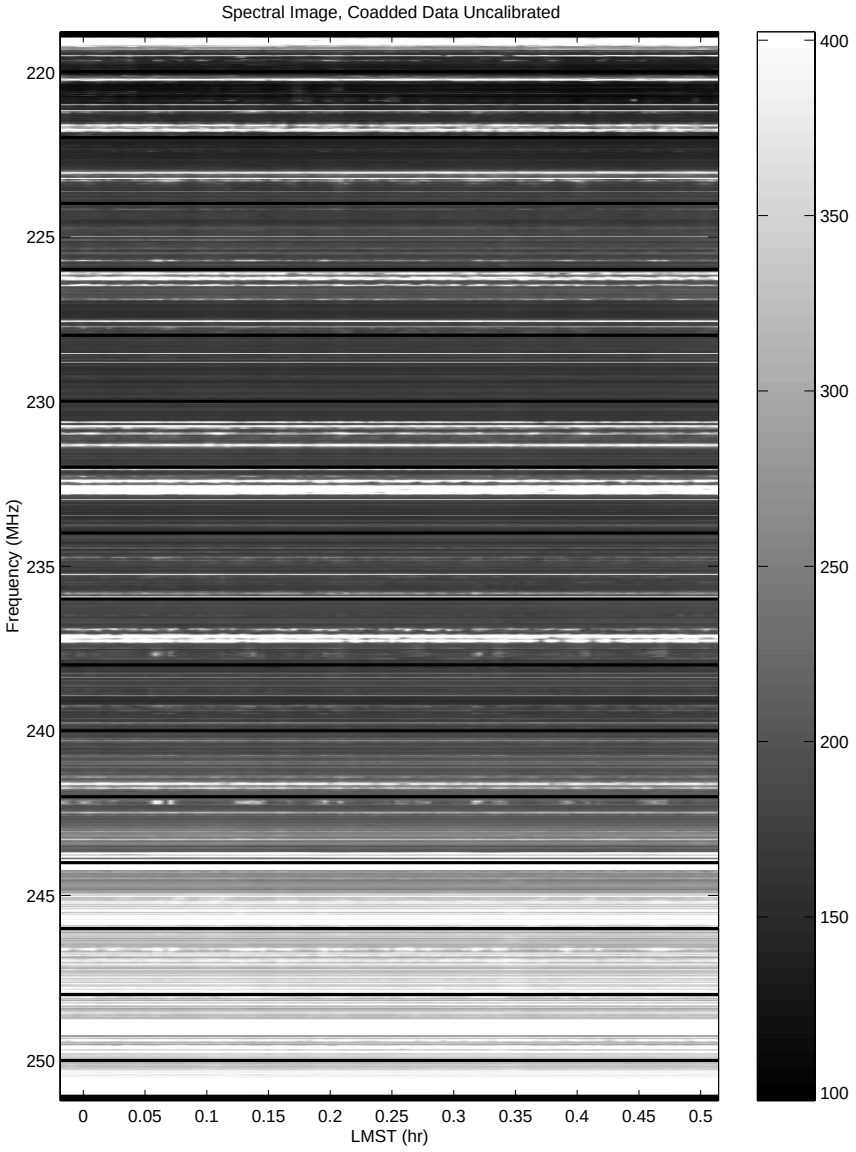

Figure 2-22: A spectral image of the example field around 0.25 hr LMST. This is the result of the second reduction, in which I did not use the CAL source to normalize spectra.

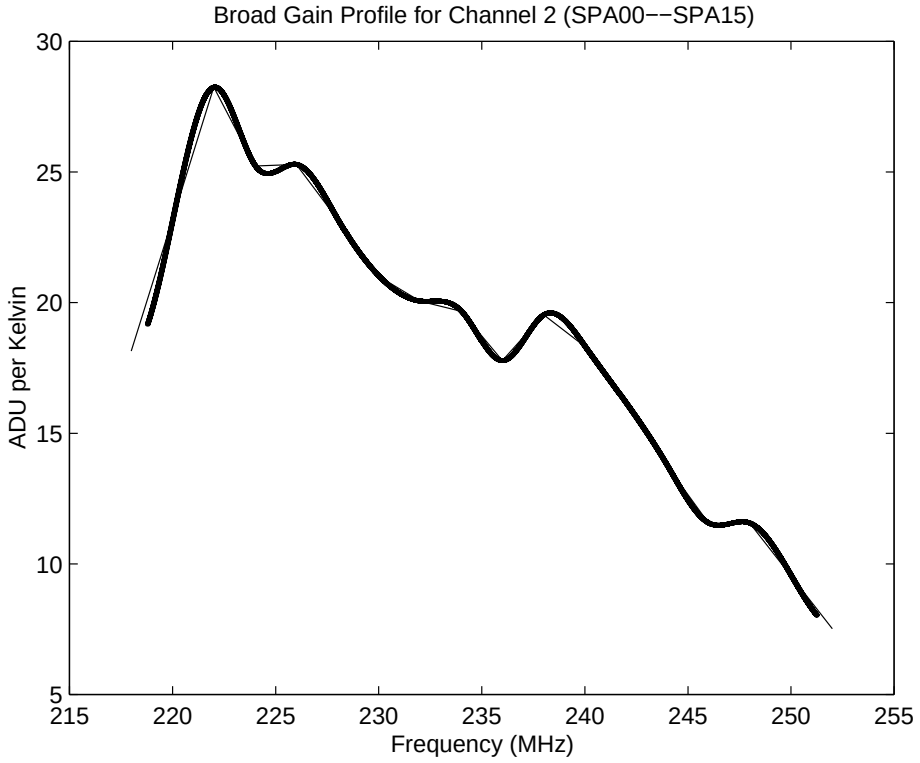

Figure 2-23: Conversion Factors, ADU per Kelvin, derived from Galaxy transit fits to uncalibrated data. The heavy curve is a spline smoothed version of the coarse (2 MHz) solution.

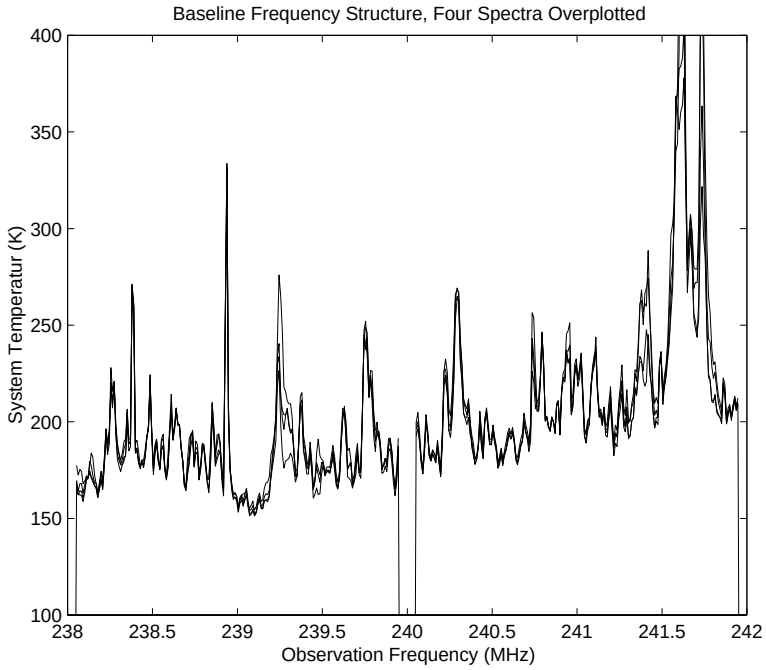

Figure 2-24: A section of the baseline from four spectra, over a span of 30^{m} LMST, overplotted. The baseline is highly structured but quite steady.

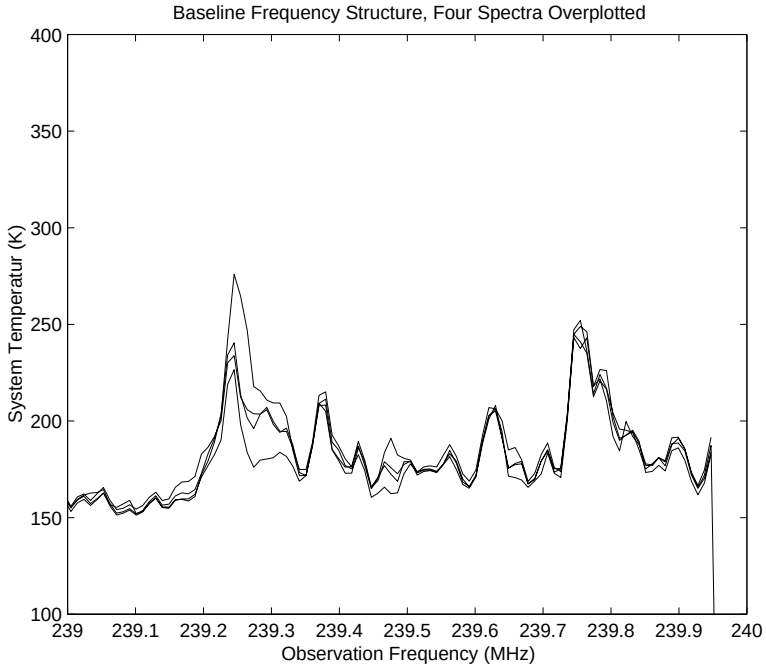

Figure 2-25: Enlarged section of the above frequency span, showing the small deviations around the constant baseline.

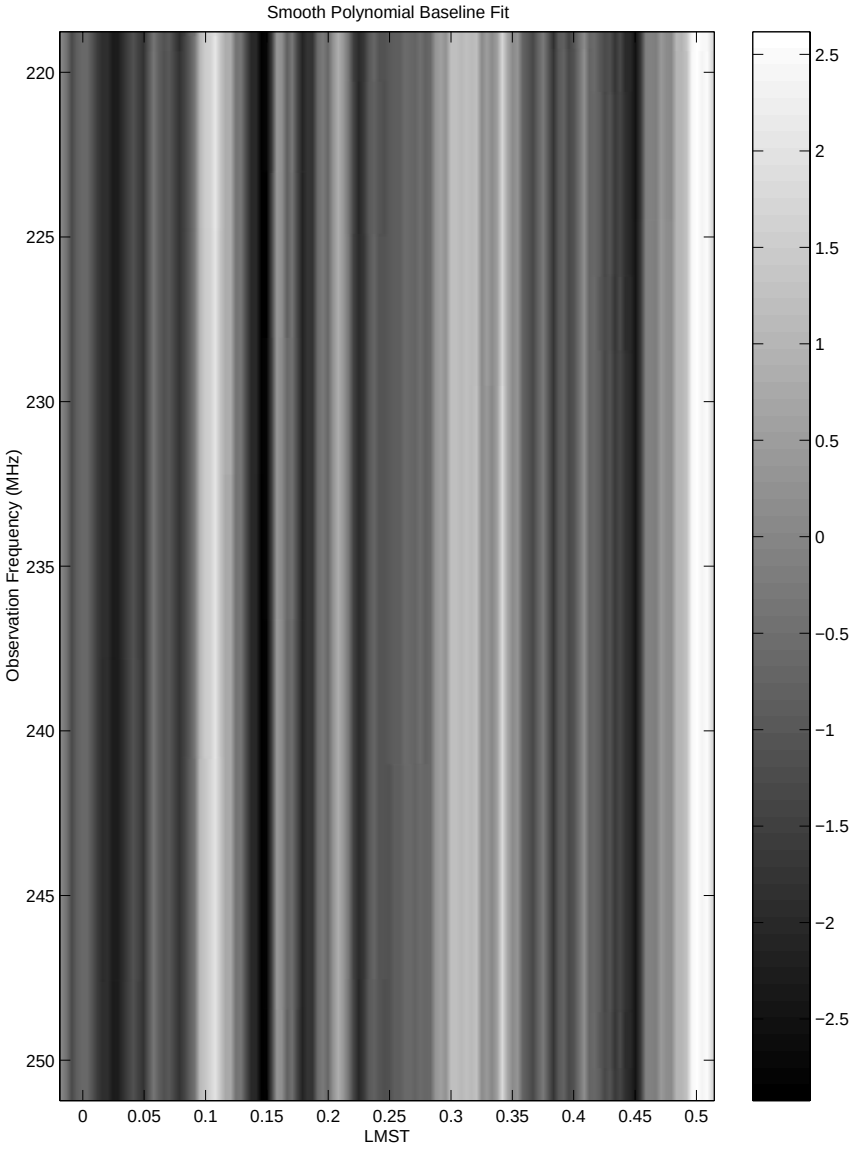

Figure 2-26: An image of the smooth baseline component resulting from the fit of all spectra to the first. The curvature in frequency is small and not visible in this stretch.

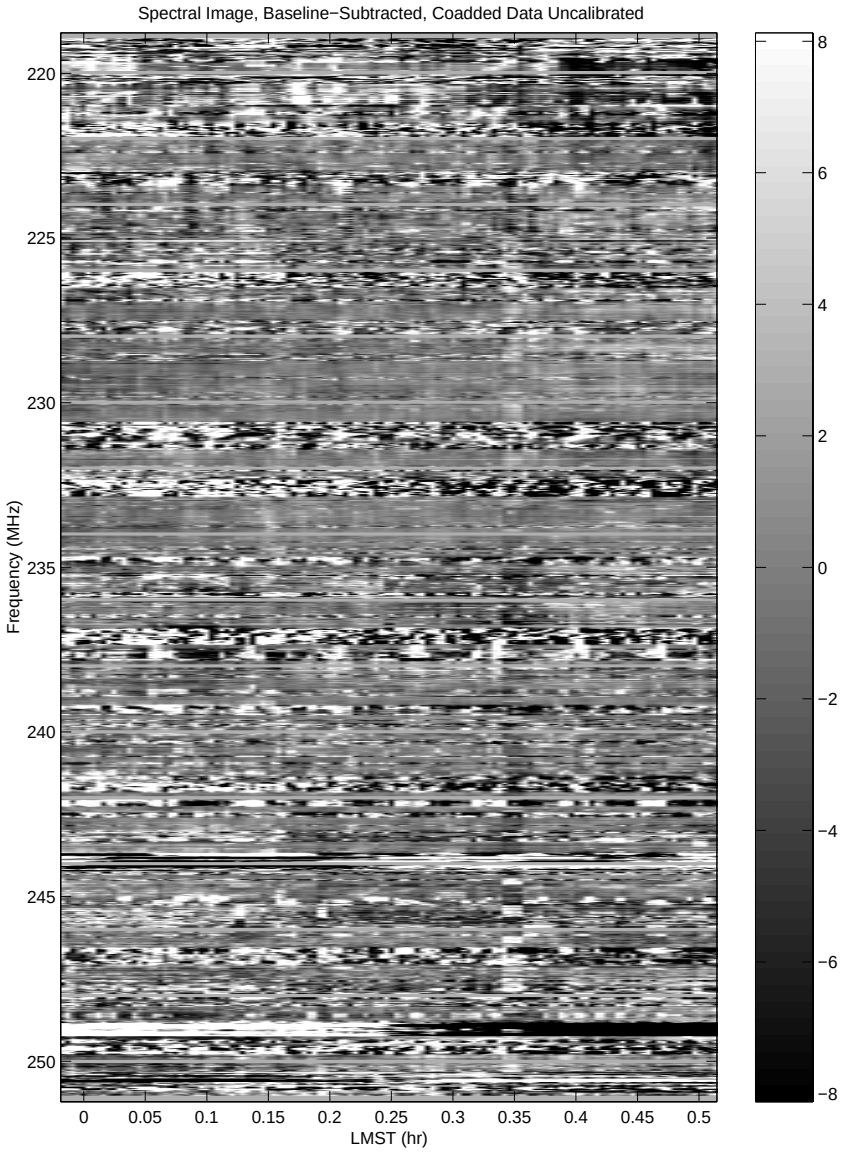

Figure 2-27: A spectral image of the example field around 0.25 hr LMST. Uncalibrated data. Brightness units are Kelvin. This is the baseline-subtracted result corresponding to the image in figure 2-22.

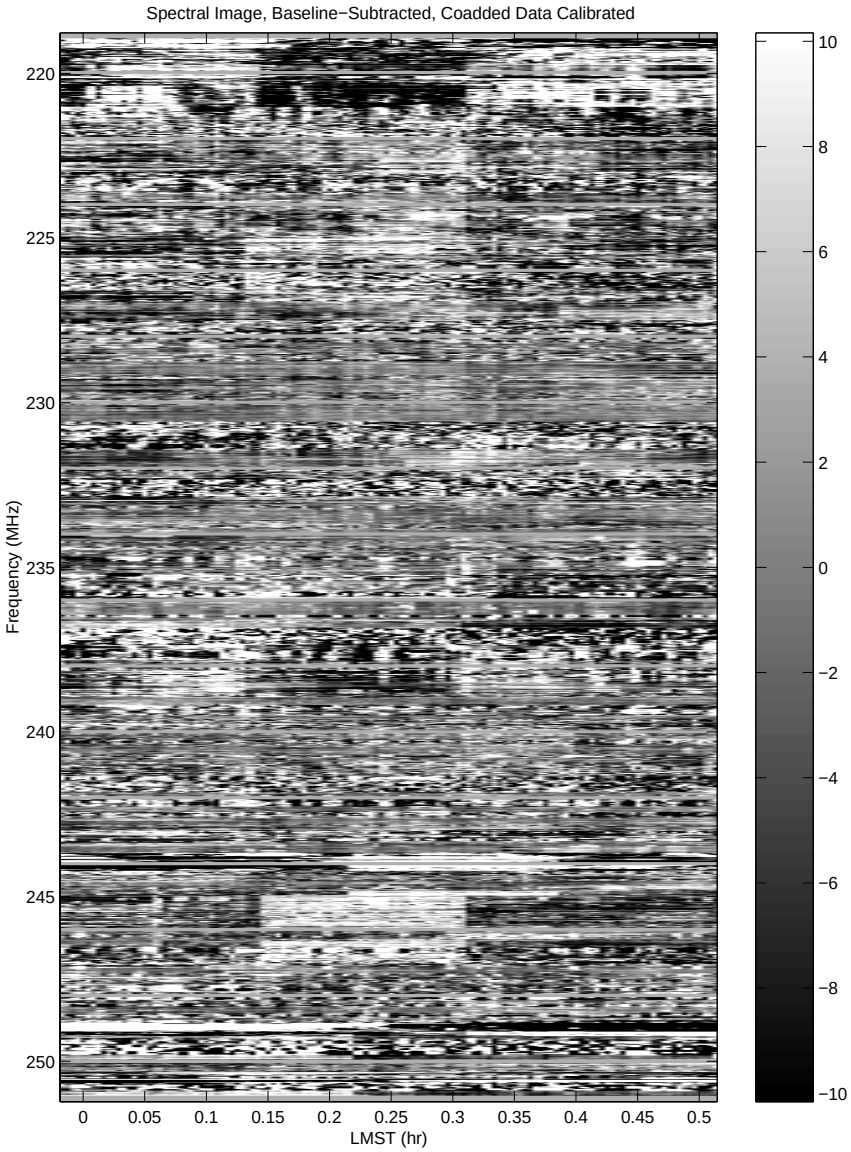

Figure 2-28: A spectral image of the example field around 0.25 hr LMST. Calibrated data. Brightness units are Kelvin. This is the baseline-subtracted result corresponding to the image in figure 2-21.

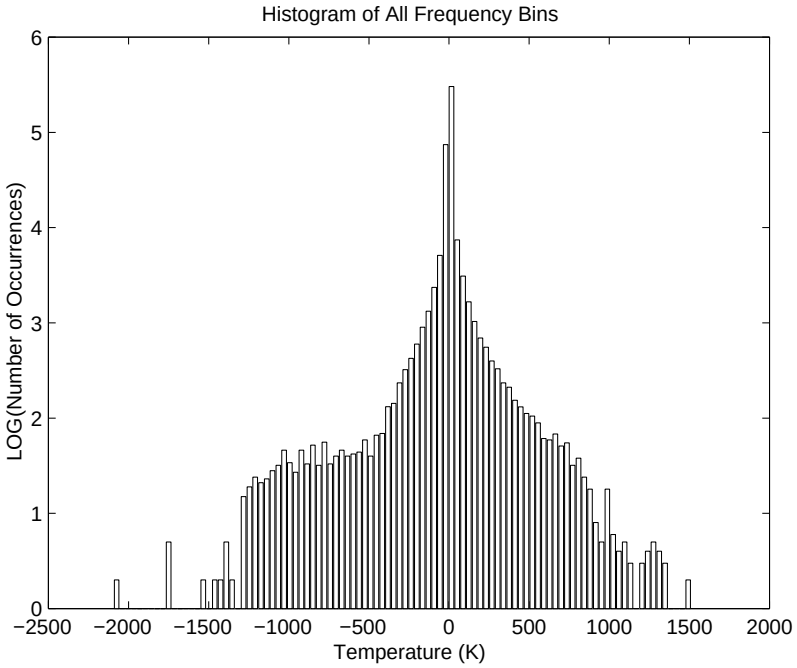

Figure 2-29: A histogram of pixel values in the example field. The are many large-residual outliers, probably due to RFI.

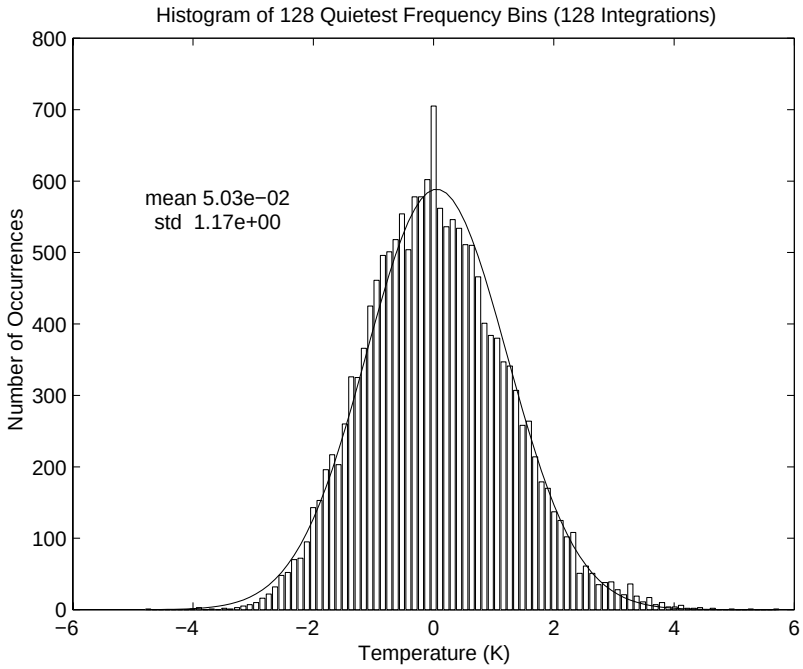

Figure 2-30: A histogram of pixel values in the quietest 128 frequency channels in the example field. Closer to a normal distribution. The excess at 0 is probably an artifact of the reduction procedure.

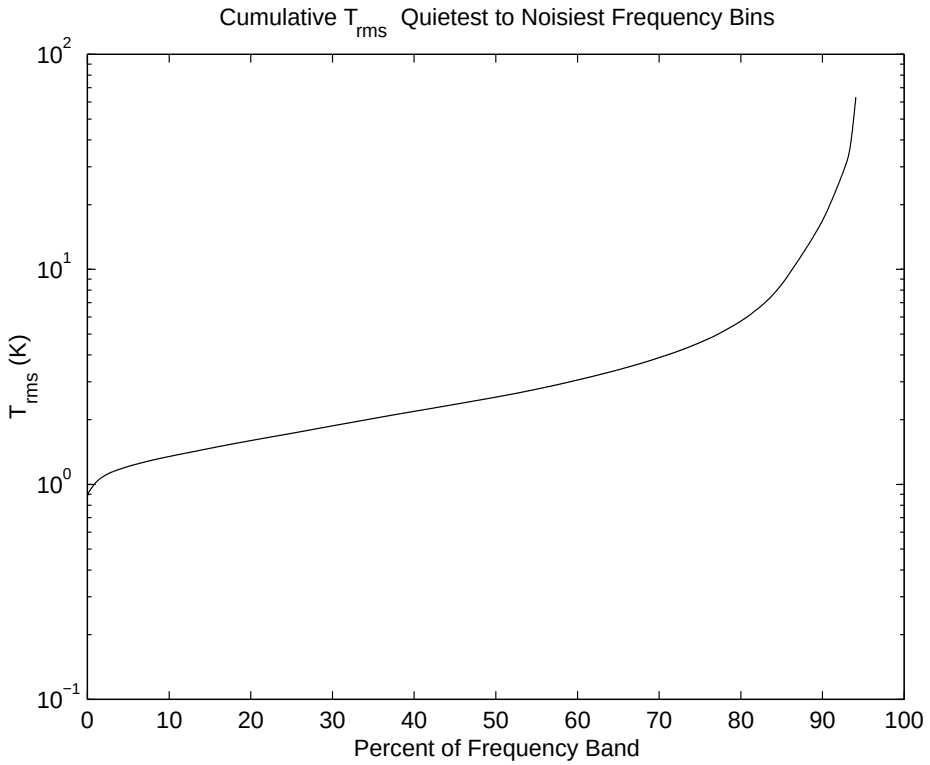

Figure 2-31: The cumulative rms of the baseline subtracted image of the reference field. The frequency bins are ranked by time-wise variance, then the cumulative rms is computed of subimages of increasing size.

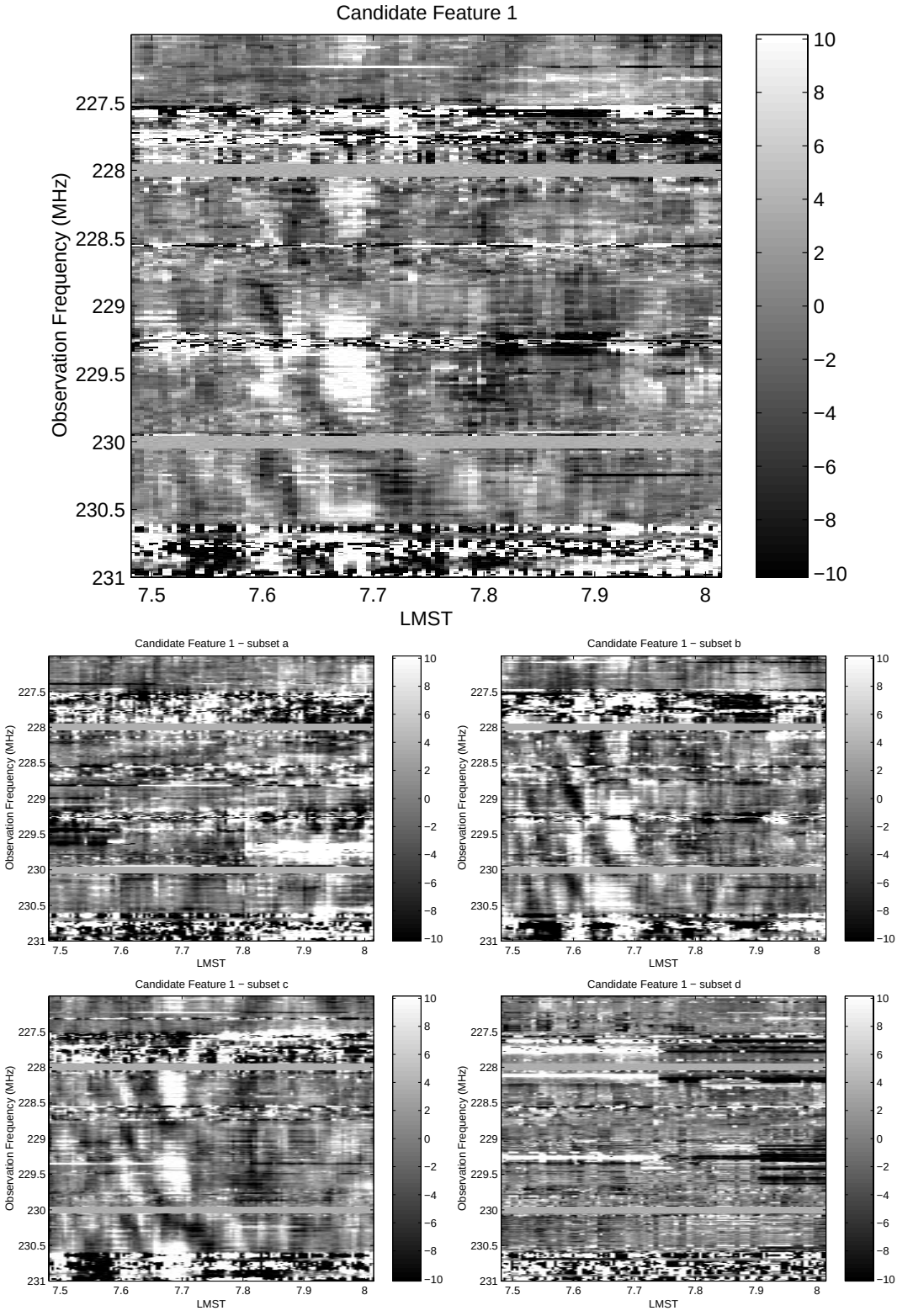

Figure 2-32: A bright polarized spectral feature in a field at low Galactic latitude. The greyscale is in Kelvin, and saturates at about 10K. Note the feature is not present in all independently reduced data subsets. Note also the fainter mottled structure nearby. Discussion in the text.

Chapter 3

ASEH and Structure Formation

In this chapter we provide the background necessary to interpret the results of the Arecibo Search for Early Hydrogen in the context of theories of cosmological structure formation. First we motivate the discussion with a brief exposition the early universe and why it's plausible that any structure at all exists today. Then we delve into some standard models of structure formation and their observational consequences. Finally, we compare the results to date of the ASEH experiment with it's forerunners and interpret them in the context of the models discussed.

3.1 Theoretical Expectations

3.1.1 The Early Universe

It is accepted that all the structures we see today have been formed by the gravitational growth of initially small density perturbations. The origin of inhomogeneity is a matter of speculation. Various kinds of surveys, from galaxy clustering to CMB isotropy, have quantified the degree of matter inhomogeneity at different epochs and volume scales. These observations are used to constrain models of the gravitational growth of structure in an expanding universe.

The standard model of cosmology is the Hot Big Bang, in which the universe is today undergoing decelerating adiabatic expansion from an earlier, hotter, and denser state. The dynamics of expansion are described by the equations of General Relativity. All of

the present components of mass-energy were once greatly compressed and in thermal equilibrium. As the energy density became dilute, and reaction rates fell, species of particles decoupled from equilibrium with photons. Within this context, standard physics can account for the measured abundances of the elements, and the growth of local density peaks through gravitation.

The origin and spectrum of density perturbations are not part of the standard model, but are supplied by auxiliary theories. These may be very generally grouped into two classes, causal and acausal (Albrecht 1998), depending on when the density perturbation power spectrum is fixed, and when it is expressed by the matter. The favored theory, inflation, is an acausal theory. Some time before the start of the standard Hot Big Bang scenario a spontaneous symmetry–breaking phase transition occurs, and while the field value changes to a new potential minimum it provides an effective energy density that causes to universe to expand exponentially, or "inflate." Small quantum mechanical perturbations to the classical value of the field's potential are inflated to large scales and serve as the seeds of structure formation. The theory is called acausal because the power spectrum is frozen on superhorizon scales. It is also possible that inflation occurred but is not the source of the dominant fluctuations; a later phase transition may have given rise to topological defects (domain walls, cosmic strings, *etc.*) which serve as perturbation seeds. The correlation length is limited by the particle horizon, so these theories are termed causal.

Measurements of CMB anisotropy can be tied to density perturbations at the epoch of recombination ($z \approx 1100$) via the Sachs-Wolfe effect (Kolb & Turner 1990). Since the measurement of degree-scale CMB anisotropies by the COBE satellite, defect models have been deemed less attractive than inflation. The power spectrum measured is consistent with the inflationary prediction, $P(k) \propto k^{-1}$. Current models of structure formation generally take this as the starting power spectrum, and the early growth of structure as due to gravitational accretion.

3.1.2 Gravitational Growth of Structures

While density contrasts are low, they grow with time (or redshift) as $(1+z)^{-1}$ (Peebles 1993). The nature of the first bound objects depends on the constituent matter. Inflation predicts

the observable universe has vanishing spatial curvature. If there is no cosmological constant, then the mass density must be at the critical value $3H_0^2/8\pi G$. Further, comparison of astronomical observations with nucleosynthesis calculations based on well–understood physics (Kolb & Turner 1990) indicate that the fraction of critical density in baryons is small, $0.005 < \Omega_b < 0.15$ (Barnett 1996 , Schramm & Turner 1998). The remaining matter is *non–baryonic*, and interacts with baryons only gravitationally. This is one constituent of the "dark matter," the mass that is present but unobservable except through it's gravitational effects. There is also baryonic dark matter, but it is included in the estimate of Ω_b above.

The nature of the dark matter is unknown. But if it interacts gravitationally with other constituents it can be included in calculations of structure formation straightforwardly. The characteristic free parameter is the mass of the individual particles. If the particles are light enough to be relativistic at $z_{\rm eq}$, the epoch of matter–radiation energy density equality (the epoch when matter can begin to cluster gravitationally), they will stream out of regions of high density more efficiently than more massive, slower, particles. Hence density contrasts will be washed out on small scales. This is called "hot" dark matter (HDM).

Historically, HDM models of structure formation were considered first, probably because neutrinos, a prime candidate particle, have observational mass bounds in the appropriate range. In the HDM paradigm the first structures to form are large, cluster–sized masses (Zel'dovich 1970), referred to as "Zel'dovich pancakes." Density perturbations collapse non-axisymmetrically into oblate clouds; when particle orbits cross the gas shocks and dissipates energy, fragmenting into smaller structures. In N-body simulations, HDM is seen to provide too little clustering power (as compared to observations) on small mass scales. The recent COBE measurements of CMB temperature anisotropy on scales of 7°, used to normalize the density perturbation spectrum at large spatial scales, exacerbates HDM's problems.

Cold dark matter (CDM) models, in which the particles are nonrelativistic at equality became the favorite of structure formation theorists in the 1980's (Bertschinger 1993). They do match observations better over a wide range of mass scales, but fail notably at the large end, or rather, it is difficult to avoid overproducing small scale structure when the large scale matches observations. The mismatch between N-body calculations and observations

has provoked interest in variants to the standard CDM, for example tilting the power spectrum, or adding a non-zero Λ. Even with it's limitations CDM remains a touchstone of structure theories, because of it's successes and its well–characterized shortcomings.

In a standard analytic approximation for the non-linear "bottom-up" hierarchical growth of structures, the Press–Schechter formalism (Press & Schechter 1974), the growth of masses by condensation is self-similar, meaning the distribution of masses looks the same even as the characteristic mass scale of collapse increases. At late times the distribution of masses of collapsed objects does not depend on the spectrum of seed masses, the number density at mass scale M and expansion scale a having a functional form

$$n_a(M) \propto M^{-1-\alpha} \exp[-const \times (\frac{M^{1-\alpha}}{a})^2].$$

Within this formalism, the first generation of bound objects occurs at a redshift of about $z_i = 50/b$ (Peebles 1993), where b is the "bias" parameter, or the factor by which the baryon overdensity exceeds the dark matter (~ 2.5). The typical mass of the objects is $\approx 10^5\,\mathrm{M}_\odot$, which will have been able to cool quickly and form stars (or black holes; it is debated what kind of object first forms (Silk & Rees 1998)) that can reheat the intercloud gas.

3.1.3 The Observability of HI at High Redshift

In the standard interpretation of the CMB radiation, the universe became transparent to photons at a redshift of approximately 1100 when the space-filling plasma recombined into neutral gas. The spectra of the most distant quasars, $z \lesssim 5$, reveal absorption features along the line of sight by discrete clouds of hydrogen gas. The most prominent features are due to resonant scattering of Lyman α (Lyα) photons from the quasar's continuum. These Lyman-α clouds range in column densities from roughly 10^{12} to 10^{22} cm^{-2} (Shull 1997). The lower density clouds are warm (T $\approx 10^4$K), highly ionized and of low optical depth. The higher density clouds, termed Damped Lyα (DLA) clouds, are opaque, absorbing all the continuum photons, and have a large neutral mass. The DLA systems may be early galaxies; they have the appropriate H mass, have higher metallicities than the wispier Lyα forest clouds (0.01 *vs.* 0.001 of solar), and are more strongly clustered, as are present day galaxies (Peebles 1993).

Although the clouds appear discrete, that may only be apparent and they are also consistent with fluctuations in a continuous intergalactic medium (IGM) (Bi & Davidsen 1997).

Apart from absorption by seemingly discrete clouds, there doesn't seem to be significant optical depth due to smoothly distributed gas along quasar lines of sight. The Gunn-Peterson test (Gunn & Peterson 1965 , Peterson 1997), the observational non-detection of a continuum decrement in quasar spectra, constrains the number density of hydrogen atoms to be $n(\langle z_{\rm abs}\rangle = 2.64) < 1.8 \times 10^{-11} h^{-1}$ cm^{-3}, a negligible contribution to the overall matter density.

When and how the neutral IGM segregates into these different phases is not known. Possible causes include: the decay of relic particles, collisional ionization in shocks created by collapsing clouds, ionization by xrays or UV light emitted from an early population of black holes or stars. The fact that the Lyα clouds have higher than primordial metallicity means a generation of stars has come and gone by z$\approx$5. The observability of atomic H depends on the unknown sequence of events in structure formation, not only the gravitational growth of objects but also the local injection of energy when nongravitational sources of radiation turn on.

In order for HI to be visible in either emission or absorption the spin temperature must depart from the background temperature, which is that of the CMB. The spin temperature will be a weighted mean of the CMB temperature and the gas kinetic temperature, the mix depending on the collision rate and ionization fraction (Field 1959). Scott and Rees (1990) have calculated the evolution of spin temperature for the cosmological IGM prior to reheating and find it follows the CMB temperature fairly closely for redshifts higher than 100 and lower than 10, dropping below in the intermediate redshift range. This is without heat input, however. Although the details of heating are unknown, they do consider it likely that the neutral gas is warm at the redshift of interest ($z > 5$) and so will be observed in emission.

In a very detailed examination of the possible ionization histories of the IGM through the epoch of galaxy formation, Madau, Meiksin, and Rees (1997) conclude that it is probable there was a substantive neutral IGM during the process of first structure formation, existing between HII regions ionized by the effects of collapsing galactic halos. At first the IGM may

be visible in absorption against the CMB, the gas being cooler than the CMB prior to reheating. Once ionizing sources turn on however, very quickly ($\approx 15\%$ of the Hubble time) the IGM is much warmer than the CMB, so that it becomes visible in emission. Of course this neutral phase must become ionized by $z \approx 5$ to be consistent with the Gunn-Peterson results.

Another view, taking a cue from the DLA systems, is that we might observe HI in the collapsed galactic-scale clouds which make up an as-yet uncollapsed protocluster, the IGM being ionized by this time (Subramanian & Padmanabhan 1993). The galactic gas is expected to become collisionally ionized upon collapse. This aids further collapse (of the baryons), because the gas cools efficiently through recombination lines. H_2 molecular lines are also a significant source of cooling (Tegmark *et al.* 1997). In this scenario, it is plausible that 10^{-3} of all baryons have formed luminous objects by $Z = 30$, sufficient to reionize the IGM.

Observational Signature of High Redshift HI

Here the uncertainties in the distribution of HI are manifest. Hogan and Rees (1979) examined the question in the context of hierarchical collapse. They imagine a beam-differencing experiment (similar to how the reduced data are presented in the appendix A of this thesis). If the observation bandwidth is picked to match the expected velocity scale ($\Delta\nu/\nu \sim 10^{-3}$), and the beamwidth is matched to the HI cloud correlation length ($\sim 1'$), then they find one could see typical temperature differences of

$$\begin{aligned} \delta T &= 2.5\,K\,\theta^{-1}\Omega^3 h^2 \Omega_{\rm HI} \left(\frac{\lambda_{c0}}{5\,{\rm Mpc}}\right) \times \frac{(1+\Omega z)^{-1/2-1/3\alpha}(1+z)}{\left[(1+\Omega z)^{1/2}+\Omega-1\right]\left[(1+\Omega z)^{1/2}-1\right]} \\ &\approx 0.72\,K\,h^2\Omega_{\rm HI} \end{aligned}$$

where λ_{c0} is the cluster correlation length today ($\sim 7h^{-1}$ Mpc), α is the mass perturbation power-law index, and I've taken $\Omega = 1$, $z = 5.1$. The authors go on to say that depending on the details of the clumping, a signal appearing as "spikes" in frequency up to a few Kelvin bright might be seen.

Scott and Rees (1990) followed the ionization history of the IGM, as discussed above, and further noted that if there were a phase of unheated HI gas, it would absorb against the CMB, and a beam differencing experiment would see fluctuations larger than in emission by the factor $T_{\rm CMB}/T_{\rm S}$, $T_{\rm S}$ being the spin temperature of the gas.

Madau, Meiksin, and Rees (1997) went further and examined in detail the effects of different heating mechanisms on the IGM, as previously discussed. Once again, because the signals are much fainter than the foregrounds (the extragalactic synchrotron background has a brightness $T_b(z=0) \approx 6\,K\,\left(\frac{\lambda}{1\,\rm m}\right)^{2.8}$, smooth in frequency but not angle) a differencing experiment with good spectral resolution is recommended. They derive a similar value for the characteristic brightness temperature difference,

$$\delta T \approx (0.011\,K) h_{50}^{-1} \left(\frac{\Omega_{\rm IGM} h_{50}^2}{0.05}\right) \left(\frac{1+z}{9}\right)^{1/2} \eta, \tag{3.1}$$

where $\eta \equiv x_{\rm HI}\left(\frac{T_S - T_{\rm CMB}}{T_S}\right)$, and $x_{\rm HI}$ is the neutral fraction of hydrogen in the region for which $T_S \neq T_{\rm CMB}$. In their picture quasars ionize surrounding gas, but also warm more extended neutral gas. A quasar turning on at $z=6$ will by $z=5.5$ ionize a shell of radius 7.5 Mpc, and warm the HI out to 23 Mpc, corresponding to an angular extent $\approx 4^\circ$. The shell of warm HI will produce a ring-like signature in angle and frequency, of peak flux

$$\delta S \approx (6\ {\rm mJy}) h_{50}^{-1} \left(\frac{\Omega_{\rm IGM} h_{50}^2}{0.05}\right) \left(\frac{1+z}{9}\right)^{-3/2} \left(\frac{\Delta\eta}{2.2}\right) \tag{3.2}$$

The width in frequency due to the Hubble flow over the size of the shell, which for the large shell at $z=5.5$ is up 30 Mhz. At higher z and for smaller shells $\Delta\nu$ would be less.

The case of galactic or subgalactic neutral clouds in an ionized environment has been investigated (Subramanian & Padmanabhan 1993 , Kumar *et al.* 1995 , Bagla *et al.* 1997) with an eye toward application of the Giant Meter Wave Radio Telescope (GMRT) in India (Swarup 1996). A representative result is that at a redshift of 5, they find the comoving number density of protoclusters with received flux greater than 0.46 mJy (a 1σ signal) is about $3.8 \times 10^{-10}\,{\rm Mpc}^{-3}$. Such an object could only be detected as excess variance above the system contribution. One would have to have confidence in the noise performance of the receivers. They do find a more detectable signal at lower redshifts, as the clusters

move closer and larger mass scales collapse. HDM pancakes are also investigated, but as mentioned above the COBE normalization of the power spectrum make HDM difficult to reconcile with observations; Zel'dovich pancakes are rarer at high redshift than the above estimates, and although not quite as faint individually (0.44 mJy) they still could only be detected as excess variance in the system.

The spectral footprint of a collapsing protocluster was computed analytically and compared with the results of N-body simulations. The overall width comes from the velocity structure of the protocluster, which at early times derives from the Hubble flow, but eventually stops expanding and contracts. For a spherically symmetric collapse, frequency widths of about 0.5 MHz to 2.0 MHz arise, depending on initial density contrast. The detailed shape of the line is very uncertain, depending on the internal velocity structure of the neutral clouds which are randomly distributed in the protocluster volume. Kumar *et al.* (1995) took them to be Gaussian, and achieved smooth, somewhat Gaussian-shaped protocluster peaks. Bagla *et al.* (1997) performed synthetic observations on N-body simulations; the overall line widths were comparable but had very complicated substructure. It seems likely, given the discovery of star-forming galaxies at redshifts up 5.64 (see section 3.2.2), that the IGM will be ionized over the range of redshifts we probe in this experiment (4.6 – 5.5).

3.2 Observations of Primeval Galaxies

3.2.1 Previous HI searches

Sunyaev and Zel'dovich (1972, 1975) first suggested looking for redshifted 21 cm emission from collapsing protoclusters. A series of searches, summarized in table 3.1, have not yielded any positive detections.

Davies, Pedlar, and Mirabel (1978) used the MkIA Telescope at Jodrell bank in a search for HI emission at 328 MHz and 240 MHz, the former being a protected band for the deuterium hyperfine line (as an aside, it's ironic that RFI was less of a problem for them in the 240 MHz band). They beam-switched, at high Galactic latitude, with a throw of 2° (Their beamsize was similar to ours, about 50′). Flux limits of 50 mJy to 100 mJy were

reached; the authors interpreted their results for Zel'dovich pancakes and decided the mass of any cloud in an observed field must be less than $3 \times 10^{15}\,\mathrm{M}_{\odot}$, or that the number of such in their survey volume must be $\leq 10^6$.

Bebbington (Bebbington 1986) used the Cambridge 6C interferometer to survey at 151 MHz ($z = 8.4$). Rather than using a spectrometer and beam differencing, he observed in a narrow band (1 MHz) and employed frequency switching to remove the contributions from continuum emission. This means only a shell of gas in a protocluster cloud will contribute to the received signal. The final images achieved an rms flux of $10\,\mathrm{mJybeam}^{-1}$ ($T_b = 2.5\,K$) and no sources were detected.

Hardy and Noreau (1987,1988) used the VLA in D array at 327 MHz. They targeted fields with QSOs, hoping that if they are associated with galaxy formation it would improve the odds of detecting HI emission or absorption. They observed with bandwidths of 6.25 MHz and 12.5 MHz, and resolution $\sim$ 200kHz. They were plagued by interference, achieving a flux limit of about $20\,\mathrm{mJy\ beam}^{-1}$ across the band, about four times the expected noise. Again, no sources were found more massive than a few$\times 10^{15}$ $\mathrm{M}_{\odot}$.

Wieringa, de Bruyn, and Katgert (1992) also searched at 327 MHz ($z = 3.3$), with the Westerbork interferometer. Survey parameters were similar to Hardy and Noreau but suffered less from interference and achieved better sensitivity. bandwidths of 2.5 MHz and 5 MHz were employed with resolution of $\sim$200 kHz. Reflecting the theoretical uncertainties, of the six fields observed, only one was chosen that has a quasar. They note that although quasars might be related to structure formation, whether it will increase one's chances of seeing HI or decrease them (due to ionization) is an open question. They achieved very good flux limits of order $4\,\mathrm{mJy\ beam}-1$, and placed upper limits of as low as $10^{13}\,\mathrm{M}_{\odot}$in their best field.

Uson, Bagri and Cornwell (1991) observed with the VLA at 333 MHz and 323 MHz, $\delta\nu =$ 98 kHz. The field chosen centered on a "normal" galaxy at $z = 3.395$. They discovered both absorption and emission, the latter at a high significance ($\sim 4\sigma$) and inferred a neutral mass of $\sim (1.3 - 0.4) \times 10^{14} h^{-2}\,\mathrm{M}_{\odot}$. However, Briggs, Sorar and Taramopoulos (1993) reobserved the field at Arecibo and failed to detect the emission at an even higher level of significance ($> 10\sigma$). They do confirm the absorption feature.

Telescope	ν MHz	z	σ mJy	Volume $10^6 h^{-3}\,\mathrm{Mpc}^3$	Reference
MkIA	328	3.33	50	0.36	(Davies *et al.* 1978)
	240	4.92	15	0.97	
6C	151	8.40	5	12.	(Bebbington 1986)
VLA	332	3.28	15	0.59	(Hardy & Noreau 1987)
VLA	331	3.29	12	1.7	(Noreau & Hardy 1988)
VLA	333	3.26	5	0.22	(Subrahmanyan & Swarup 1990)
VLA	333	3.26	1.3		(Uson *et al.* 1991)
Westerbork	326	3.36	1.1	1.47	(Wieringa *et al.* 1992)
Arecibo	235	5.04	1000.	112.	this work

Table 3.1: Synopsis of previous and current high redshift HI searches, adapted from Wieringa *et al.* (1992).

3.2.2 The Lyman–break Galaxies

The search for primeval galaxies is a field undergoing rapid growth. Whereas the searches at meter wavelengths are nominally for clouds of unionized gas, imagined to be prior to significant star formation, some observers came from the other direction, looking for an expected very strong Lyα emission line from star forming galaxies at high redshift (Djorgovski 1992), again, to no great success. The techniques used for this approach to the problem are improving. By using very narrow Fabry-Perot filters centered at the expected Lyα frequency and employing other colors to reject foreground objects, Thommes *et al.*(1998) have produced a candidate list of primeval galaxies at z=5.7 (no spectroscopic confirmation as yet). The most distant object known to date, a star-forming galaxy at redshift 5.6 (Hu 1998), was discovered in such a Lyα search.

Very lately, an optical technique has been developed which has found a slew of high redshift galaxies. The method that has proven so successful was discovered by Steidel and Hamilton (1992, 1993) . It turns out that the optical depth to Lyα from high redshifts is very large, the photons being absorbed in the host galaxies and IGM. But there is a discontinuity in the UV-continuum of star forming galaxies at the rest-frame Lyman limit frequency of 912Å. The drop is due to the intrinsic spectra of O and B type stars in the primeval galaxy,

and absorption by the intra- and intergalactic neutral media (Pettini *et al.* 1997). Using three filters, two of which bracket the Lyman limit at z=3, high redshift objects can be culled from the field by using color-color diagrams. The selection is automated, which is a necessary condition for reducing images with thousands of galaxies. What appears to be a cluster of such galaxies has been discovered at $z = 3.09$ (Steidel *et al.* 1998), the observed number being consistent with CDM formation scenarios and reasonable bias parameter values (Adelberger *et al.* 1998).

As noted by Thommes, the Ly-break objects are not primeval; they are already enriched with metals. The strong Lyα emitting galaxies are considered better candidates for objects just collapsing from the primeval density field. This is an exciting time for observations of galaxy formation, and although the approaches from above (meter wavelength HI) and below (Lyα emission) have not definitely found the epoch of first structure formation, new instruments coming on line may well do so.

3.3 Results of the Arecibo Search for Early Hydrogen

3.3.1 Limits on Protocluster HI Masses

There are no signals in the images produced from this data set that are convincing. In figure 2-32 I presented the best candidate; even though I consider it very unlikely because elsewhere in the band there's suspicious structure at the same LMST which leads me to believe the baseline fitting algorithm is having trouble. On the other hand, this field is in the Galactic plane, and this source is at about $\ell \sim 220°$, $b \sim 10°$.

The "spectral line" is just about a beamwidth in angular size, and 1 MHz wide. It has a ragged shape, probably due to poor fitting to the baseline frequency structure. Smoothed, it peaks at about 12K. If our sensitivity is 3.8 K/Jy (refer to chapter 4), the peak flux is 3.2 Jy, three orders of magnitude brighter than the estimated signal of interest.

It's interesting that the fields at low Galactic latitude have more structure than at high latitudes. I am not convinced though, that this represents real emission, such as recombination lines. I would like to reduce more data in a different way and see if the features persist.

We can determine what limit our high system noise places on cosmological HI . We will treat each $30^{\rm m}$ field separately; we can further subdivide the frequency band into quarters to segregate the RFI, which is worst at the outer ends of the band. Each field represents a comoving volume of (Padmanabhan 1996)

$$\begin{aligned} V &= \Omega_{\rm field} \int_{z_1}^{z_2} \frac{4c^3}{H_0^3} \frac{\left[z+1-\sqrt{1+z}\right]^2}{(1+z)^3\sqrt{1+z}} dz \\ &= 4.0 \times 10^6 \; h^{-3} \; {\rm Mpc}^3 \end{aligned}$$

(in this and all the following I assume $\Omega = 1$, $\Lambda = 0$) where z_1 and z_2 are the redshifts of the 21 cm line if it appeared at the edges of the observing band, and $\Omega_{\rm field}$ is the angular size of the field, $30^{\rm m} \times 0.77^\circ = 1.87 \times 10^{-3}$ ster. Our whole band covers the redshift range 4.65 to 5.49.

The measured $T_{\rm rms}$ in each field can be related to an rms flux density, $S_{\nu,{\rm rms}}$ by means of the estimated sensitivity (see chapter 4), $S_{\nu,{\rm rms}} = T_{\rm rms}/\Gamma$. Then, assuming an optically thin HI cloud, we can derive a limiting mass of HI (Wieringa *et al.* 1992)

$$\left(\frac{M_{\rm HI}}{10^{14}\,{\rm M}_\odot}\right) = \frac{S_{\nu,{\rm rms}}}{11.7\,{\rm mJy}} h^{-2} \left(\frac{\Delta V}{10^3\,{\rm km/s}}\right) \frac{1+z-\sqrt{1+z}}{(1+z)}$$

where ΔV is the velocity width of the cloud. I will take the velocity width as that due to a spherical collapsing cloud at redshift 5.1, whose density contrast is a $1\sigma_{\rm CDM}$ fluctuation (Kumar *et al.* 1995), about 2000 km/s.

In the calculations I split the observing band into quarters and compute the upper bound on $M_{\rm HI}$ for each subband. $T_{\rm rms}$ is computed optimistically; I rank each individual channel on time-wise variance and then only include the quietest three-quarters of the subband. This is not completely dishonest because the RFI-corrupted channels are relatively easy to distinguish from quiet neighbors, and so the eye is not fooled when looking for spectral features in quiet regions that happen to cross over interloping RFI-filled bins.

In figures 3-1, 3-2, and 3-3 I present the upper limit on $M_{\rm HI}$ derived for each subband and field. Of course, because the flux limits are so high (a half to a few Janskys), the

corresponding upper limits on HI mass are high.

These mass scales do not really probe the expected protoclusters. A simple estimate of the comoving number density of collapsed objects is given in Weinberg *et al.*(1996) . The present day cumulative mass function of clusters with total mass $> M$ is

$$n(>M) = n_0^*(M/M_0^*)^{-1}\exp\left(-M/M_0^*\right) \tag{3.3}$$

where $M_0^* = 1.8\times10^{14}h^{-1}\,\mathrm{M}_\odot$and $n_0^* = 4\times10^5h^3\,\mathrm{Mpc}^{-3}$ (Bahcall & Cen 1993). In a hierarchical model of structure formation the mass fluctuations as a function of redshift and mass scale can be written as

$$\sigma(M,z) = \sigma^*(M/M_0^*)^{-1/3}(1+z)^{-1} \tag{3.4}$$

taking $\Omega = 1$ and the power spectrum index $n = -1$. $n(>M,z)$ can be derived from $n(>M,z=0)$ by asserting $n_z^*M_z^* = n_0^*M_0^*$, that objects of mass $M > M^*$ maintain a constant fraction of the total mass in the universe, which is the case in self-similar growth. Instead of the total mass we can express n in terms of the HI mass, and to be straightforward I will take $\Omega_b = 0.1$, and the ionization fraction to be 0.5, so $M_{\rm HI} = \chi M$ with $\chi = 0.05$. Then

$$n(>M_{\rm HI},z) = n_0^*\left(\frac{M_{\rm HI}}{\chi M_0^*}\right)^{-1}\exp\left(-\frac{M_{\rm HI}(1+z)^3}{\chi M_0^*}\right) \tag{3.5}$$

The argument of the exponent, for our redshifts and mass limits, is $\frac{M_{\rm HI}(1+z)^3}{\chi M_0^*} \approx 2\times10^5$, so even in our entire search volume of $106\times10^6h^{-3}\,\mathrm{Mpc}^3$, much larger than previous searches, the expected number is infinitesimal.

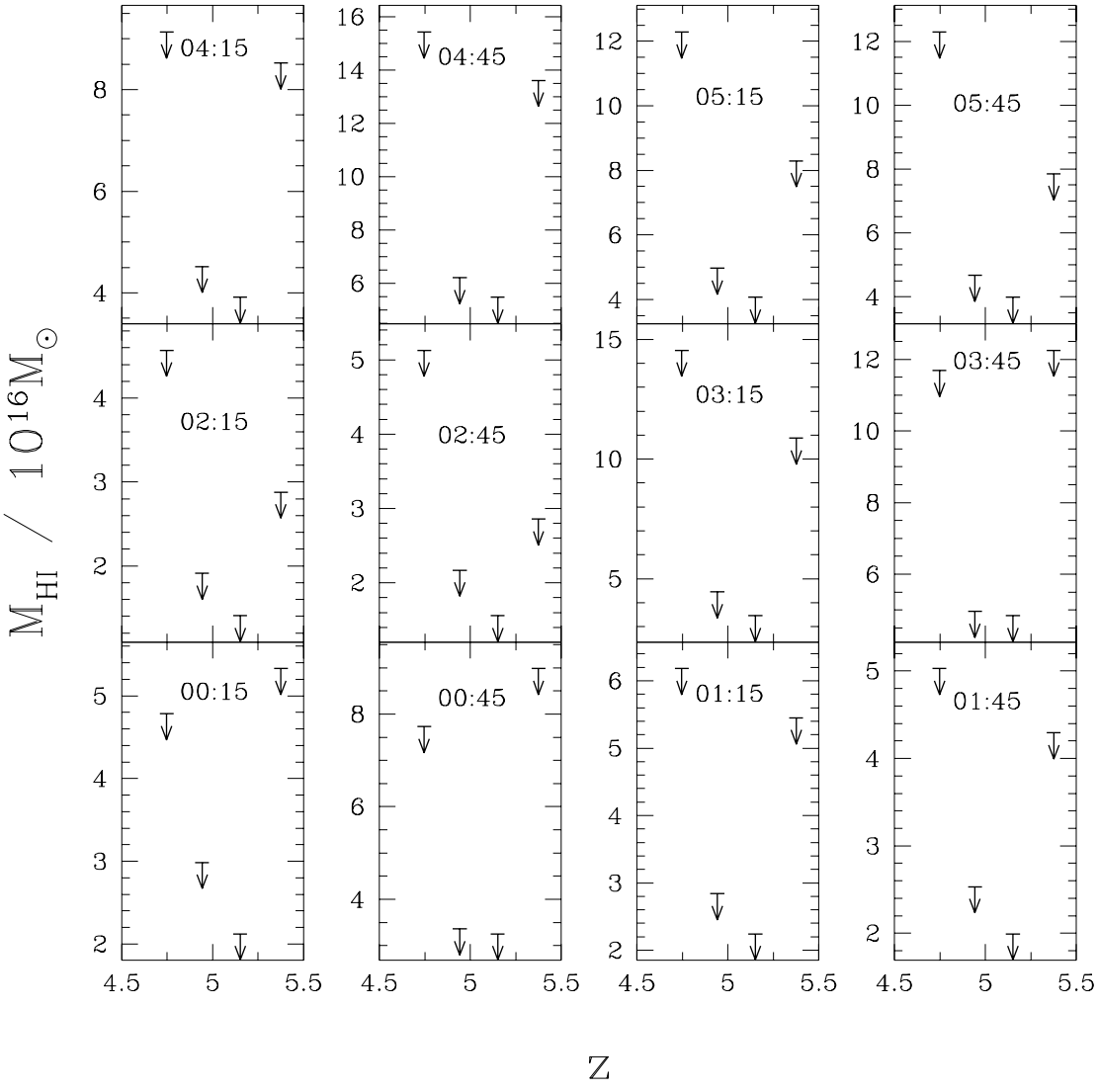

Figure 3-1: The (1σ) upper limits on the HI mass of undetected protocluster clouds in our fields. Each of the four redshift points for each 30^m field represents the mean redshift of an 8 MHz subband; these redshifts are 4.747, 4.942, 5.151, and 5.375. The field center LMST labels each plot. Note the mass scale is in $10^{16}\,M_\odot$.

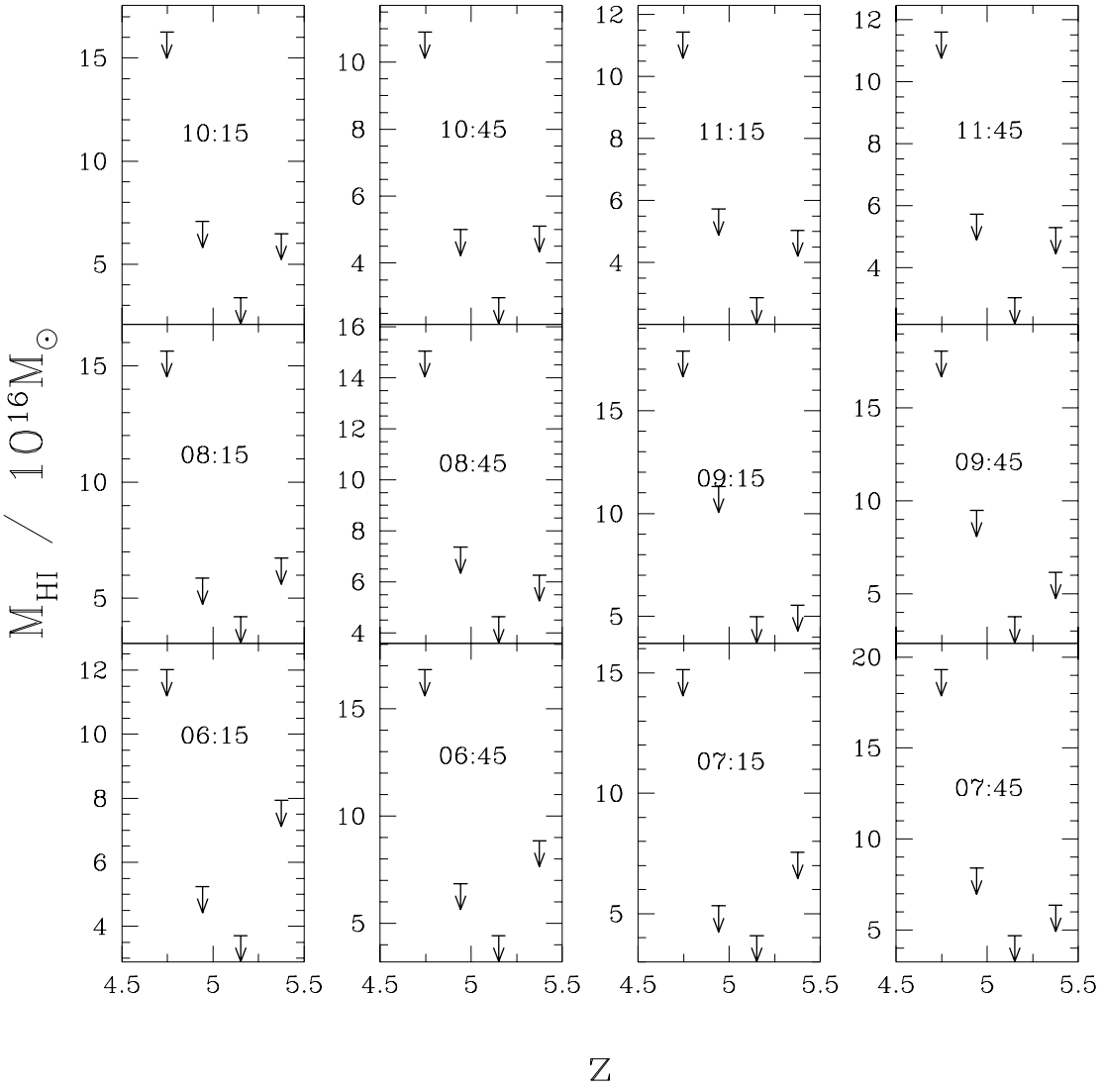

Figure 3-2: The (1σ) upper limits on the HI mass of undetected protocluster clouds in our fields. Each of the four redshift points for each 30^m field represents the mean redshift of an 8 MHz subband; these redshifts are 4.747, 4.942, 5.151, and 5.375. The field center LMST labels each plot. Note the mass scale is in $10^{16}\,M_\odot$.

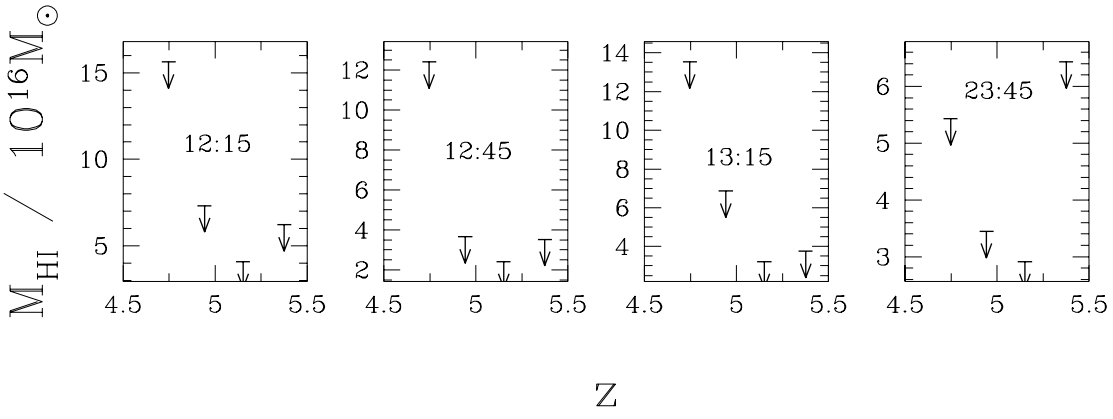

Figure 3-3: The (1σ) upper limits on the HI mass of undetected protocluster clouds in our fields. Each of the four redshift points for each $30^{\rm m}$ field represents the mean redshift of an 8 MHz subband; these redshifts are 4.747, 4.942, 5.151, and 5.375. The field center LMST labels each plot. Note the mass scale is in $10^{16}\,{\rm M}_\odot$.

Chapter 4

Arecibo Gain Modeling

Examining the data shortly after installation of the spectrometer at Arecibo, it seemed the system sensitivity was not as high as hoped, and that the feeds were not performing as expected. Radio frequency interference (RFI) was also seen to be worse than expected. We thought things might be improved if we could design a feed that would have very low sidelobes toward the horizon, and that would illuminate the dish in an optimal way.

An antenna is a device that serves as a coupling between electromagnetic waves traveling in a transmission line and waves traveling in free space. An aperture antenna does this in two stages, the feed illuminating an aperture which restricts the response over the sky. The feed and reflector are designed as a pair to produce the desired beam shape and sensitivity. In this chapter I will describe the analytic and numerical work performed to answer the question, "Given the Arecibo dish with which to work, what are the desirable properties of a point feed, and how should it be placed, to reap the greatest possible sensitivity?"

4.1 Simple Antennae

A passive antenna is interface between two media, free space and a transmission line. The usual phenomena at an interface take place – transmission, reflection, attenuation. The following are some results that apply in general; this discussion follows that of Kraus (1988) .

In figure 4-1 we represent and antenna and its termination as circuit elements. Assume the size of the circuit is small compared to the wavelength, so there is no wave propagation

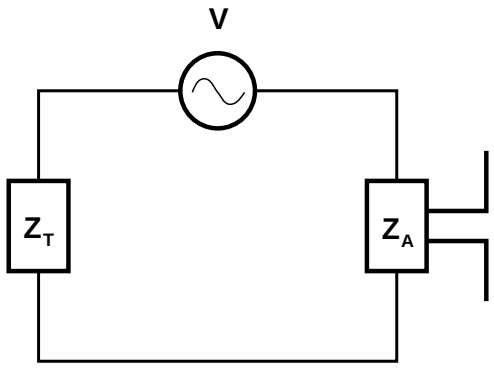

Figure 4-1: An idealized circuit consisting of an antenna and matched load represented by discrete elements. Note we avoid discussion of transmission lines by assuming the driving voltage wavelength $\lambda \gg D$, where D is the size of the circuit.

within the circuit between elements, as in a transmission line. This diagram applies whether we consider transmission or reception; let's consider the former. A voltage source puts energy into the system. $Z_T = R_T + X_T$ is the internal impedance of the generator. The antenna has impedance $Z_A = R_A + X_A$. We will further idealize the situation to simplify the discussion. We are interested in having maximum power transfer from the load to the antenna, and so we will assume $Z_T = Z_A^*$. Therefore as power flows from T to A there is no reflection at A back to T. We will also assume the antenna is lossless, that there is no dissipation of power in the form of heat. However, neither R_T nor R_A need be zero; the generator itself will in general consume energy, and the antenna will radiate energy out of the system. In this case R_A is called the radiation resistance of the antenna. For unity power factor $R_T = R_A$ and $X_T = -X_A$.

In steady state a current

$$I = \frac{V}{\sqrt{(R_A + R_T)^2 + (X_A + X_T)^2}}$$

is set up in the circuit. The maximum power dissipated in A is

$$P_A = I^2 R_A = I^2 R_T = P_T = \frac{V^2}{R_A}.$$

So in the case of maximum power transfer, an equal amount of energy is consumed in the termination as is transmitted by the antenna. The power will in general not be radiated isotropically; its angular dependence is called the power pattern of the antenna, and it depends on the detailed geometry of the conductors comprising the antenna (as well as it's terminating impedance and transmission line length, but as we've noted those details have been swept under the rug). Near the antenna (within a few wavelengths) the fields are complicated, with energy being stored in the reactive components of the antenna impedance. But sufficiently far away ($r \gg \lambda$) the fields become transverse and decay only as $1/r$. In that regime, we can define the power pattern by

$$p(\hat{\mathbf{n}}) = \frac{dU}{d\Omega}(\hat{\mathbf{n}}) \Big/ \frac{dU}{d\Omega}(\hat{\mathbf{n}}_0) \tag{4.1}$$

where $dU/d\Omega$ is the energy radiated into an infinitesimal cone about $\hat{\mathbf{n}}$, and $\hat{\mathbf{n}}_0$ is the direction of maximum power. The pattern can be tailored to fit one's particular need; in our case we want most of the power to come out in a main lobe of some width, and to have the side and rear lobes as low as possible so that we illuminate the main reflector efficiently. If one were interested in signals from the horizon, a toroidal power pattern would do the trick.

Now to reception; when a wave of flux S $\mathrm{Wm}^{-2}\mathrm{Hz}^{-1}$ is incident from some direction, it will excite the antenna and produce a voltage V' at the antenna terminals. The same circuit diagram in figure 4-1 applies, and for maximum power transfer $Z_A = Z_T^*$. The antenna acts as the voltage source, with an internal resistance R_A. Once again, an equal power is dissipated in the load and *lossless* antenna. So, half the power extracted from the incident wave is scattered by the antenna and does not reach the load. The dependence of V' on the direction of incidence is also a result of details of construction.

We can define an *effective* aperture via

$$A_e(\hat{\mathbf{n}}) = P_T/S(\hat{\mathbf{n}}) \tag{4.2}$$

where $S(\hat{\mathbf{n}})$ means a wave incident *from* direction $\hat{\mathbf{n}}$, and a *scattering* aperture via

$$A_s(\hat{\mathbf{n}}) = P_A/S(\hat{\mathbf{n}}) \tag{4.3}$$

where P_A is the power scattered or reradiated by the antenna. As an aside, In the case of matched termination, equations 4.2 and 4.3 show $A_e = A_s$. This is not true in general; if there is mismatch between the antenna and load, the power reflected from the load will be reradiated. If we replace the termination by a short circuit, all of the power absorbed will be reradiated, so $A_e = 0$. It is possible to design an antenna that scatters in exactly the same pattern as it radiates (Collin & Zucker 1969), called a minimum-scattering antenna; such an antenna when short-circuited will radiate a field that cancels the scattered field, and is then invisible. In fact, being matched does not guarantee $P_A = P_T$. It is possible to build an antenna that when hooked to a matched load has $P_A > P_T$, but in which P_A is not maximized. When the termination impedance is changed to maximize P_A, $P_A = P_T$ (Collin & Zucker 1969). A short dipole is an example of a minimum scattering antenna.

It is intuitive and in fact true that the functions $A_e(\hat{\mathbf{n}})$ and $p(\hat{\mathbf{n}})$ are the same apart from normalization. This is the *Reciprocity Theorem of Helmholtz*, an extension of the result from electrostatics that the mutual inductance matrix of a system of conductors is symmetric. The *antenna beam solid angle* is

$$\Omega_A = \int_{4\pi} p(\hat{\mathbf{n}}) d\Omega \tag{4.4}$$

and the gain, a measure of the directivity of the antenna response, is

$$G = 4\pi/\Omega_A \tag{4.5}$$

4.2 Parabolic and Spherical Reflector Antennae

One can greatly increase the gain of a simple antenna by placing it above a reflecting plane. It's simple to see that the power that can no longer flow in the direction through the plane must be directed away, though not all will go into the main lobe. By shaping the reflector

and the feed antenna power pattern the side lobes can be reduced.

For very large antennae, an obvious choice for a reflecting surface is a parabola. If the feed is placed at the focus, then the radiated fields reflect off the dish according to Snell's Law and emerge from the aperture rays collimated and wavefronts in phase. By reciprocity, a wave normally incident on the aperture will be focused, in phase, onto the feed. The effective aperture of the parabolic reflector antenna is the physical area of the aperture. Of course the preceding discussion holds true, and half the power incident on the feed will be reflected back to the dish; this unfortunately can give rise to standing waves due to multiple reflections from the sub-feed point and is a ubiquitous problem in radio telescopes. Also, due to power carried in these reflected waves the effective impedance of the feed is different than would be measured at an antenna range and should be considered if optimum performance is desired (Silver 1949).

A parabolic antenna has one focal point. Actually, the size of the focal region is about a wavelength in diameter (Ruze 1978), so simultaneous multifrequency observations are possible. As the feed is moved away from the focus transverse to the optical axis, the peak of the antenna power pattern lowers and moves in the opposite direction. This is one method of steering the beam of a large telescope without moving the dish, but gain suffers. On the other hand, a spherical reflector has an infinite number of optical axes defined by the line from the center of curvature to the feed point, offering simultaneous multibeam operation. The downside is that a sphere focuses incident plane waves onto a line, not a point. If you illuminate a sphere with a point feed the wavefronts leaving the aperture will not be plane, even neglecting diffraction, and this is called spherical aberration. The focal line starts at the paraxial surface, the sphere of radius $R/2$ where rays very close to the optical axis converge, end extends downward to a distance that depends on the aperture illuminated. The phase of the waves focused along this line, relative to paraxial, as a function of distance below the paraxial surface, the *longitudinal astigmatism*, is (Spencer 1978)

$$\phi(l) = \frac{2\pi R}{\lambda}[\frac{l}{R/2 + l} - \frac{l}{R}]$$

The largest telescope in the world, Arecibo Observatory, is a spherical reflecting dish. It was

originally illuminated by line feeds that corrected for longitudinal astigmatism by injecting a corrective phase along the line feed. Recently it has been fitted with specially shaped secondary and tertiary reflectors to correct for the aberrations and illuminate a larger fraction of the dish. If you do illuminate a perfect spherical-cap reflector with a point feed, the phase error function in the aperture, representing the departure of exiting wavefronts from plane, and computed using ray tracing, is

$$\delta(\rho) = \frac{2\pi}{\lambda}\left(R(2-m) - \sqrt{R^2 - P^2}\right) - \begin{cases} \frac{\sqrt{R^2-\rho^2}-\sqrt{R^2-P^2}}{\cos(2\alpha-\theta)} + \frac{\rho}{\sin\theta} & \text{if } \rho \neq 0 \\ R(2-m) - \sqrt{R^2-P^2} & \text{if } \rho = 0 \end{cases} \tag{4.6}$$

where

$$\begin{aligned} m &= 1 - f/R \\ \tan\theta &= \frac{\rho}{\sqrt{R^2-\rho^2} - mR} \\ \tan\beta &= \frac{\rho}{\sqrt{R^2-\rho^2}} \\ \cos\alpha &= \sin\theta\sin\beta + \cos\theta\cos\beta \end{aligned}$$

Figure 4-2 shows the geometry and defines the constants in equation 4.6. Figure 4-3shows the value of δ over the aperture of a dish similar to Arecibo's, at a wavelength of 1.27 m.

4.3 Aperture Antenna Power Patterns

We said that the power pattern of a wire antenna is difficult to calculate, depending on the details of construction. The pattern produced far away from apertures much larger than the wavelength depends mainly on the shape of the aperture and can be computed more readily. We start with the expression for diffraction of a scalar field by an aperture (Jackson 1975)

$$\Psi(\mathbf{x}) = \frac{k}{2\pi i}\int_S \frac{e^{ikR}}{R}\left(1 + \frac{i}{kR}\right)(\hat{\mathbf{n}}\cdot\hat{\mathbf{R}})\Psi(\mathbf{x}')dS' \tag{4.7}$$

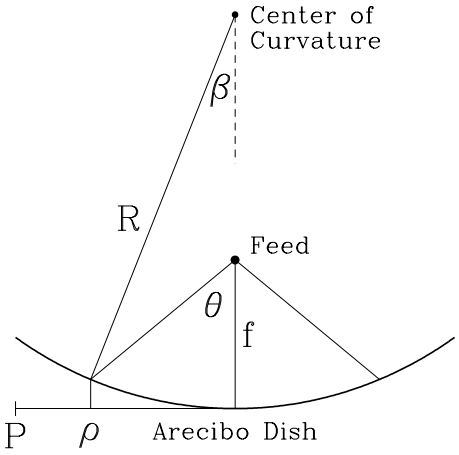

Figure 4-2: The geometry for the calculation described by equations 4.6. There is cylindrical symmetry about the radial line from the feed to the dish.

where $\mathbf{x}$ is the observation point, S is the aperture surface with unit normal $\hat{\mathbf{n}}$, $\mathbf{x}' \in S$, and $\mathbf{R} = \mathbf{x} - \mathbf{x}'$. Now we will take $x \gg x'$, so that $|\mathbf{x} - \mathbf{x}'| \simeq x - \mathbf{x}' \cdot \hat{\mathbf{x}}$, and we discard the term $\propto R^{-2}$ compared to R^{-1}.

$$\Psi(\mathbf{x}) = \frac{-ik}{2\pi} \frac{e^{ikR}}{R} (\hat{\mathbf{n}} \cdot \hat{\mathbf{R}}) \int_S e^{-ik\hat{\mathbf{R}}\cdot\mathbf{x}'} \Psi(\mathbf{x}') dS' \tag{4.8}$$

The power radiated through the point $\mathbf{x}$ is $|\Psi(\mathbf{x})|^2$, and over the angles where it is appreciable $(\hat{\mathbf{n}} \cdot \hat{\mathbf{R}})$ is approximately one. The power radiated into a small cone about $\mathbf{x}$ is $P(\hat{\mathbf{x}}) = \frac{1}{2} R^2 |\Psi(\mathbf{x})|^2$, and the total power passing through the aperture is $P_{\rm tot} = \frac{1}{2} \int_S |\Psi(\mathbf{x}')|^2 dS'$. Let $\Psi(\mathbf{x}) = f(\mathbf{x}) e^{i\delta(\mathbf{x})}$, where f is the field strength in the aperture and δ a phase error. We have finally that the gain is

$$G(\hat{\mathbf{n}}) = \frac{4\pi P(\hat{\mathbf{n}})}{P_{\rm tot}} = \frac{4\pi}{\lambda^2} \frac{\left| \int_S f(\mathbf{x}') e^{-i\mathbf{k}\cdot\mathbf{x}'} e^{i\delta(\mathbf{x}')} dS' \right|^2}{\int_S f^2(\mathbf{x}') dS'} \tag{4.9}$$

where $\mathbf{k} = (2\pi/\lambda)\hat{\mathbf{R}}$.

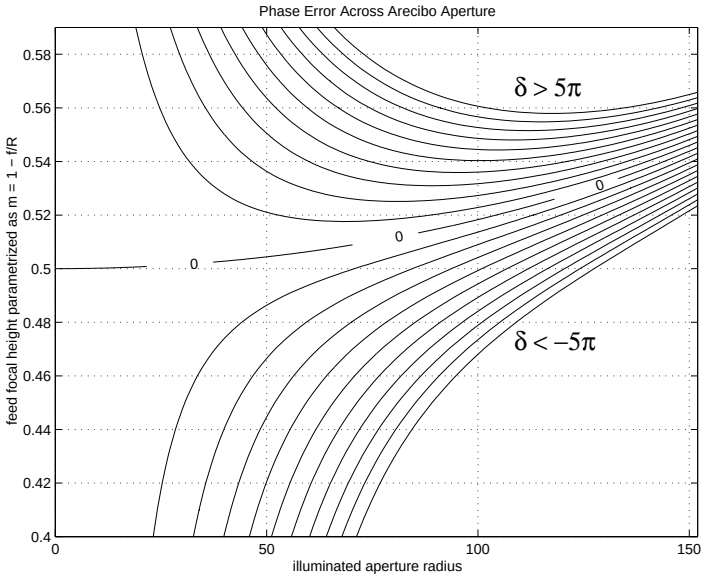

Figure 4-3: The phase error across the aperture of the Arecibo dish as expressed in equation 4.6. Contours are in increments of $\pi/2$.

4.4 Arecibo Gain via the Ruze Formula

Equation 4.9, when $\mathbf{k} \cdot \hat{\mathbf{x}} = 1$, expresses the effect of phase errors on the maximum gain of the antenna. Ruze (1952) investigated the case when $\delta(\mathbf{x}')$ is a random variable from a Gaussian distribution of zero mean, standard deviation $\delta_{\rm rms}$, and of various correlation lengths. When the correlation scale is large compared to wavelength, the loss in gain due to the phase error is given by the Ruze formula,

$$\frac{G}{G_0} = e^{-\delta_{\rm rms}^2}, \tag{4.10}$$

and if one defines an effective reflector surface tolerance ϵ as the *axial* component of the surface *normal* deviation from parabolic, and then define its standard deviation as

$$\epsilon_0^2 = \frac{\int_S \epsilon^2 f(\mathbf{x}') dS'}{\int_S f(\mathbf{x}') dS'} \tag{4.11}$$

then the loss of gain is

$$\frac{G}{G_0} = e^{-(4\pi\epsilon_0/\lambda)^2}. \tag{4.12}$$

This equation was derived assuming an error correlation length large compared to wavelength, and small phase error magnitude. Figure 4-3 shows $|\delta|$ can exceed 5π within Arecibo's aperture; nevertheless we can attempt to estimate the loss of gain due to spherical aberration with this formula, and come up with an answer very close to correct. We duplicate an analysis due to J. Weintroub (1998) , performed during the planning of the experiment in order to estimate the sensitivity and integration time to detection.

For application of the Ruze formula, the mean phase error across the aperture should be zero, whereas in general it will not be for a given illuminated spherical cap. So for each trial aperture radius P we must compute a mean-subtracted error function. We do this by finding the parabola that minimizes the area-weighted path length difference from the sphere; we can then compute the rms surface deviation of that parabola from the sphere and apply the Ruze formula.

$$\mathcal{U}(\rho) = R - \sqrt{R^2 - \rho^2} \tag{4.13}$$

$$\mathcal{V}(\rho) = A\rho^2 + B \tag{4.14}$$

$$\Delta(P) = \frac{1}{\pi P^2}\int_0^P (\mathcal{U}(\rho) - \mathcal{V}(\rho))^2 2\pi\rho \, d\rho \tag{4.15}$$

and we want A, B such that

$$\frac{\partial\Delta}{\partial A} = \frac{\partial\Delta}{\partial B} = 0;$$

This leads to expressions for A and B,

$$A_{\rm m} = \frac{4}{5Rx^6}\Big[5x^2 - 4 + (1-x^2)^{\frac{3}{2}}(4+x^2)\Big] \tag{4.16}$$

$$B_{\rm m} = -\frac{R}{15x^4}\Big[4(1-x^2)^{\frac{3}{2}}(6-x^2) - (15x^4 - 40x^2 + 24)\Big] \tag{4.17}$$

where $x = P/R$, and then to a value of the root-mean-square surface deviation from the

parabola as in equation 4.11, assuming uniform illumination

$$\epsilon_{\rm m}^2 \quad = \quad \frac{\int_0^P (\mathcal{U}_{\rm m}(\rho) - \mathcal{V}_{\rm m}(\rho))^2 2\pi\rho \, d\rho}{\int_0^P 2\pi\rho d\rho} \tag{4.18}$$

The results for Arecibo are presented in figure 4-4 and 4-5. From the former, one can see that an aperture up to about 220 m in diameter can be illuminated before the gain is appreciably affected. Of course one would like as large an effective area as possible, and the latter figure shows that it falls off very quickly as the phase errors increase. Clearly one should illuminate an aperture of diameter about 195 m. Sensitivity is proportional to effective area, see equation 4.5.1.

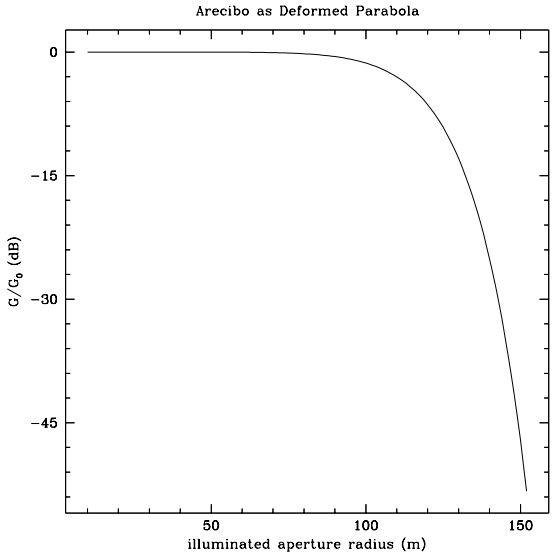

Figure 4-4: The reduction in gain of a spherical reflector, referred to a parabola of the same aperture. The calculation, via equations 4.10 through 4.18, has been scaled for Arecibo.

4.5 Maximizing Sensitivity

4.5.1 Characterizing Performance

During the diagnostic phase after installation of the experiment the noise in the system seemed rather high, and we decided some of it might be due to a misplacement of our feeds.

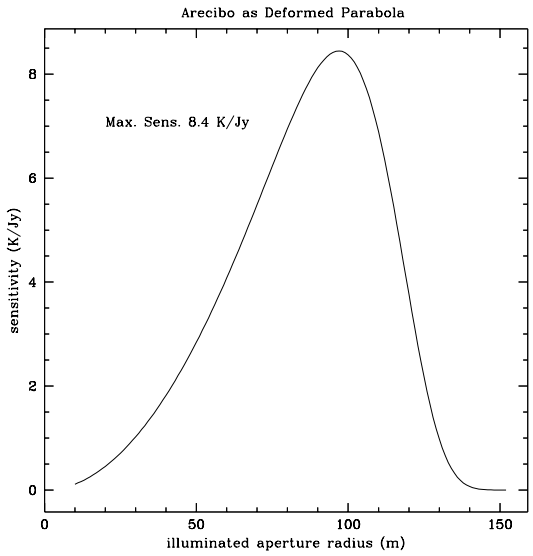

Figure 4-5: The sensitivity of Arecibo illuminated by a point feed, as a function aperture radius.

The foregoing analysis prescribes a focal height and a uniformly illuminated aperture to maximize forward gain, but does not take into account the noise added to the system when the feed illuminates regions outside the dish, called spillover or vignetting. An important measure of performance is the ratio of the power in the signal to the noise power in the system in the absence of signal, both of which depend on feed placement and orientation. Further, the assumption in equation 4.10 is that surface errors are distributed randomly whereas spherical aberration is not. Finally, we would like to know if we can make large improvements with small effort, like squinting the feed inboard a few degrees or turning it so that a high sidelobe points toward the dish instead of the ground. The starting point is equation 4.9 except now the feed power pattern is not zero off the dish, so the gain is lowered by the ratio of the power spilt off the dish to the total power radiated by the feed,

$$G' = G\frac{\int_{\text{dish}} p(\hat{\mathbf{n}})d\Omega}{\int_{4\pi} p(\hat{\mathbf{n}})d\Omega} \tag{4.19}$$

where $p(\hat{\mathbf{n}})$ is the feed power pattern, and G is as defined in equation 4.9.

We must quantify the system noise[1]. Taking again Figure 4-1, imagine the terminating impedance Z_T is at a physical temperature T, and the voltage source is actually the random fluctuating voltage across the load due to the thermal oscillations of electrons and phonons. A result due to Nyquist is that the specific power dissipated in the impedance is $P_T = kT$, where the units of P_T are WHz^{-1}, as before. When the impedance is matched this is also the power supplied to Z_A, and so the antenna radiates a total power kT. So with our previous definitions we have

$$\begin{aligned} kT &= \int_{4\pi} \frac{dU}{d\Omega} d\Omega = \frac{dU}{d\Omega}(\hat{\mathbf{n}}_0) \int_{4\pi} p(\hat{\mathbf{n}}) d\Omega = \Omega_A \frac{dU}{d\Omega}(\hat{\mathbf{n}}_0) \\ &\Rightarrow \quad \frac{dU}{d\Omega}(\hat{\mathbf{n}}_0) = kT/\Omega_A = A_e kT/\lambda^2 \\ &\Rightarrow \quad \frac{1}{A_e}\frac{dU}{d\Omega}(\hat{\mathbf{n}}_0) = kT/\lambda^2 = \frac{1}{2} B_\nu^{\mathrm{RJ}} \end{aligned}$$

So the antenna radiates, in at least one direction, a specific intensity equal to *one half* that of a black body of temperature T in the Rayleigh-Jeans limit. And because A_e is a function of direction, it turns out to be true for all directions – the antenna looks like a black body of area $A_e(\hat{\mathbf{n}})$. It radiates only half the energy of a real black body because it must radiate polarized waves, and thermal emission is unpolarized. Note that the T one would infer by measuring the flux from the antenna has to do with the termination, not the antenna itself. We assumed it was lossless, so formally it's at $T = 0$. Now by reciprocity we can say if the antenna observes radiation from a collection of black bodies at various temperatures $T_b(\hat{\mathbf{n}})$, the noise equivalent temperature at the terminals of the antenna, T_A, is given by

$$T_A = \frac{1}{\Omega_A} \int_{4\pi} T_b(\hat{\mathbf{n}}) p(\hat{\mathbf{n}}) d\Omega \tag{4.20}$$

This is one contribution to the noise floor in our system. The signals received by the feed will be transmitted, amplified, filtered, amplified, transmitted, *etc.*, and each stage will add some extra noise power. The power added by a lossy transmission line depends on the

[1] I may sometimes use "noise" in an imprecise and disparaging way, referring to any signal interfering with detection of the signal of interest. Strictly speaking the signal, produced naturally, is noise too because it is characterized by a band-limited noise power spectrum.

ambient temperature; the lossier the line the higher the optical depth down it and the closer T_L comes to the physical temperature. The contribution of the first stage of amplification, T_R, is the most important, and this can be measured in the lab and is usually not very dependent on environment.

So we can estimate the noise floor in the absence of our signal of interest. When we observe the signal it will add some noise power, and so the signal-to-noise ratio is its contribution divided by the total.

$$\begin{aligned} T_{\rm sig} &= S_\nu \Gamma = S_\nu \frac{A_e}{2k} \\ T_{\rm sys} &= T_{\rm sig} + T_A + T_R + T_L \\ {\rm SNR} &= T_{\rm sig}/T_{\rm sys} \end{aligned}$$

I take as constants $T_L = 10$K, and $T_R = 50$K, which subsequent measurement has found to be optimistic(see figure 2-5, $T_R \approx 120$K). In our case, $T_{\rm sig} \ll T_A$, so we ignore its contribution to $T_{\rm sys}$. SNR is dimensionless, but is not the most useful parameterization because we need to know S_ν; so it's better to consider SNR/S_ν, SNR per Jy, or its reciprocal the System Equivalent Flux Density (SEFD), which is the flux of a celestial source that would double the system temperature. The latter is a common figure of merit for radio telescopes, and is equal to $T_{\rm sys}/\Gamma$.

4.5.2 Degrees of Freedom

The goal is to maximize (minimize) SNR/Jy (SEFD), in the specific context of our experiment at Arecibo. Given a feed power pattern, we compute, by numerical integration, Γ according to equation 4.19 and T_A by equation 4.20. For the latter, we break the world as seen by the feed into four domains: the dish, which has a brightness temperature equal equal to the sky's; the ground screen around the dish which shields against spillover, which we also take to be the sky temperature; the ground that extends from the screen edge to the horizon and is warm, about 300K; and the hemisphere of the sky, which we take to be 90K. At our frequencies the sky brightness temperature ranges from 90K to 1500K in total

intensity. An error in the analysis described here is that, of course, our feed is polarized and so the ambient temperatures should have been halved in their contribution to T_A. It will turn out the results of interest are not very sensitive to such a change, and it is also partly offset by our optimistic estimate of T_R. So we have

$$T_A = \frac{1}{\int_{4\pi} p d\Omega}\{\int_{\text{dish}} T_{\text{sky}} p d\Omega + \int_{\text{scr}} T_{\text{sky}} p d\Omega + \int_{\text{gnd}} T_{\text{gnd}} p d\Omega + \int_{\text{sky}} T_{\text{sky}} p d\Omega\} \tag{4.21}$$

4.5.3 Investigating Illumination Patterns

The integral in the numerator of equation 4.19 is over the aperture surface. Because we are expressly considering non-axisymmetric illumination patterns, and will include measured feed patterns in our numerical evaluation, I would like to chose coordinates that will be convenient for that purpose. The coordinate system for the integration is then the spherical coordinates centered on the feed, with z pointing toward the dish but off radial by at some squint α. Figures 4-6 and 4-7 lay out the coordinate system used. I will perform the integration over spherical coordinates, but my z axis is misaligned with the axial z by the squint angle α. Therefore, the feed-aligned angles θ' and ϕ', are related to the dish normal coordinates implicitly by

$$\tan\phi = \tan\phi'\cos\alpha + \frac{\cos\theta'\sin\alpha}{\cos\phi'\sin\theta'} \tag{4.22}$$

$$\cos\theta = \cos\theta'\cos\alpha - \sin\theta'\sin\phi'\sin\alpha \tag{4.23}$$

These, plus the equation for the aperture radius variable

$$\rho(\theta) = R\sin\theta\{\sqrt{1 - m^2\sin^2\theta} - m\cos\theta\} \tag{4.24}$$

give me the Jacobian for coordinate transformation. In what follows, I will sometimes present results as plots of sensitivity and SNR/Jy. They are related to G as follows: $\Gamma = \lambda^2 G/4\pi$, and $\text{SEFD} = \Gamma/T_{\text{sys}}$.

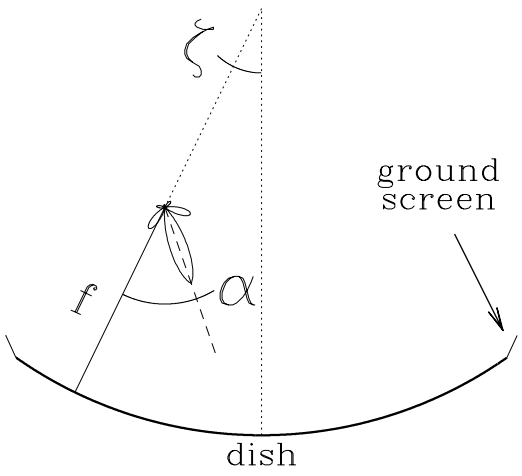

Figure 4-6: The geometry of our experiment at Arecibo, to scale. The feed is at focal height f, zenith angle ζ, and squinted inboard by angle α. The ground screen that shields feeds from spilling over onto hot ground is also shown.

4.6 Feed Design Results

An interesting check is to redo the calculation of section 4.4, the sensitivity of a uniformly illuminated Arecibo with no spillover. They agree nicely, as presented in Figure 4-8, in which I over-plotted the "deformed parabola" results. Note the latter come to predicting the best focal height and aperture. The peak Γ is close as well, 8.4 K/Jy (figure 4-5) compared to 8.8 K/Jy. However, off–peak the direction of slowest descent is not as well predicted.

With parabolic reflector antennae, in general the highest gain is achieved with uniform illumination; for instance all the VLA antennae are uniformly fed (Perly *et al.* 1989). With spherical aberration however, the phase error increases with wider illumination and eventually offsets the collecting area. Even if you could you would not want to illuminate all of

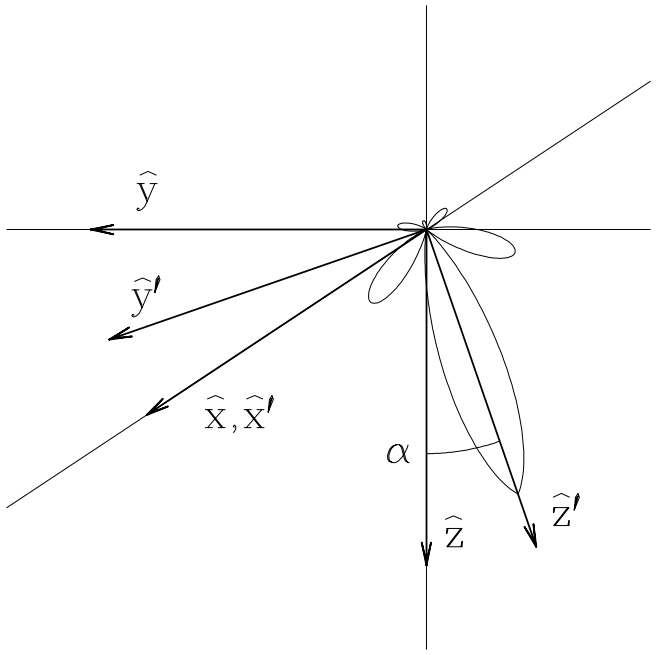

Figure 4-7: The coordinate system used for the calculations of section 4.5.3. The unit vector $\hat{\mathbf{z}}$ is parallel to the optical axis. The feed is squinted inboard an angle α, defining the primed coordinate axes. The angles (θ, ϕ) and (θ', ϕ') are defined with respect to the axes in the usual way.

Arecibo with a point feed. The first question to answer is what are the gross characteristics, *i.e.* beamwidth and sidelobe level, of a feed that will maximize our sensitivity?

The results from the uniform illumination calculation (figure 4-8) show that the best focal height is at about 128 m, very close to the original placement of our feeds. Other calculations, fixing the opening angle of the cone of illumination and varying the focal height showed the sensitivity to be a very peaked function of f, so in what follows we will fix the feed at that focal height and allow feed pattern and squint to be the parameters.

To investigate the effects of sidelobe level and beamwidth, we computed results for three families of feed patterns (see Figure 4-9), which in order of increasing sidelobe level are:

$$\text{Gaussian}: \qquad p(\theta) = \exp[\kappa_1 \theta/\theta_a]$$

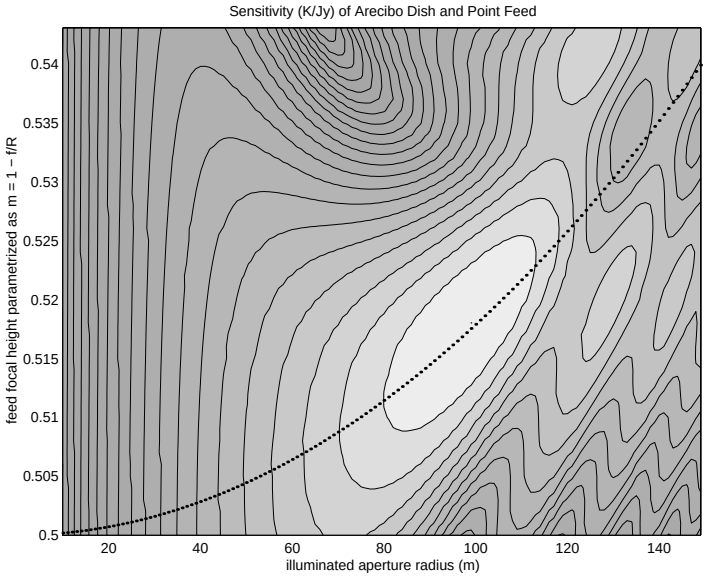

Figure 4-8: The sensitivity of Arecibo, uniformly illuminated, for a variety of apertures and focal heights. The results of section 4.4, where the sensitivity is calculated via the Ruze formula, are over-plotted. Good agreement.

$$\text{Airy}: \quad p(\theta) = 4J_1^2(\kappa_3\theta/\theta_a)/\theta^2$$

$$\text{Bessel}: \quad p(\theta) = J_0^2(\kappa_2\theta/\theta_a)$$

where κ_i is chosen so that all have the same FWHM. The results are presented in figures 4-10 through 4-15. The general features are that the lower the sidelobes the better, and that the optimum beamwidth increases with increasing sidelobe level. This is to offset the phase errors accumulated in the sidelobes by illuminating more of the sub-feed portion of the dish. For realistic sidelobe levels (the Airy pattern), the optimum beamwidth is approximately 44° FWHM.

Having identified some general criteria, we attempted to design a simple feed that would approach them. Early efforts involved arrays of dipoles over a ground plane, but we decided the sidelobes were probably too high, and the structure had high windage, not a desirable property for something suspended hundreds of feet above the dish during hurricane season.

Weintroub (1998) has studied the design of helical antennae, incorporating the use of

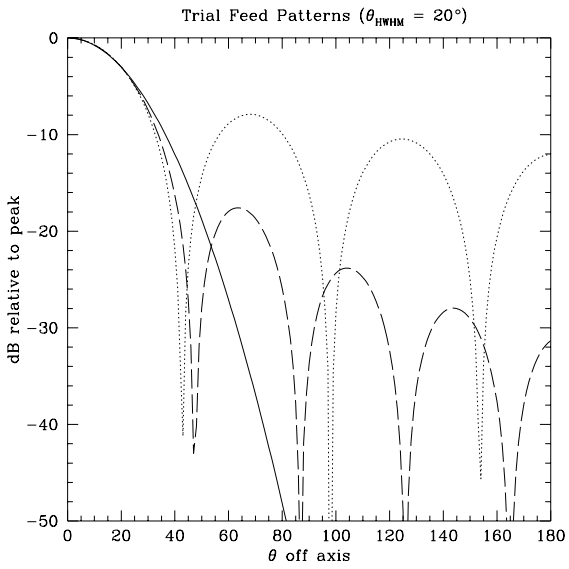

Figure 4-9: Three test feed patterns used in calculations to derive design criteria for beamwidth and sidelobe level.

"soft" or slotted ground planes to lower sidelobes and tailor the beam shape. He has built and measured some 9 GHz prototypes which have improved sidelobes over flat ground plane designs. The measured beam pattern of a particularly good candidate is shown in figure 4-19. A complication is that the power squeezed out of the sidelobes seems perhaps to have gone into the cross-polarized beam response.

With measurements like this in hand, we can estimate the improvement over current sensitivity such a feed would provide. I used simple bilinear interpolation over θ and ϕ to sample the illumination over unmeasured points. I can also rotate the feed pattern to place the highest measured sidelobe away from the horizon where from RFI perhaps emanates. The result, shown in figures 4-22 and 4-21, is that a fair improvement in SEFD is seemingly possible if we tailor the beam pattern to fit our criteria. A reduction in SEFD by a factor f=1.2 results in a reduction of integration time to detection at a given significance level by f^2=1.4. However, we decided not to implement the change for several reasons. Firstly, this analysis has not included several possibly serious factors: aperture blockage by the Arecibo platform, and polarization impurity of the feed, which is worse for the prototype than the

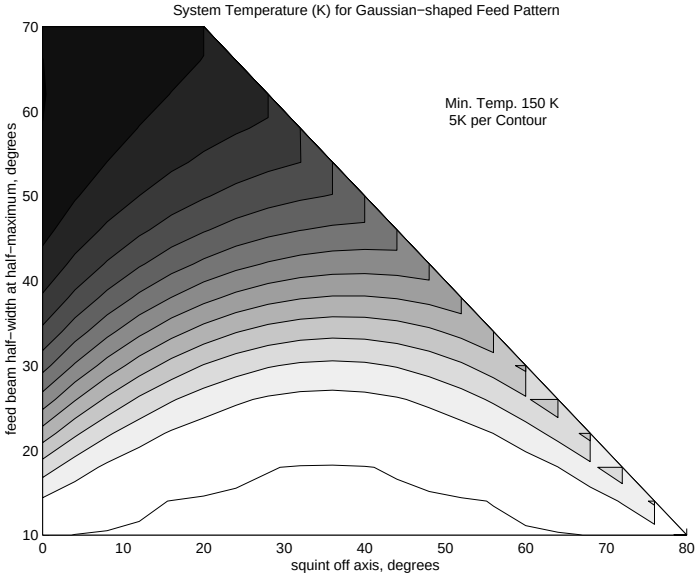

Figure 4-10: The system temperature for a Gaussian feed power pattern. The minimum is at such a squint to point to the center of the dish, and it increases smoothly for increasing beam width. This pattern has no sidelobes.

current helix, at least according to modeling. Secondly, the effort to build and install new feeds is significant, and Arecibo Observatory was and is in the process of a major upgrade which strains the resources available to observers.

In summary, we have produced a method to evaluate the effect of measured feed designs on our experimental sensitivity, and to prescribe an optimum orientation of the feed. Fortunately, the sensitivity is a gentle function of squint and beam size, so considerable leeway is available when trying to match design criteria.

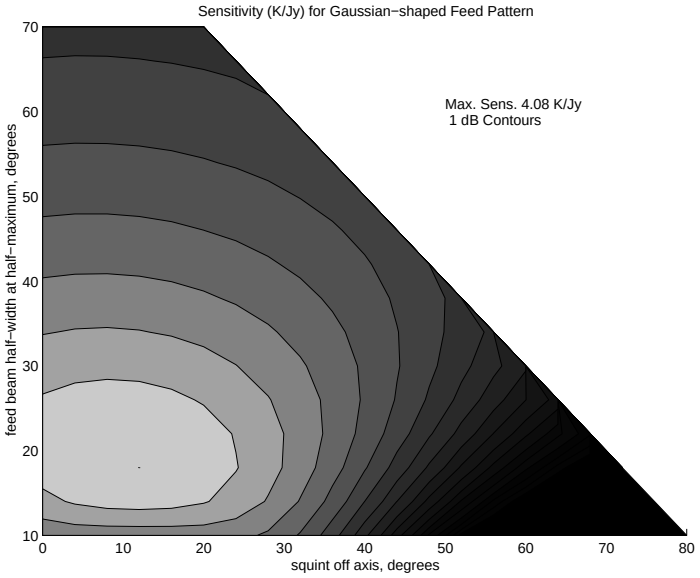

Figure 4-11: The sensitivity for a Gaussian feed power pattern. Again, the smooth behavior is due to lack of sidelobes.

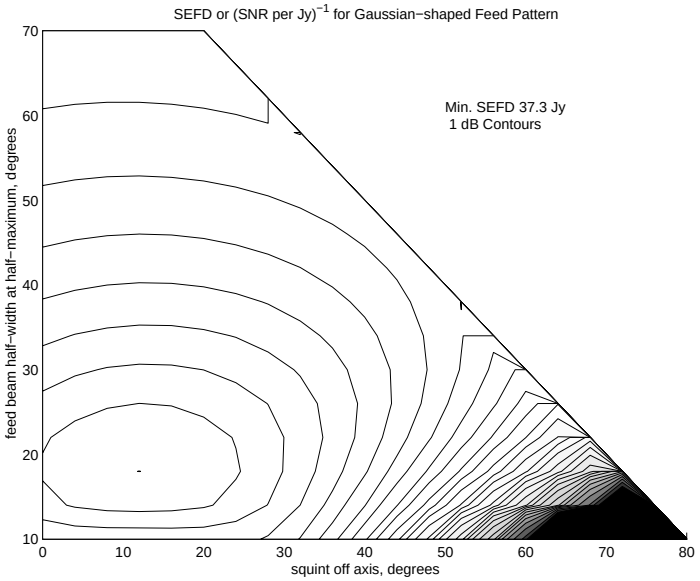

Figure 4-12: The system equivalent flux density for a Gaussian feed power pattern. This is probably a lower limit to the SEFD we might possibly achieve by redesigning our feeds.

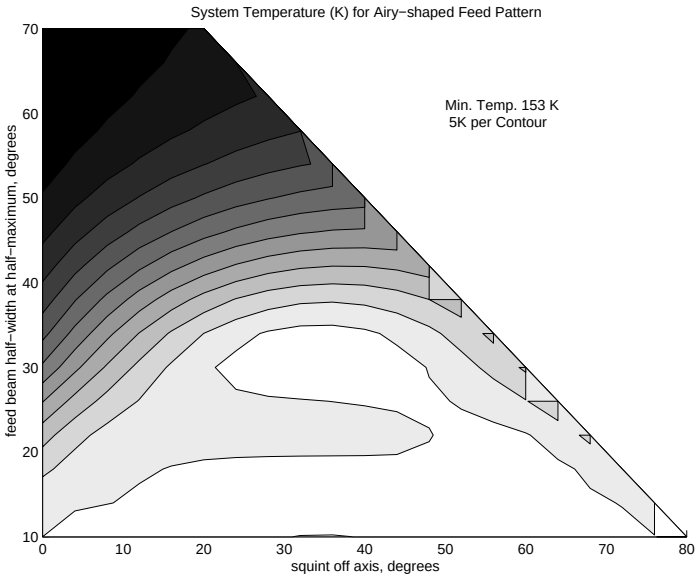

Figure 4-13: The system temperature for an Airy feed power pattern. As the beam width increases, a sidelobe spills over the ground screen onto hot ground, then passes over into the horizon, causing a local maximum at about 20° HWHM.

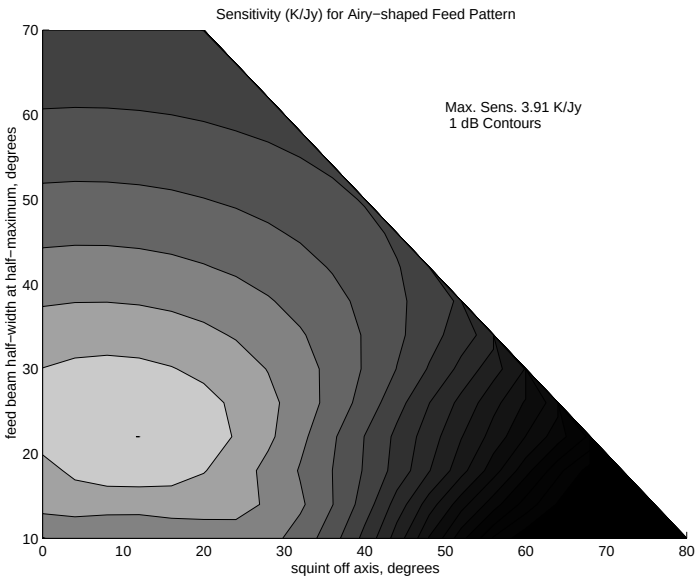

Figure 4-14: The sensitivity for an Airy feed power pattern. The optimum HWHM is higher than Gaussian because of the power lost to sidelobes.

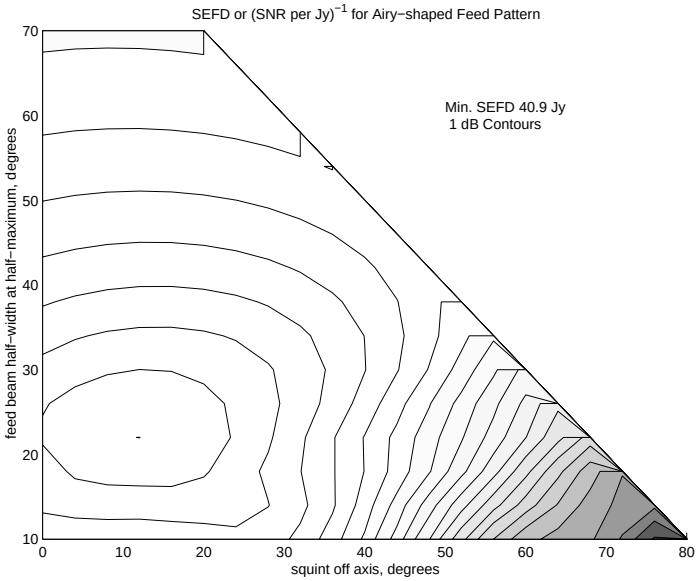

Figure 4-15: The system equivalent flux density for an Airy feed power pattern. This is a more likely value for a realizable feed design.

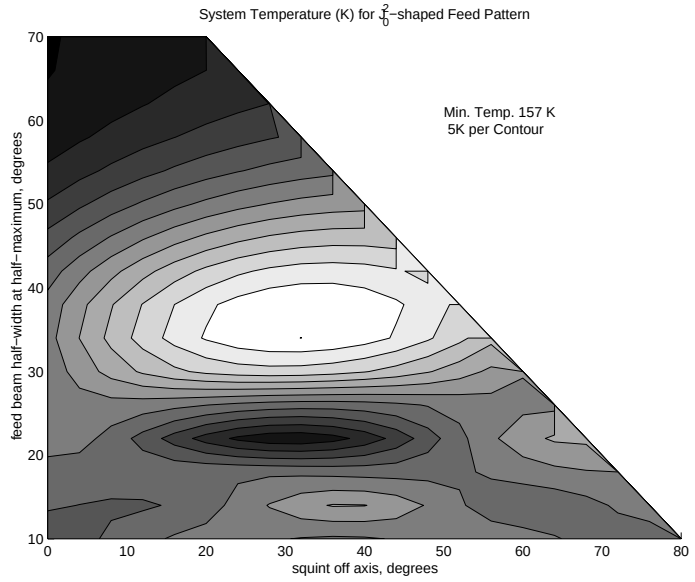

Figure 4-16: The system temperature for a Bessel feed power pattern. The effect of high sidelbes is evident in the multiple maxima as the beamwidth increases.

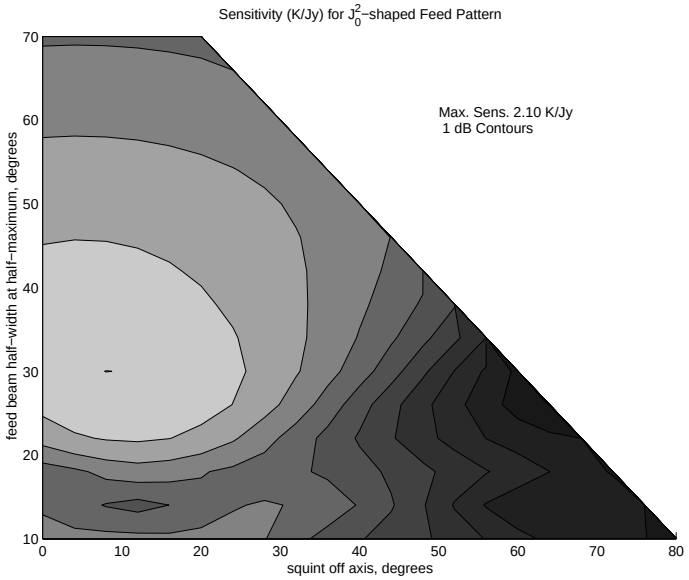

Figure 4-17: The sensitivity for a Bessel feed power pattern. Much effective area is lost to spillover and phase error in the sidelobes.

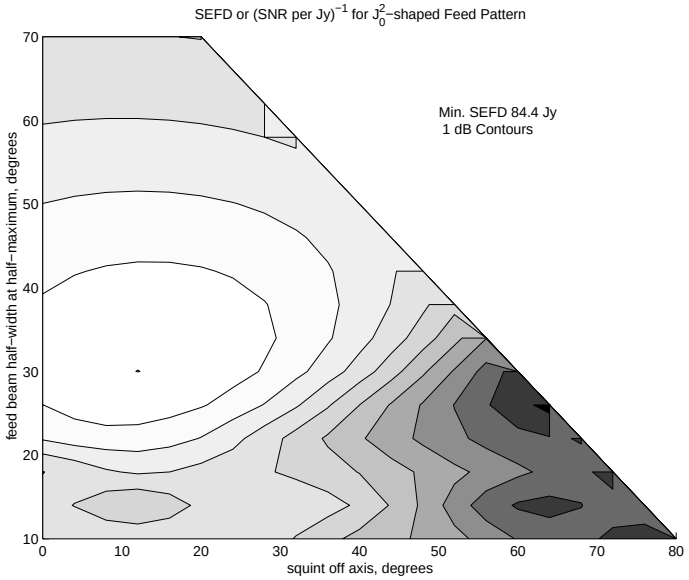

Figure 4-18: The system equivalent flux density for a Bessel feed power pattern. The SEFD at optimum orientation is more than twice as high as the Gaussian case.

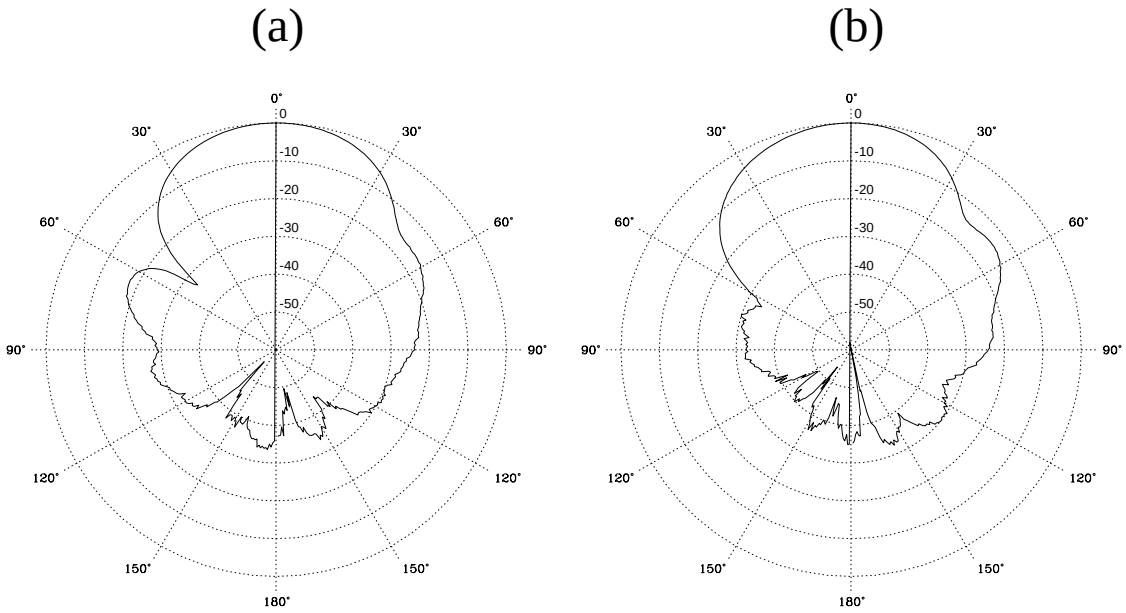

Figure 4-19: The measured pattern of a prototype helix, employing tapering and soft ground plane to lower sidelobe response. (a) the azimuth 0° pattern,(b) the azimuth 90° pattern.

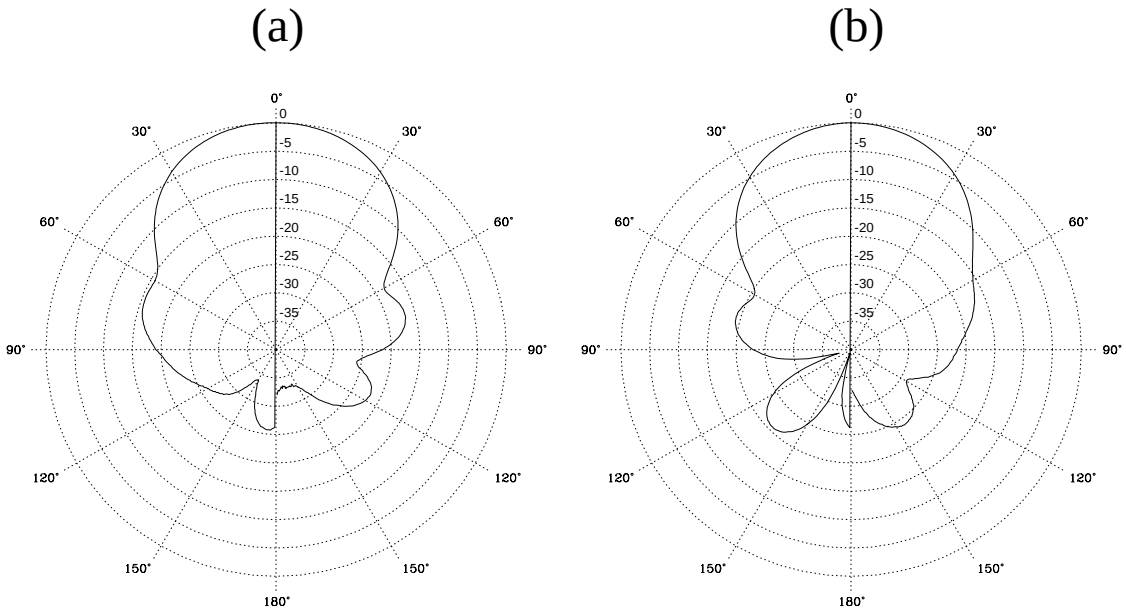

Figure 4-20: The measured pattern of a model of our original, and current, helix. (a) the azimuth 0° pattern,(b) the azimuth 90° pattern.

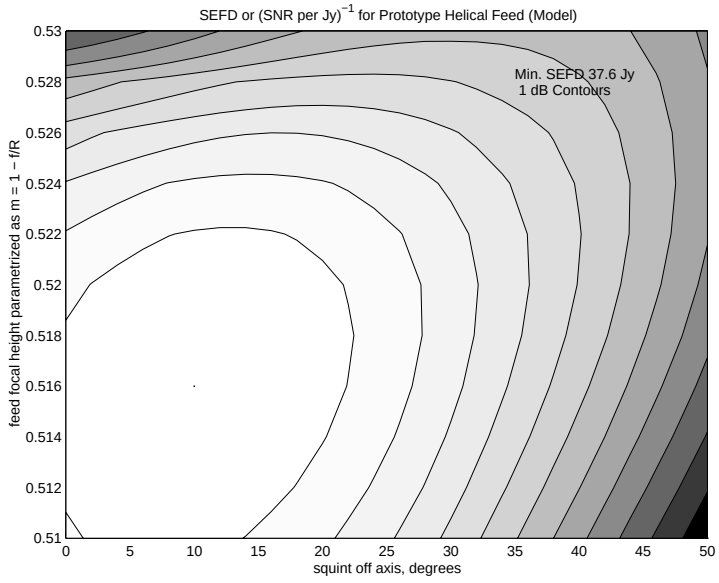

Figure 4-21: The SEFD achieved with a prototype feed that reasonable matches our design criteria. The optimum focal height is consistent with the current location to the level of accuracy of the calculation. The minimum SEFD approaches that of the Gaussian feed 4-11.

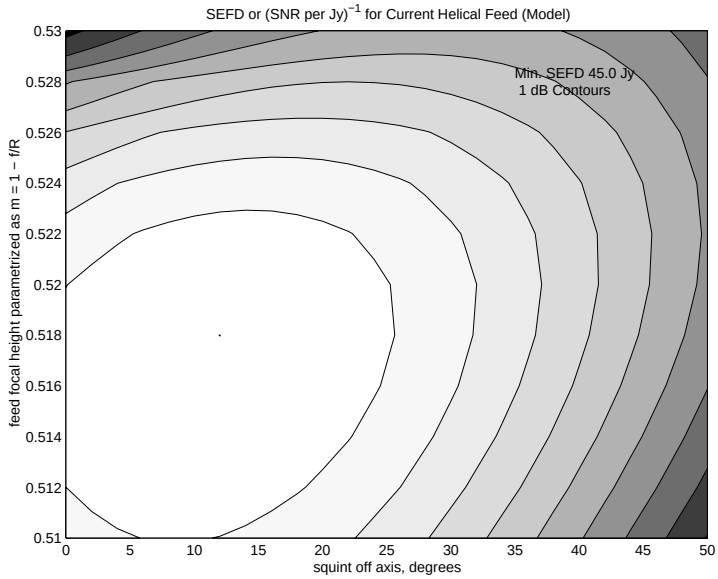

Figure 4-22: The SEFD achieved with a model of our current feed.

Chapter 5

The M.I.T. Near-Real-Time Test Correlator for VSOP

VSOP (VLBI Space Observatory Programme) is a Japanese space science mission under control of the Institute of Space and Astronautical Science (ISAS), with significant participation by NASA and the NSF. The experiment consists of a radio telescope satellite in orbit about the Earth, observing under control from the ground, and telemetering data to a string of tracking stations around the globe. Large ground telescopes observe simultaneously, and when the data are reduced according to more-or-less standard techniques a synthetic aperture up to three Earth-radii in diameter (resolution of 55μas) may be formed. The satellite was launched in February 1997 and is currently entering the second round of proposal solicitations.

In support of this mission we undertook to build a piece of test equipment, a near-real-time correlator that would be a diagnostic tool at the Green Bank (or any other) tracking station. Normally, correlation is performed at computer centers geographically far from the tracking stations. Achieving fringes is an important milestone for each tracking station, so rapid feedback on performance would be highly valued. This chapter describes the hardware, software, and test results of this project.

5.1 VLBI Theory and Practice

A *brief* summary of the subject of Very Long Baseline Interferometry is in order. A plane electromagnetic wave whose source is some astrophysical process is incident on a set of radiotelescopes. With the telescopes sampling the wave at different spatial points, we can measure the spatial coherence function of the incident field. This is what interferometers do. If the measurements are sufficiently finely sampled, they may be inverted to compute the brightness distribution on the sky which gave rise to the incident field (Perley *et al.* 1989 , Thompson *et al.* 1994).

The basic operation in measuring the spatial coherence function (or visibility function) is to correlate the signals from two geographically separate telescopes, which means simply multiply them together and integrate to reduce noise. There will usually be a time delay between the two antennae due to different relative distances from the source. This geometrical delay and its derivative (delay rate) is known and removed. The motion of the antennae move them through the spatial coherence function – they move through the fringes. Removing the effects of this motion is called phase tracking. Both the phase rate (measured in Hz) and the phase acceleration are removed.

However, there will always be errors in the predetermined values of delay and phase rate. Therefore multiple values must be tried. This is done for each baseline; various delays and delay rates are applied to the data, and those values that maximize the observed fringes are found. This is called "fringe fitting."

All of the above takes place before the typical observer sees his data. Baseband analog signals are written to high bandwidth videotape at each observing station, and shipped to a central facility. There the tapes are played back; sophisticated electronics digitize the data, applying corrections based upon models of antenna position and motion. The visibility data are computed (if possible) and then relayed to the investigator.

5.2 Space VLBI and VSOP

Baselines of length an Earth diameter are routine. The next obvious step (after going to higher frequencies) is to place a telescope in orbit – OVLBI. Trials of the concept were made

with TDRSS (Transfer and Data Relay Satellite System) between 1986 and 1988 (Levy *et al.* 1986). TDRSS is a communications satellite in geosynchronous orbit operating at 2.3 MHz and 15 MHz. Baselines with Usuda and Tidbinbilla were formed and a number of sources produced fringes.

VSOP (a.k.a. HALCA) deploys a dish with an effective diameter of 8 m. Receivers operate at 1.6 GHz, 5 GHz, and 22 GHz, although after launch the 22 GHz receiver chain was found to have extraordinarily high system temperature, probably due to a waveguide decoupling during launch. The downconverted signals are relayed to tracking stations via a rear-facing Ku band (14.2 GHz) telemetry antenna. The same antenna receives ground control signals at 15.3 GHz.

The main science goals of this first OVLBI mission include imaging the cores of AGN, monitoring superluminal sources for structure changes, and performing a non-imaging survey of bright sources to learn about their general characteristics.

5.3 M.I.T. Near-Real-Time Correlator

VLBI is complicated business, and OVLBI more so. Because data tapes are shipped from all over the world to central facilities for correlation there is a long turn-around time from observation to detection. Further, correlators are complex instruments that perform at the forefront of current technical capability, and when new must be tested thoroughly to ensure correct operation.

For these reasons it is desirable to have a "quick look" capability, a way to perform a reasonably fast correlation of a small subset of data and determine that at least within the limitations imposed by brevity there is correlated flux in the system, at least on one baseline. Further requirements for such a test instrument would be low cost, portability, and modularity. As large a fraction as possible of off-the-shelf components would be desirable.

This much indicates we should design something around a commercial personal computer. A quick calculation indicates that it is feasible. Imagine a baseline formed by the VSOP satellite and a large Ground telescope, which will turn out to be the Green Bank

140′ (see figure 5-1). The signal to noise ratio of a fringe peak is

$$\mathrm{SNR} = \eta_c \frac{S_c \sqrt{A_{\mathrm{eff},1} A_{\mathrm{eff},2}}}{2k\sqrt{T_{\mathrm{sys},1} T_{\mathrm{sys},2}}} \sqrt{2\Delta\nu\tau} \tag{5.1}$$

where S_c is the correlated flux of the source, A_{eff} and T_{sys} are the effective areas and system temperatures of each antenna, $\Delta\nu$ is the observing bandwidth, τ is the total observing time, and η_c is the efficiency loss due to digitization. Assuming a source with $S_c = 3$ Jy, and using numbers appropriate for a VSOP–Green Bank 140′ baseline, we find a SNR in one second of 18. The digital data telemetered from the satellite is a 2-bit quantized representation of the voltage at the antenna terminals of the satellite. As described later, the nominal data rate from the satellite is 8 megabytes (MB) per second. Taking the same rate for the Ground telescope, in one second of observing we would acquire 16MB of raw data, a large but not unthinkable number for real–time PC applications.

The geometry of the interferometer formed during observing is shown in figure 5-1. Our source of data from the satellite is a direct link from the Green Bank tracking station. The tracking station communicates two-way with VSOP via the Ku band link. Data are telemetered down, and time calibration signals are sent up to the satellite. Our computer is some distance away from the tracking station, in the 140′ control room. The spacecraft data are sent over fiber-optic cable to VLBI interface hardware, demultiplexed, and presented to us on standard ribbon cables in a specified format. In order to perform a VLBI experiment, the 140′ must observe the same source, with the data appropriately filtered, sampled, and formatted. This is not a problem, because the data interchange format is something of an informal standard for VLBI observatories, and the existing VLBI hardware is sufficient to produce the necessary digital data.

The system is built around an Intel Pentium based PC, figure 5-2. Use of the newer PCI data bus is vital. Until a few years ago this experiment would have required extensive custom hardware. Cheap PC-type computers employing an ISA (Industry Standard Architecture) data bus can manage peripheral to CPU or RAM transfer rates of up to 5MB/s. The newer PCI bus can theoretically perform at up to 132MB/s, although 20 is typical. Although a general purpose PC can push data around at this rate, it can not process it simultaneously.

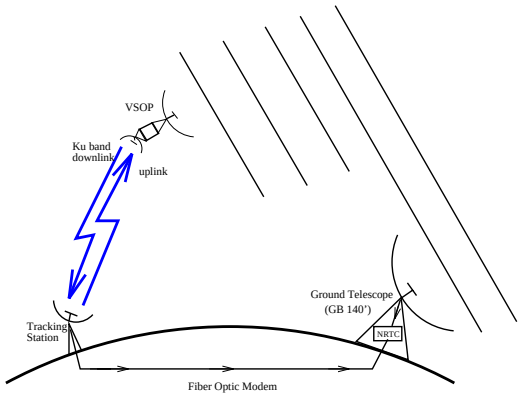

Figure 5-1: The Baseline formed by the VSOP satellite and a Ground radio telescope during testing of the MIT–NRTC. The digitized data from the satellite is downlinked to the tracking station, and relayed to the NRTC via optical cable.

Therefore our goal is to accept data at the required rate of 16MB/s, moving it from a peripheral I/O device directly to RAM, and when data acquisition (DAQ) is complete, to store the data on disk and then process it.

The data path is as follows: the cables from the VLBI rack enter an interface device (XFACE), a custom built ISA-bus expansion card that performs data packing and rate buffering. The packed data are handed to a fast digital I/O (DIO) card, PCI bus, from Datel Co. By purchasing an off-the-shelf component with software we avoid programming PCI bus DMA transfers and other messy details. The Datel part transfers the incoming data directly to RAM (DMA), and when DAQ is accomplished the data is written (much more slowly) to disk under software control. Now the raw data are ready to be processed.

We chose to perform the correlation in the 133 MHz Pentium CPU rather than a dedicated digital signal processing (DSP) device because of more convenient programming and debugging. The processing software was written by Fronefield Crawford with assistance from Deborah Haarsma. We are supplied with an estimate of the expected delay and delay rate by our collaborators on this project at NRAO, principally Glen Langston, Toney Minter, Dan Pedtke, and Larry D'Addario. This estimate is calculated from the satellite's measured orbital elements with a computer ephemeris. The cross-correlation is computed in the Fourier domain; depending on the execution time that can be tolerated by the observer,

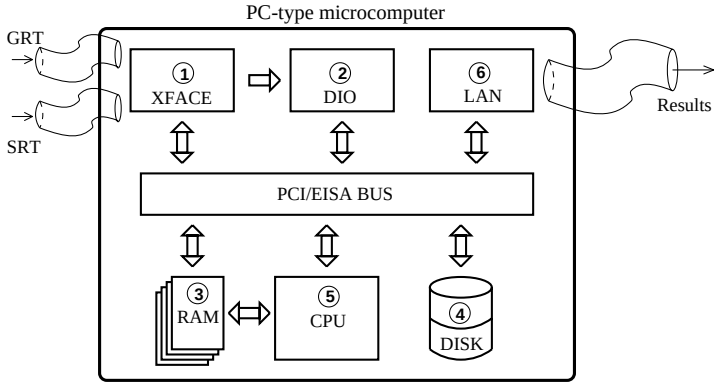

Figure 5-2: A simplified block diagram of the NRTC. Two data streams, one from each telescope, enter through the XFACE (interface) card. The data passes from there to the DIO card, thence directly to RAM. After DAQ is complete, the data is stored to disk under CPU control. Any time thereafter it may be processed either by the computer CPU or dedicated DSP (not shown). Results or data may be transferred over the network (LAN) for further analysis.

we may compute the lag spectrum to very high resolution.

Although it is the only piece of custom hardware, the XFACE card (block diagram in figure 5-3, photo in figure 5-4) required much work so some discussion is warranted. The Datel DIO card will acquire and transfer 16-bit data words. To achieve the highest data rate one should make use of all the bits, and feed it at a uniform rate. The data into the XFACE is from two streams: the ground telescope side, whose data rate is one 2-bit word at 32 MHz, and the space side, whose data rate is nominally the same but due to Doppler shifts may increase or decrease. The job of the interface is to start acquiring data at a precisely defined time, to buffer the data streams so as to equalize the data rates, and to pack the time ordered samples parallel into long words for efficient transfer to the DIO device. The XFACE card was designed and built by the author in Professor Paul Horowitz's laboratory at Harvard, with much advice and help from Prof. Horowitz, and especially from Jonathan Weintroub, who advised during the design, and instructed the author in the art of high–speed digital circuitry construction.

The only question is what the maximum rate difference due to satellite Doppler shift can be, and therefore how much data may pool behind the buffer "dam," or how much data to

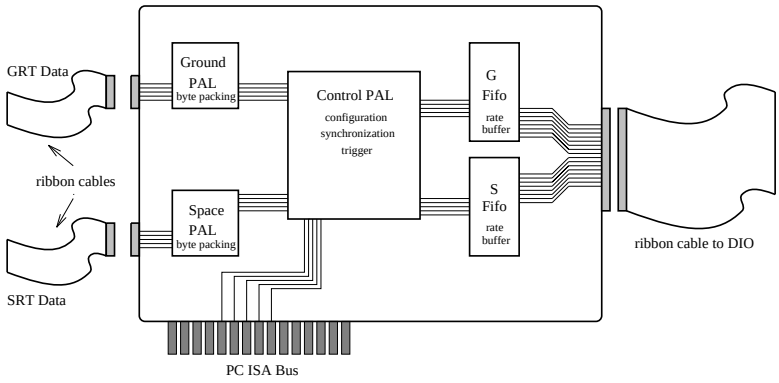

Figure 5-3: A simplified block diagram of the NRTC XFACE. The XFACE accepts the raw digital data to be correlated, and formats it appropriately for the DIO card. It is configurable via the host PC, allowing one to chose from several input data format options, and provides for proper DAQ timing.

pool before transfer starts so as to never empty the buffers. The satellite's orbit has apogee height 22,000 km, and perigee 1000 km. As an upper limit, take the VSOP radial velocity with respect to the ground telescope to be the velocity at perigee. That is approximately 9000 m/s. So the frequency shift from 32 MHz is 960 Hz, over 8 seconds accumulating to about 8000 samples. Let's call it 10^4 samples, which is 2500 bytes. FIFO memories 4kB deep are large but common, so this is not a problem.

The XFACE controls data acquisition. It is armed by the PC some time shortly before the UTC second, and is triggered by a one pulse per second (PPS) signal supplied on the data cables. Hence we know the exact start time of the ground data stream, and we can estimate the space stream offset.

5.4 Some results and conclusion

We installed the NRTC at Green Bank in late winter 1996. Figure 5-5 shows the instrument in use during "first light." Our initial tests indicated some signal format incompatibilities with the NRAO hardware. This turned out to be a real problem which could have delayed successful operation of the tracking station. Identifying this problem was the first success of the NRTC. In the same run we recorded data from VSOP in which test tones were mixed

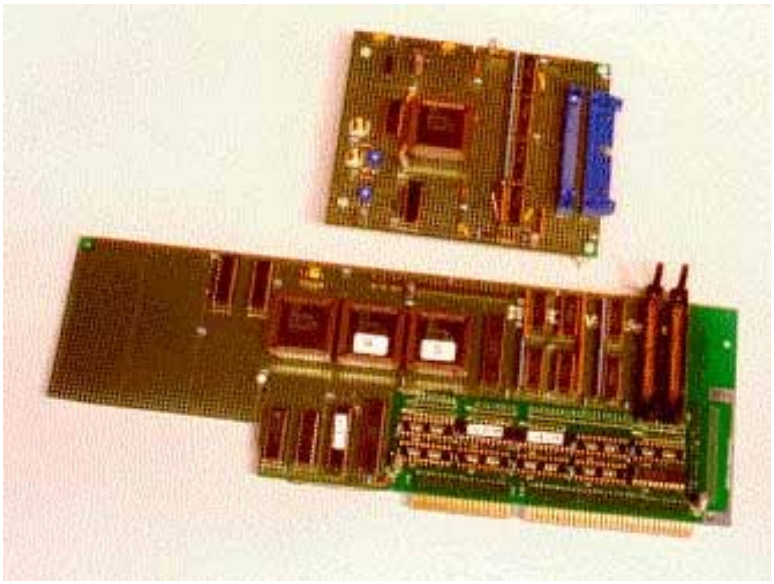

Figure 5-4: A photograph of the Interface built for the NRTC, bottom, and a test data generator, top.

in at the satellite. We clearly see them in the autocorrelation power spectrum, figure 5-6. This indicates data is being faithfully recorded, at least without any particularly sinister garbling.

Observations of the strong OH Maser source W49OH were performed with the Green Bank 140′, and we successfully detected it in the autocorrelation power spectrum of the ground data (figures 5-7 and 5-8). Observations of continuum sources were performed during May 1997. Unfortunately we have not decisively detected fringes in these experiments. Other tracking stations co-observed, and shipped their data to the central correlators at Penticton and Socorro. They did achieve detection of fringes, but at low SNR. With such faint sources, we could not have detected them with our small data set. Nevertheless, we have shown the capability of the NRTC to monitor system performance in real time.

Currently the NRTC is used as test apparatus for the Green Bank tracking station. This is where the flexibility of a PC-based system pays dividends. The computer runs autonomously, collecting data every ten minutes, computing the autocorrelation of each data stream, and transferring the results over the local network to another computer which posts

Figure 5-5: A photograph of the NRTC installed in the control room of the GB140′ telescope. The two ribbon cables on the right carry the data being correlated.

them on a world-readable web page (`http://www.gb.nrao.edu/ovlbi/mitnrc.html`). When VSOP is visible to the tracking station, this provides a quick check of system operation in a complementary way to the information provided in the downlink telemetry.

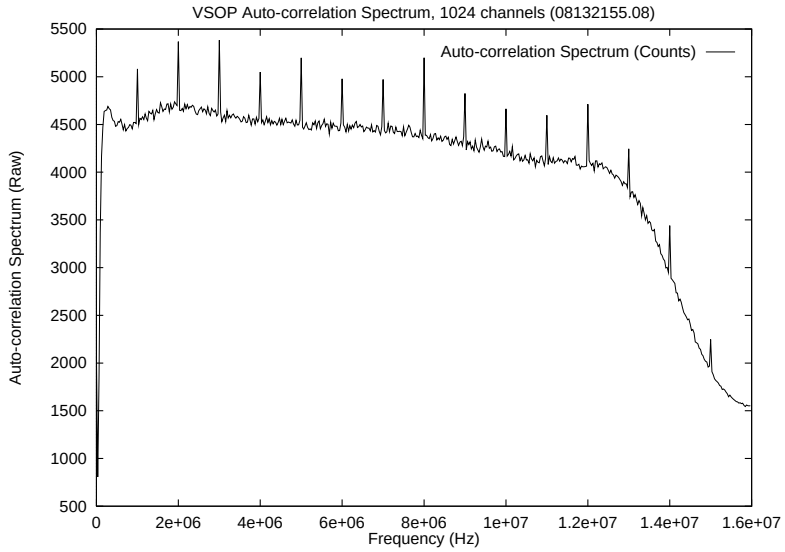

Figure 5-6: The power spectrum of a small amount of VSOP data, produced via autocorrelation by the NRTC. The satellite observing passband is 16 MHz wide; the shoulder of the passband filter is to the right. The regular spikes are harmonic test tones injected into the data by the satellite.

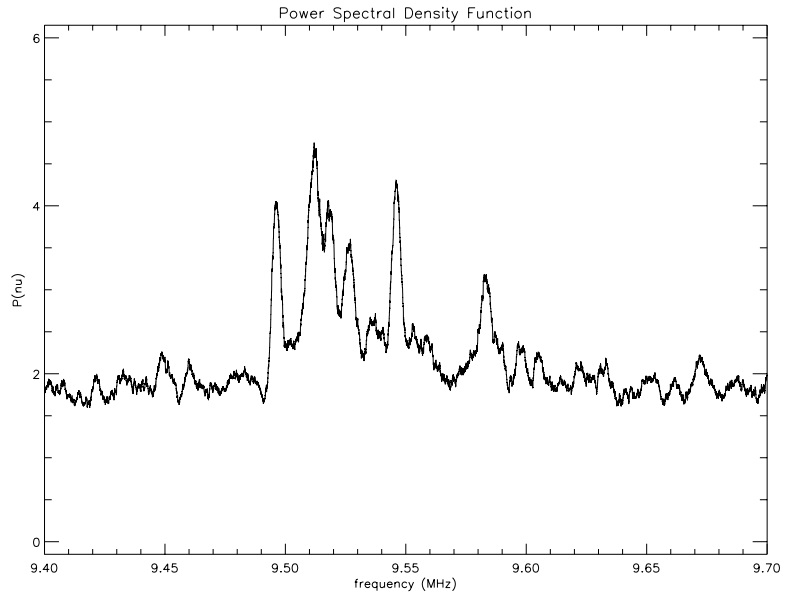

Figure 5-7: The power spectrum of the Galactic hydroxyl maser W49OH in left circular polarization, observed with the Green Bank 140′ telescope with the NRTC. The frequency axis is relative to baseband, after mixing down. The power axis is uncalibrated.

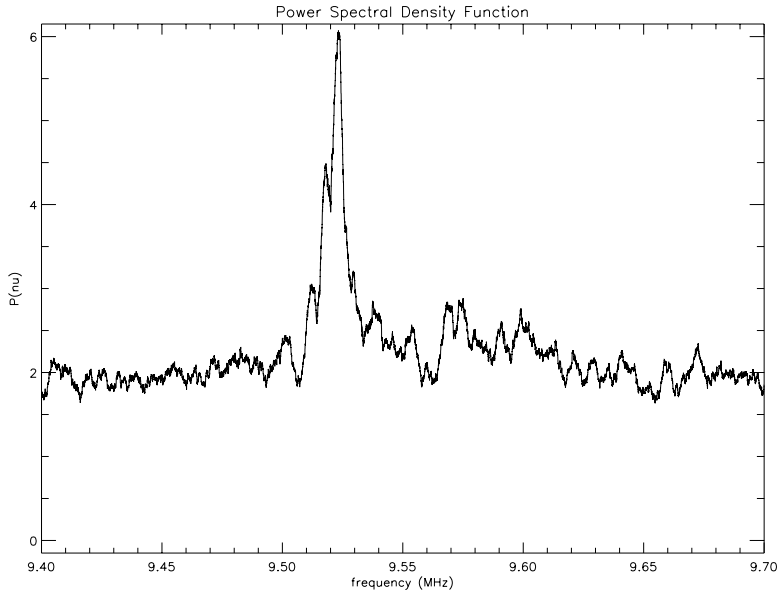

Figure 5-8: The power spectrum of the Galactic hydroxyl maser W49OH in right circular polarization, observed with the Green Bank 140′ telescope with the NRTC. The frequency axis is relative to baseband, after mixing down. The power axis is uncalibrated.

Chapter 6

Low Surface Brightness Studies of Gravitational Lens 0957+561[†]

6.1 Abstract

We have produced deep radio maps of the double quasar 0957+561 from multiple-epoch VLA observations. To achieve high sensitivity to extended structure we have re-reduced the best available 1.6 GHz observations and have combined 5 GHz data from multiple array configurations. Regions of faint emission approximately 15″ north and south of the radio source G are probably lobes associated with the lensing galaxy. An arc 5″ to the east of G may be a stretched image of emission in the background quasar's environment. 1.4″ southwest of G we detect a source that we interpret as an image of emission from the quasar's western lobe, which could provide a constraint on the slope of the gravitational potential in the central region of the lens. We explore the consequences of these new constraints with simple lens models of the system.

[†]This chapter has appeared as a Letter in the Astrophysical Journal (Avruch *et al.* 1997) with coauthors A. S. Cohen, J. Lehár, S. R. Conner, D. B. Haarsma, and B. F. Burke.

6.2 Introduction

Astrophysicists have anticipated the use of gravitational lensing as an observational tool for 60 years (Zwicky 1937 , Scheider *et al.* 1992), and in the case of the double quasar 0957+561 (Walsh *et al.* 1979), after 18 years of study the promise is closest to fulfillment. If one knew the details of the gravitational-lensing potential, and the time delay among the images of flux-variable components, one could make an estimate, albeit cosmology-dependent, of Hubble's constant H_0 (Refsdal 1964).

Efforts to measure the time delay in this system have converged recently (417±3 (Kundic *et al.* 1997), 420±13 (Haarsma 1997)). However, models of the lensing potential have been less well constrained (Falco *et al.* 1991 , Kochanek 1991 , Grogin & Naryan 1996a,1996b) despite detailed observations of the cluster of galaxies providing the lensing mass (Young *et al.* 1981 , Angonin-Willaime *et al.* 1994 , Fischer *et al.* 1997). In an effort to produce a definitive radio map of the object we undertook to re-reduce VLA[1] data gathered by the M.I.T. group, discovering several new features in the field (Avruch *et al.* 1993). In this letter we present improved maps and identify features that may be useful as model constraints.

6.3 Observations

The data sets from which results presented in this letter were computed are listed in Table 1. We first mapped a low resolution λ6cm data set to identify any sources in the primary beam whose side lobes would contaminate the field of interest; during self-calibration of other data sets this emission was taken into account. For sensitivity to low surface brightness features we chose the best extant λ18cm observation. We have also combined five λ6cm data sets from array configurations A, B, and C to achieve more complete (u, v) coverage and compensate for the reduced brightness at λ6cm compared to λ18cm. The fluxes of A and B were roughly constant at these epochs. Using the AIPS software, the data sets were independently mapped and self-calibrated following standard VLA reduction procedures (Cornwell & Fomalont 1989). Each data set was phase self-calibrated several times,

[1]The VLA is part of the National Radio Astronomy Observatory, which is operated by Associated Universities, Inc. under co-operative agreement with the National Science Foundation.

followed by a single amplitude self-calibration, provided that it reduced the map noise. The individual data sets were then co-added in AIPS and the combined data were mapped and self-calibrated as above. To produce source-subtracted images, we use the model for compact emission that the deconvolution algorithm creates in the form of CLEAN components, subtracting the model source from the visibility plane and remapping.

To the north and south of 0957+561 we have detected lobes of emission, separated by about 30″. The northern lobe (N) is more compact, with a λ6cm flux of about 840 μJy and spectral index $\alpha_{6\rm cm}^{18\rm cm} \sim -1.0$ ($S \propto \nu^{\alpha}$). The southern lobe (S) is extended, with a total flux of about 1000 μJy, $\alpha_{6\rm cm}^{18\rm cm} \sim -0.7$. These lobes may be associated with radio galaxy G, or with the lensed quasar in the background. To the east of the quasar images A and B we have detected an arc of emission (R1). The arc is clearly resolved tangentially, with a peak flux of 1.27 mJy beam^{-1} at λ18cm and spectral index $\alpha_{6\rm cm}^{18\rm cm} \sim -0.8$. In Figure 1 we present a radio map of these features; B has been subtracted from the image in the manner described above.

Galaxy G, the dominant contributor to the lensing potential, is definitely extended to the east, southwest, and northwest. To better view the structure near G, we subtracted from the multi-epoch (u, v) data all emission associated with the B quasar image, the BN component (Roberts *et al.* 1985), and G. These structures were identified by directly inspecting the CLEAN components from the multi-epoch map. In Figure 2 the extension of G to the east we name GE, to the northwest GN, to the northeast GNE, and the brightest component of the arc-like structure to the southwest of G we call R2. Table 2 presents the positions and fluxes for these new components.

We are confident that these features are real. N, S, and R1 have been confirmed with detections by Harvanek *et al.* (1996); R1 and perhaps GN have also been confirmed by Porcas *et al.* (1996). The fainter features GE, GN, GNE, and R2 are visible in every individual, reduced data set with sufficient resolution and sensitivity, so it is unlikely that they are artifacts of calibration or deconvolution. On the other hand, detailed substructure such as the double peaks of GNE is not significant, because with extended sources CLEAN produces spurious peaks on that scale (Briggs 1995).

6.4 Discussion

To illustrate our interpretation of these new VLA components, we used the `LENSMOD` software (Lehár *et al.* 1993) to model the lensing mass with a softened power-law potential (Blandford & Kochanek 1987). The model parameters were: the lens position ($\Delta\alpha$, $\Delta\delta$), the critical radius (b), a core radius (θ_c), the power index P ($P = 1$ is isothermal, while $P = 2$ is a Hubble profile), the isodensity ellipticity ($e = 1 - \frac{\text{minor axis}}{\text{major axis}}$), and the major axis orientation (ϕ). As constraints we used the new HST quasar and G1 positions (Bernstein *et al.* 1997) and required that the quasar images have a magnification ratio of 0.75±0.02 (Schild & Smith 1991). We required that any third image of the quasar near G be at least 30 times fainter than B (as a 1σ limit). We also added constraints from the new HST "blobs" and "arc." We required that blob2 and blob3 be images of each other, and that the two knots in the arc share a common source. Note that the HST arc is probably caused by the eastern end of the same object that gives rise to blobs 2 and 3, and this could be used to further constrain lens models. To account for the possibility that the HST objects are at a different redshift than the quasar, we added a uniform scale factor Q_2 to the deflection angles for those components, as an extra model parameter. The lens model parameters were varied until the source plane position and magnitude differences for each pair were minimized, with a resultant reduced χ^2 for the fit of 1.1. The best fit model parameters are given in Table 3, with uncertainties determined by varying the model parameters until the reduced χ^2 increased by 1. Note that the Q_2 range corresponds to HST component redshifts of $z_{\rm HST} \approx 1.3 \pm 0.1$ for an $\Omega = 1$ cosmology, which is fully consistent with the quasar and HST objects being at the same redshift. Figure 3 shows the best fit model for $Q_2 = 1$, with components added to show the modeled radio emission. We do not attempt to account for the VLBI structures (Garrett *et al.* 1994) in this model, and thus make no claims about the time delay or Hubble's constant based upon our model.

We interpret the component GE as the counter-image to the low surface brightness tail of the quasar's western radio lobe E. GE's peak surface brightness and spectral index ($\alpha^{\rm 18cm}_{\rm 6cm} \sim -1.0$) matches that of component E's northeastern extension, so the brighter parts of the lobe are not multiply imaged. The Bernstein *et al.* (1996) HST blobs 2 and 3, almost

certainly multiple images of a background object, are very close to the positions of GE and the northeast end of E; therefore we expect an image of E near where we have found GE. Because not all of E is multiply imaged, the detailed structure of GE can yield strong constraints on the central region of the lens: either the mass distribution is non-singular, in which case GE comprises two merging images of the eastern end of E, or, if the mass has a central singularity, GE will have a sharp cusp at its western end. High resolution radio observations of GE may be able to distinguish these two possibilities, or at least determine an upper limit on the size of the central mass concentration in G. This is also important because, for a given lens mass, the potential near the quasar B image is generally deeper for singular models, yielding a longer predicted time delay and thus a lower H_0 estimate.

The arc-like feature R1 may be a stretched image of background emission. As there is no clear counterpart to the west of G, it is unlikely to be multiply imaged. If the background source is circular, the axial ratio of R1 yields a lower limit of about 5 for its magnification. Jones *et al.* (1993), in *Einstein* HRI data, have detected an apparent x-ray arc about $3''$ northwest of R1. The positions are formally consistent, but seem unlikely to be coincident judging from the relative positions of A and B. An association is not ruled out, however. The authors claim the extended x-ray source is an image of thermal emission from a cooling flow in the cluster hosting the lensed quasar at z = 1.41. There are examples of diffuse non-thermal radio emission associated with x-ray-emitting clusters (Deiss *et al.* 1997), and in this case the lensing magnification may have helped to make it observable. Of course this emission could be foreground; if G has radio lobes, N and S, it could as well have jets. R1 might be back flow from the lobe S, and GN might be a faint jet feeding the lobe N. GE is well explained as an image of the quasar's E lobe, but it's not impossible for it to be the counter-jet of GN, feeding lobe S.

The features R2, GN, and GNE are not readily explained by a lensing hypothesis. R2 is in the position of the western half of the HST arc, but all the models we have investigated would produce an eastward extension of this arc which is not detected. We could appeal, *ad hoc*, to source size and spectral index morphology causing the image to be unobservable. The component GN should have a brighter image $5''$ south of G, which is not seen, though we could make the same appeal and note that it might be difficult to separate visually from S.

GNE should also have a counter-image to the south of G, which is not seen. However, given the interpretation of R1 as lensed, and the faintness of these features, it is not ruled out that at least some of the emission is due to structure in the background quasar's environment.

N and S are certainly not multiply imaged, but whether they are foreground or background is less clear. They could be the radio lobes of the galaxy G. At the lens redshift ($z = 0.36$, and assuming $\Omega = 1$, $h = 0.75$) N and S would have a (projected) proper separation of 120 kpc, and luminosities at 178 MHz of about 10^{24} WHz^{-1}, typical values for low power, limb darkened radio galaxies. The optical classification of G as a cD galaxy, and the fact that N and S are aligned within 30° of its optical minor axis are also consistent (Miley 1980). N and S might be old lobes of the background quasar, in which case the numbers are 170 kpc and 10^{26}WHz^{-1}, more appropriate for powerful, limb brightened sources. If N and S are associated with the quasar, the relatively small lobe separation (56 kpc) and the high core-to-lobe flux ratio ($R = 0.22$) suggest that the jet axis is moderately inclined towards the line-of-sight (Muxlow & Garrington 1991). This inclination readily explains the seemingly large rotation of the jet from the axis defined by N and S to that defined by C and E.

The performance of the VLA at λ18cm has improved markedly since 1980, and new observations should detect or exclude these features with high significance. We are aware of a very deep VLA observation (Harvanek *et al.* 1996) at λ18cm and λ3.6cm; the longer wavelength data should be able to confirm GE, GN, and GNE, and if GE is detected at λ3.6cm it may be possible to determine whether the mass model is singular, or whether GE consists of two merging images.

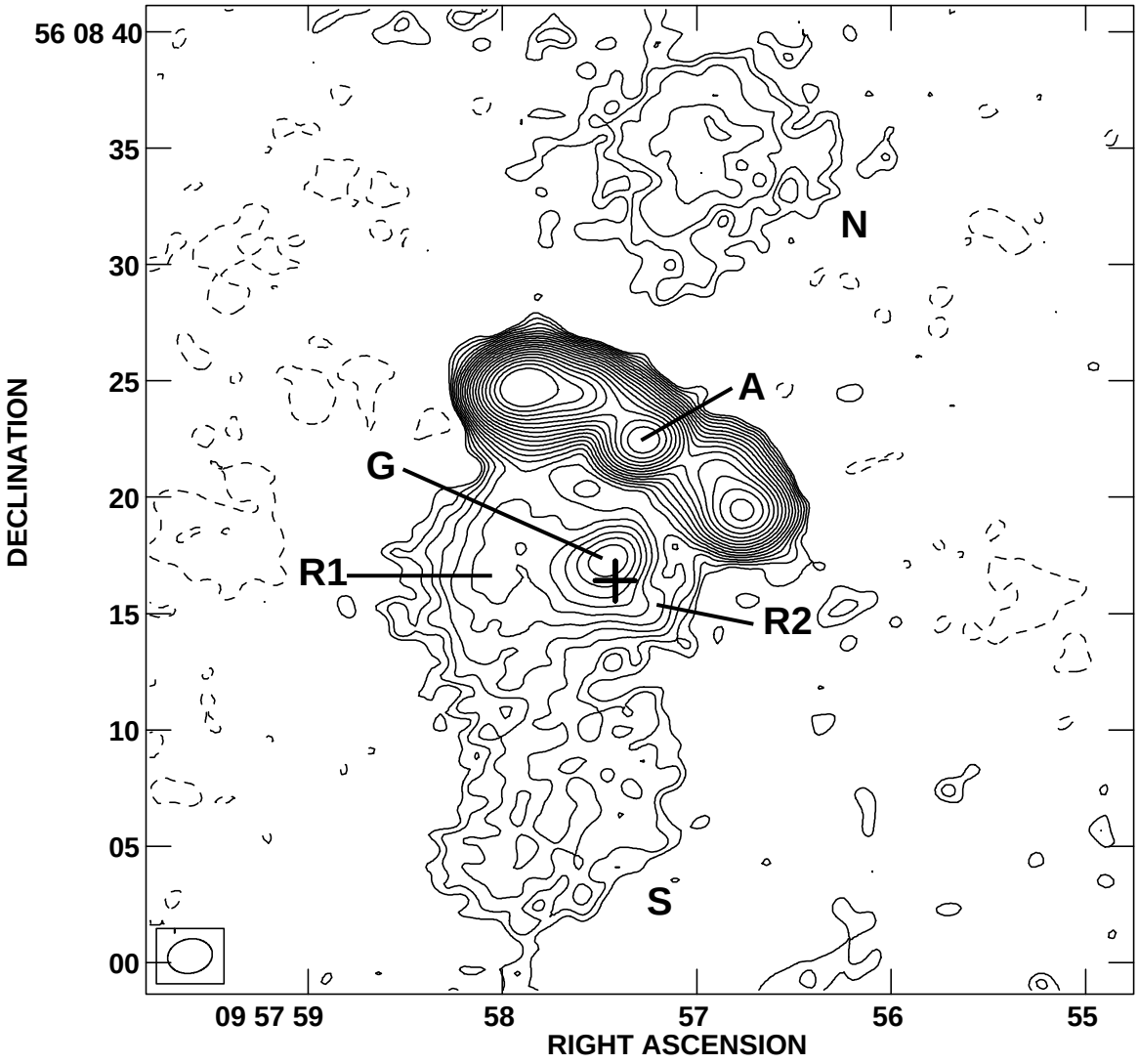

Figure 6-1: Contour plot of λ18cm A array map of 0957+561 on 1980 December 16. The cross hair marks the position at which the quasar B component has been subtracted from the map. The source just to the north of B is G, the lensing galaxy. Contour levels are -0.10%, 0.10%, 0.20%, 0.28%, 0.40%, 0.57%, 0.80%, 1.13%, 1.60%, 2.26%, 3.2%, 4.53%, 6.40%, 9.05%, 12.8%, 18.1%, 25.6%, 36.2%, and 51.2% of the peak intensity of 181 mJy beam^{-1}. The noise level is 105μJy beam^{-1}. The box in the lower left shows the beam FWHM ellipse.

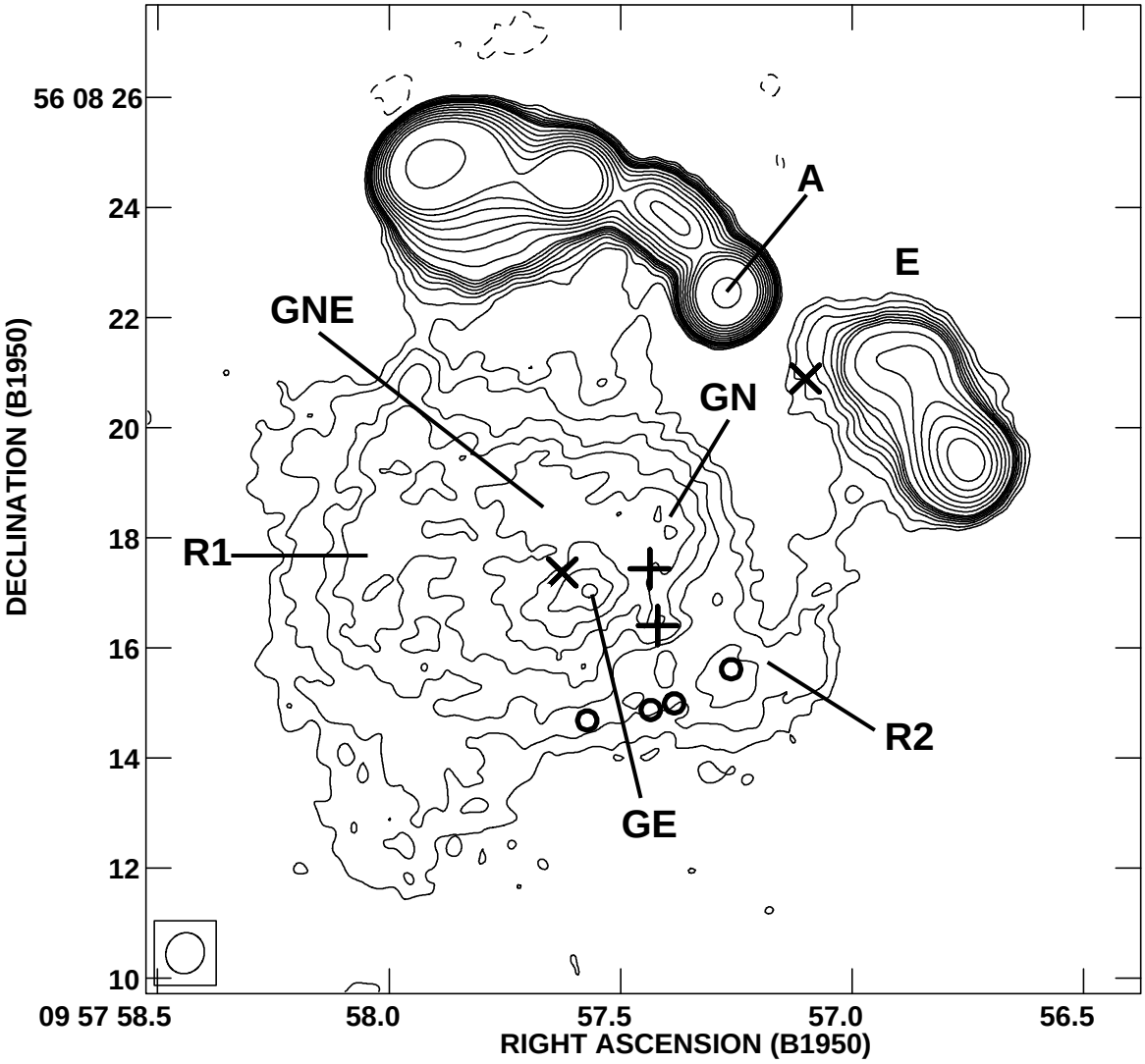

Figure 6-2: Contour plot of λ6cm map of 0957+561 from co-added observations in A, B, and C arrays (data sets #4 – #8, Table 1). The cross hairs (+) are the positions from which models of the components B (to the south) and G were subtracted. The crosses ($\times$) are, east to west, the positions of HST components "blob 2" and "blob 3." The circles are positions along the HST arc, the outer two being the approximate extent and the inner two being "knot 1" and "knot 2." Contour levels are -0.25%, 0.25%, 0.35%, 0.50%, 0.63%, 0.75%, 0.88%, 1.00%, 1.13%, 1.60%, 2.26%, 3.20%, 4.53%, 6.40%, 9.05%, 12.8%, and 51.2% of the peak intensity of 41.8 mJy beam^{-1}. The noise level is 39μJy beam^{-1}. The box in the lower left shows the beam FWHM ellipse.

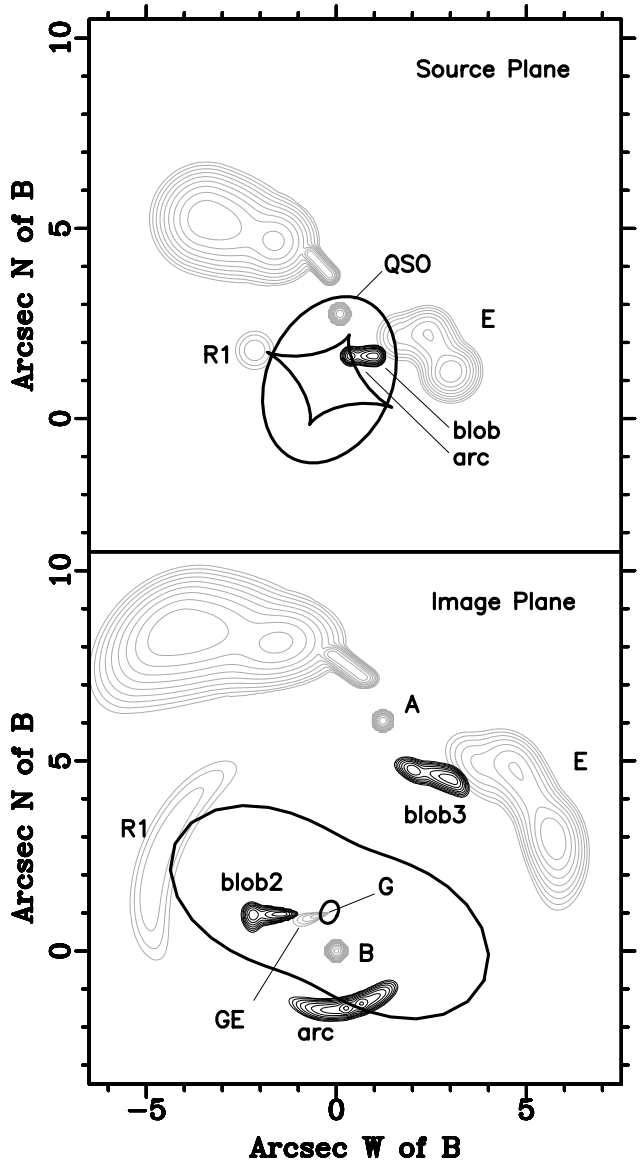

Figure 6-3: Lens model constrained to the HST components, showing disposition of radio components. The HST and radio components are shown as dark and light contours, respectively. The source plane shows how the source would appear without lensing; the caustics separate regions of multiple imaging. The image plane shows the model source seen through our lens model; the critical lines divide the images. The location of G is shown on the image plane, at the center of the lens model. Note that the HST arc is probably formed by the eastern end of the source that yields the HST blobs.

N^o	Obs. Date	λ (cm)	Duration (hrs)[1]	VLA Config.
1	16DEC80	18	3.0	A
2	21AUG90	6	0.8	B
3	17MAR88	6	0.9	C
4	27SEP87	6	1.5	A
5	20JUL87	6	0.8	A
6	09DEC87	6	1.1	B
7	02JUN85	6	1.2	B
8	11JAN87	6	1.6	C

Table 6.1: Archival VLA Data Presented in this Letter.

[1]The duration is the effective VLA observing time devoted to 0957+561, excluding time spent on calibration and instrumental difficulties.

Feature	$(\Delta\alpha'',\Delta\delta'')$[1]	λ6cm Peak[2] mJy beam^{-1}	λ6cm Flux mJy	λ18cm Flux[3] mJy
N	$(-4.5\ ,\ 18.8\ ) \pm (0.5\ ,0.5\ )$	0.440±0.053 [4]	0.840±0.110 [4]	10.15±0.66
S	$(\ 1.5\ ,-11.7\ ) \pm (0.5\ ,0.5\ )$	0.270±0.053 [4]	1.030±0.149 [4]	8.87±0.61
R1	$(\ 5.38,\ 0.80) \pm (0.59,1.17)$	0.366±0.043 [5]	3.646±0.181 [5]	6.61±0.31
R2	$(-1.28,\ -0.80) \pm (0.26,0.21)$	0.250±0.039 [6]	2.270±0.159 [6]	
GE	$(\ 1.24,\ 0.68) \pm (0.04,0.04)$	0.486±0.039 [6]	2.130±0.093 [6]	
GN	$(-0.24,\ 1.68) \pm (0.12,0.24)$	0.373±0.039 [6]	0.930±0.066 [6]	
GNE	$(\ 2.24,\ 2.08) \pm (0.34,0.22)$	0.357±0.039 [6]	1.186±0.073 [6]	

Table 6.2: Faint Emission Features Described in this Chapter

[1] Positions relative to B, α=09^{h}57^{m}57^s.42±0^s.01, δ=56°08′16″.40±0″.1 (B1950)

[2] Flux uncertainties are based on the measured map noise away from source emission. For the components GE, GN, and GNE, the error is dominated by the deconvolution algorithm, and the quoted errors are likely underestimated.

[3] λ18cm, beam FWHM ellipse 1.94″×1.47″, map rms 105μJy beam^{-1}

[4] λ6cm, beam FWHM ellipse 3.51″×2.57″, map rms 53μJy beam^{-1}

[5] λ6cm, beam FWHM ellipse 1.56″×1.37″, map rms 43μJy beam^{-1}

[6] λ6cm, beam FWHM ellipse 0.75″×0.69″, map rms 39μJy beam^{-1}

Parameter	Best Fit Value
$\Delta\alpha^1$	$+0\farcs181\pm0\farcs001$
$\Delta\delta^1$	$+1\farcs019\pm0\farcs001$
b	$2\farcs88\pm0\farcs021$
θ_c	$(<0\farcs02)$
P	$0.88^{+0.04}_{-0.02}$
e	0.538 ± 0.018
ϕ^2	$+65.2\pm0.5$
Q_2	1.03 ± 0.02

Table 6.3: Best Fit Lens Model Parameters

[1] offsets in right ascension and declination from the B quasar image.

[2] orientation in degrees from north through east

Chapter 7

Conclusion

7.1 Arecibo Search for Early Hydrogen – Results

We have presented a search for emission from cosmologically distributed HI. In the volume of data reduced so far, we have not detected any protoclusters in HI emission.

The volume surveyed in the reduced data is $112 \times 10^6 h^{-3}\,\mathrm{Mpc}^3$, to to a volume-averaged flux limit of approximately 1 Jy. We can place upper limits on the detectable HI mass in most of our fields on the order of a few$\times 10^{16} h^{-1}\,\mathrm{M}_\odot$. In the standard bottom-up hierarchical model of structure formation, this is not very interesting limit; detection limits of order 0.01 mJy would be more appropriate, for detecting masses of order $10^{14} h^{-1}\,\mathrm{M}_\odot$.

There are interesting artifacts in the reduced spectra; they have structure similar to that predicted by theoretical investigations of the HI emission in the region of influence of the first quasars. The observed features are too bright by orders of magnitude. A more likely cause than protoclusters would be poor baseline estimation due to strong radio frequency interference (RFI).

There is one possible real source for this structure. Weiringa *et al.* (1993) during deep observations at Westerbork in search of high–z HI, discovered small scale ($\sim 1^\circ - 8^\circ$) linearly polarized structures of brightness temperatures 2–4 K. He interpreted these as being local effects in interstellar medium, perhaps the differential Faraday rotation of an intrinsically smoothly polarized synchrotron emission. Now, these are features of the correct magnitude for the ones we see. In our observations they are more apparent at low Galactic latitude,

more circumstantial evidence. However, I am unsure enough about my baseline subtraction and the effects of the very strong RFI that I can only say I would like to reduce some more data independently to look for correlated structure.

7.2 Future Work

There is a substantial amount of data of varying quality collected during this experiment. The subset I have presented in this thesis was chosen for its homogeneity: uniform binary format, unchanging feed position, complete error log, in a contiguous stretch of calendar dates. It is not necessarily the cleanest or most sensitive. I would like to reduce data from earlier epochs, but first approach the reduction algorithms anew. I hesitate to say we've achieved the limiting sensitivity of our instrument, but in spectrometers of this type the noise does not improve simply by integrating *ad infinitum* (Dowd 1998). As for future observations, the RFI environment may improve when the upgrade is completed, but RFI in general is worsening.

The search for emission from primordial galaxies is a key observational goal of the next decade. Techniques such as searching for Lyα emission (Thommes *et al.* 1998) and the Lyman limit continuum break (Steidel *et al.* 1998); (Dey *et al.* 1998) are setting new distance records every few weeks. Here we see young, but not primeval, galaxies.

The new radio telescopes coming on line now and being planned have as one of their important motivations the search for cosmological HI. The Giant Meter Wave Radio Telescope (GMRT) in Pune, India is due to come online very soon, if not already (Swarup 1996). The instrument is an array of thirty 45m diameter dishes. Twelve antennae are clustered in a compact random arrangement about 1 km $\times$ 1 km in size. The rest are divided among three arms in a rough "Y" shape similar to the VLA, each arm of length $\approx$ 14 km. The telescope is built to operate at low frequencies. The dishes are mesh wire and suitable for observations up to 1420 MHz. Studies of the possible abundance of detectable clusters in the redshift ranges accessible to the GMRT have been performed (Subramanian & Padmanabhan 1993 , Bagla *et al.* 1997), and estimates are that a positive detection might be made at $z = 3.3$ with about 50 hrs of integration in one out of 20 to 30 fields.

The Square Kilometer Array Interferometer (SKAI) is a device with only a name as of yet. Through the techniques VLBI and OVLBI, extremely high angular resolution at centimeter wavelengths has been achieved. In the words of Peter Dewdney of DRAO, "Resolution is a solved problem in Radio Astronomy." It's sensitivity that is needed for the next set of problems to be addressed by radio astronomy, from cosmological HI to radio stars. The SKAI concept is to achieve a total collecting area of a 1 km^2, made up of individual interferometer elements. The R&D effort is being led by the Netherlands Foundation for Research in Astronomy (NFRA), but there is significant international interest.

What form these elements might take is the currently being studied (Braun 1996, 1997). Ideas include: planar elements, such as crossed dipoles, in some kind of self-similar arrangement of scales for multiband observing; small (few meter) hemispherical reflectors; individual large parabolic or spherical reflectors fed with array feeds to sample the focal region, allowing simultaneous multifrequency, multibeam operation.

An instrument of this type could detect very modest masses ($\approx 10^{10}\,M_\odot$) of CDM-distributed HI at $z = 5$ with 400 hrs of integration time. Neglecting RFI, of course; but interferometers have a great advantage single-dish telescopes in that RFI usually averages out of the correlation.

Bibliography

Adelberger, K. L., Steidel, C. C., Giavalisco, M., Dickinson, M., Pettini, M., & Kellogg, M., 1998, *A Counts-in-Cells Analysis of Lyman-Break Galaxies at Redshift* $\approx$ *3*, astro-ph/9804236

Albrecht, A., 1998, *What is the future of Causal Models of Cosmic Structure Formation?*, astro-ph/9802135

Angonin-Willaime, M., Soucail, G., & Vanderriest, C., 1994, *A&A* **291**, 411

Avruch, I., Becker, D., Conner, S., & Burke, B., 1993, *BAAS* **25**, 1403

Avruch, I., Cohen, A., Lehár, J., Conner, S., Haarsma, D., & Burke, B., 1997, *ApJ* **488**, L121

Bagla, J. S., Nath, B., & Padmanabhan, T., 1997, *MNRAS* **289**, 671

Bahcall, N. A. & Cen, R., 1993, *ApJ* **407**, 49

Barnett, R. M., 1996, *Physical Review D* **54**, 1

Bebbington, D. H. O., 1986, *MNRAS* **218**, 577

Bernstein, G., Fischer, P., Tyson, J., & Rhee, G., 1997, *ApJ* **483**, L79

Bertschinger, E., 1993, *Preprint MIT-CSR-93-31*

Bi, H. & Davidsen, A., 1997, *ApJ* **479**, 523

Blandford, R. D. & Kochanek, C. S., 1987, *ApJ* **321**, 658

Braun, R., 1996, in M. N. Bremmer, P. P. van der Werf, & H. J. A. Röttgering (eds.), *Cold Gas at High Redshift*, p. 437, Kluwer Academic Publishers, Dordrecht

Braun, R., 1997, *Small Hemispherical Reflectors for the SKAI?*, The 1kT/SKAI Technical Workshop in Association with the URSI LTWG, Sydney, Australia

Briggs, D. S., 1995, *Ph.D. thesis*, New Mexico Institute of Mining and Technology

Briggs, F. H., Sorar, E., & Taramopoulos, A., 1993, *ApJ* **415**, 99

Collin, R. E. & Zucker, F. J., 1969, *Antenna Theory*, Vol. 1, McGraw-Hill Book Company

Cornwell, T. & Fomalont, E. B., 1989, in R. A. Perley, F. R. Schwab, & A. H. Bridle (eds.), *Synthesis Imaging in Radio Astronomy*, No. 6 in Conference Series, pp 185–197, Astronomical Society of the Pacific

Davies, R. D., Pedlar, A., & Mirabel, I. F., 1978, *MNRAS* **182**, 727

Deiss, B. M., Reich, W., Lesch, H., & Wielebinski, R., 1997, *Astronomy and Astrophysics* **321**, 55

Dey, A., Spinrad, H., Stern, D., Graham, J., & Chaffee, F., 1998, *ApJ* **498**, 93

Djorgovski, S., 1992, in R. R. de Carvalho (ed.), *Cosmology and Large-scale Structure in the Universe*, Vol. 24 of *Astronomical Society of the Pacific Conference*, Astronomical Society of the Pacific, Astronomical Society of the Pacific, San Francisco

Dowd, A., 1998, private communication

Dwarakanath, K. S. & Shankar, N. U., 1990, *Astrophys. Astr.* **11**, 323

Falco, E., Gorenstein, M., & Shapiro, I., 1991, *ApJ* **372**, 364

Field, G. B., 1959, *ApJ* **129**, 536

Fischer, P., Bernstein, G., Rhee, G., & Tyson, J. A., 1997, *AJ* **113**, 521+

Garrett, M., Calder, R., Porcas, R., King, L., Walsh, D., & Wilkinson, P., 1994, *MNRAS* **270**, 457

Grogin, N. A. & Narayan, R., 1996a, *ApJ* **464**, 92

Grogin, N. A. & Narayan, R., 1996b, *ApJ* **473**, 570

Gunn, J. E. & Peterson, B. M., 1965, *ApJ* **142**, 1633

Haarsma, D. B., 1997, *Ph.D. thesis*, Massachusetts Institute of Technology

Hardy, E. & Noreau, L., 1987, *AJ* **94**, 1469

Harvanek, M., Stocke, J., Tyson, T., & Rhee, G., 1996, *BAAS* **28**, 843

Haslam, C. G. T., Stoffel, H., Salter, C. J., & Wilson, W. E., 1982, *A&AS* **47**, 1

Hogan, C. J. & Rees, M. J., 1979, *MNRAS* **188**, 791

Hu, E., 1998, *Science News* 153(18)

Jackson, J. D., 1975, *Classical Electrodynamics*, John Wiley & Sons, New York

Kochanek, C., 1991, *ApJ* **382**, 58

Kolb, E. W. & Turner, M. S., 1990, *The Early Universe*, Addison-Wesley Publishing Co.

Kraus, J. D., 1988, *Antennas*, McGraw-Hill Book Company, 2 edition

Kumar, A., Padmanabhan, T., & Subramanian, K., 1995, *MNRAS* **272**, 544

Kundic, T., Turner, E. L., Colley, W. N., Gott, J. Richard, I., Rhoads, J. E., Wang, Y., Bergeron, L. E., Gloria, K. A., Long, D. C., Malhotra, S., & Wambsganss, J., 1997, *ApJ* **482**, 75+

Lehár, J., Langston, G., Silber, A., Lawrence, C., & Burke, B., 1993, *AJ* **105**, 847

Levy, G. S., Linfield, R. P., Ulvestad, J. S., amd J. F. Jordan Jr., C. D. E., Nardo, S. J. D., Christensen, C. S., Preson, R. A., Skjerve, L. J., Stavert, L. R., Burke, B. F., Whitney, A. R., Cappallo, R. J., Rogers, A. E. E., Blaney, K. B., Maher, M. J., Ottenhoff, C. H., Jauncey, D. L., Peters, W. L., Nishimura, T., Hayashi, T., Takano, T., Yamada, T., Hirabayashi, H., Morimoto, M., Inoue, M., Shiomi, T., Kawaguchi, N., & Kunimori, H., 1986, *Science* **234**, 117

Lupton, R., 1993, *Statistics in Theory and Practice*, Princeton University Press

Madau, P., Meiksin, A., & Rees, M. J., 1997, *ApJ* **475**, 429

Miley, G., 1980, in G. Burbidge, D. Layzer, & J. Phillips (eds.), *ARA&A*, Vol. 18, p. 165, Annual Review Inc.

Muxlow, T. & Garrington, S., 1991, in P. Hughes (ed.), *Beams and Jets in Astrophysics*, p. 52, Cambridge University Press, New York

Noreau, L. & Hardy, E., 1988, *AJ* **96**, 1845

Padmanabhan, T., 1996, *Cosmology and Astrophysics Through Problems*, Cambridge University Press

Peebles, P. J. E., 1993, *Principles of Physical Cosmology*, Princeton University Press, Princeton

Perly, R. A., Schwab, F. R., & Bridle, A. H. (eds.), 1989, *Synthesis Imaging in Radio Astronomy*, Vol. 6 of *ASP. Conference Series*, Astronomical Society of the Pacific

Peterson, B. M., 1997, *An Introduction to Active Galactic Nuclei*, Cambridge University Press, Cambridge

Pettini, M., Steidel, C. C., Adelberger, K. L., Kellogg, M., Dickinson, M., & Giavalisco, M., 1997, astro-ph/9708117

Press, W. H. & Schechter, P., 1974, *ApJ* **187**, 425

Press, W. H., Teukolsky, S. A., Vetterling, W. T., & Flannery, B. P., 1992, *Numerical Recipes in C: The Art of Scientific Computing*, Cambridge University Press

Refsdal, S., 1964, *MNRAS* **128**, 295

Roberts, D. H., Greenfield, P. E., Hewitt, J., Burke, B., & Dupree, A., 1985, *ApJ* **293**, 356

Ruze, J., 1952, *Physical Limitations on Antennas*, Technical Report 248, Research Laboratory of Electronics

Ruze, J., 1978, in A. W. Love (ed.), *Reflector Antennas*, IEEE Press

Schild, R. E. & Smith, R. C., 1991, *AJ* **101**, 813

Schneider, P., Ehlers, J., & Falco, E. E., 1992, *Gravitational Lenses*, Springer-Verlag

Schramm, D. N. & Turner, M. S., 1998, *Reviews of Modern Physics* **70(1)**, 303

Scott, D. & Rees, M. J., 1990, *MNRAS* **247**, 510

Shull, J. M., 1997, astro-ph/9709110

Silk, J. & Rees, M. J., 1998, *A&A* **331**, L1

Silver, S., 1949, *Microwave Antenna Theory and Design*, Vol. 12 of *Radiation Laboratory Series*, Chapt. 2, McGraw-Hill Book Company

Spencer, ., 1978, in A. W. Love (ed.), *Reflector Antennas*, IEEE Press

Steidel, C. C., Adelberger, K. L., Dickinson, M., Giavalisco, M., & Pettini, M., 1998, *ApJ* **492**, 428

Steidel, C. C. & Hamilton, D., 1992, *AJ* **104**, 941

Steidel, C. C. & Hamilton, D., 1993, *AJ* **105**, 2017

Subrahmanyan, R. & Swarup, G., 1990, *A&A* **11**, 237

Subramanian, K. & Padmanabhan, T., 1993, *MNRAS* **265**, 101

Sullivan, W. & Knowles, S., 1985, in M. D. Papagiannis (ed.), *The Search for Extraterrestrial Life: Recent Developments*, pp 327–334, IAU

Swarup, G., 1996, in M. N. Bremmer, P. P. van der Werf, & H. J. A. Röttgering (eds.), *Cold Gas at High Redshift*, p. 457, Kluwer Academic Publishers, Dordrecht

Tegmark, M., Silk, J., Rees, M. J., Blanchard, A., Abel, T., & Palla, F., 1997, *ApJ* **474**, 1

Thommes, E., Meisenheimer, K., Fockenbrock, R., Hippelein, H., Roser, H.-J., & Beckwith, S., 1998, *MNRAS* **293**, L6

Thompson, A. R., Moran, J. N., & Swenson, G. W., 1994, *Interferometry and Synthesis in Radio Astronomy*, Krieger Publishing Company, Malabar, Florida

Uson, J. M., Bagri, D. S., & Cornwell, T. J., 1991, *PRL* **67(24)**, 3328

Walsh, D., Carswell, R., & Weymann, R., 1979, *Nature* **279**, 381

Weinberg, D. H., Hernquist, L., Katz, N. S., & Miralda-Escudé, J., 1996, in M. N. Bremmer, P. P. van der Werf, & H. J. A. Röttgering (eds.), *Cold Gas at High Redshift*, p. 93, Kluwer Academic Publishers, Dordrecht

Weintroub, J., 1998, *Ph.D. thesis*, Harvard University

Wieringa, M. H., de Bruyn, A. G., Jansen, D., Brouw, W. N., & Katgert, P., 1993, *A&A* **268**, 215

Wieringa, M. H., de Bruyn, A. G., & Katgert, P., 1992, *A&A* **256**, 331

Young, P., Gunn, J. E., Kristian, J., Oke, J., & Westphal, J. A., 1981, *ApJ* **244**, 736

Zel'dovich, Y. B., 1970, *A&A* **5**, 84

Zwicky, 1937, *Phys. Rev* **51**, 290